8-2013

Electrospun Nanofiber Yarns for Nanofluidic Applications

Chen-Chih Tsai
Clemson University

Recommended Citation

Tsai, Chen-Chih, "Electrospun Nanofiber Yarns for Nanofluidic Applications" (2013). *All Dissertations*. 1609.
https://tigerprints.clemson.edu/all_dissertations/1609

ELECTROSPUN NANOFIBER YARNS FOR NANOFLUIDIC APPLICATIONS

A Dissertation
Presented to
the Graduate School of
Clemson University

In Partial Fulfillment
of the Requirements for the Degree
Doctor of Philosophy
Materials Science and Engineering

by
Chen-Chih Tsai
August 2013

Accepted by:
Dr. Konstantin G. Kornev, Committee Chair
Dr. Igor Luzinov
Dr. Douglas E. Hirt
Dr. Gary C. Lickfield
Dr. Fei Peng

ABSTRACT

This dissertation is centered on the development and characterization of electrospun nanofiber probes. These probes are envisioned to act like sponges, drawing up fluids from microcapillaries, small organisms, and, ideally, from a single cell. Thus, the probe performance significantly depends on the materials ability to readily absorb liquids. Electrospun nanofibers gained much attention in recent decades, and have been applied in biomedical, textile, filtration, and military applications. However, most nanofibers are produced in the form of randomly deposited non-woven fiber mats. Recently, different electrospinning setups have been proposed to control alignment of electrospun nanofibers. However, reproducibility of the mechanical and transport properties of electrospun nanofiber yarns is difficult to achieve. Before this study, there were no reports demonstrating that the electrospun yarns have reproducible transport and mechanical properties. For the probe applications, one needs to have yarns with identical characteristics. The absorption properties of probes are of the main concern. These challenges are addressed in this thesis, and the experimental protocol and characterization methods are developed to study electrospun nanofiber yarns.

A modified electrospinning setup was built which enables control of the properties of electrospun yarns. A library of e-spinnable polymers was generated and the polymers successfully electrospun into yarns. A unique technique for characterization of yarn permeability was developed. The produced electrospun yarns have permeabilities spanning two orders of magnitude (10^{-14}~10^{-12} m^2). The yarns made from porous fibers can significantly increase the absorption rate. The produced yarns have been applied for diagnosis of sickle cell disease. Using the experimental protocol developed for characterization of yarn permeability, the permeability of a butterfly proboscis was examined for the first time. The electrospun yarns and methods of characterization developed in this study will find many applications.

DEDICATION

This dissertation is dedicated to my family. Your constant love, support, and encouragement have guided and helped me during my PhD studies. I would like to thank you all for your prayers and support.

ACKNOWLEDGMENTS

This dissertation could not have been completed without the help of many individuals. First of all, I would like to thank my advisor, Dr. Konstantin G. Kornev, for his support, guidance, and patience during my PhD study. He shared with me not only the excitement of research but also advised me in many other sides of my life. His guidance has provided me with a broad knowledge in the field of porous materials. I am also very grateful to my committee members, Dr. Igor Luzinov, Dr. Douglas E. Hirt, Dr. Gary C. Lickfield, and Dr. Fei Peng for their critical comments and valuable suggestions for the research.

Many thanks to all past and current group members for their help, suggestions, and encouragements during my graduate study: especially, Yu Gu and Dr. Daria Monaenkova in the development of Matlab® codes. Also, I would like to acknowledge the help of undergraduate students, Edgar White, Joseph Howe, and Kara Phillips. I would like to extend thanks to the MSE staff, particularly Kim Ivey, James Lowe, Stanley Justice, and Robbie Nicholson, for helping me learn many tricks of analytical polymer and textile chemistry and engineering.

I enjoyed the time spent with Dr. David Lukas and Dr. Petr Mikes from Technical University of Liberec, Czech Republic. These conversations enriched my knowledge in electrospinning. I would like to extend special acknowledgements to Dr. Alexey Aprelev from Drexel University for the collaboration on the development of new application of the electrospun nanofiber yarns for diagnosis of the sickle cells disease. Dr. Peter Adler, Dr.

Charles E. Beard, and Daniel Hasegawa from the Department of Entomology of Clemson University helped me to understand anatomy of butterfly proboscis and fruitful discussions with them led to the development of an experimental protocol for characterization of permeability of butterfly proboscis.

I have no words to express my gratefulness to my dearest parents, Chun-Pao Tsai and Shien-Nu Wu. They are the greatest parents in the World. Thank you for everything that you give me. The greatest thanks are to my wife, Li-Ching Pan, who is always on my side supporting and encouraging me. I also need to thank our lovely son, Lucas Tsai, for providing a lot of fun, setting the deeper meaning of life, and hope for the future.

TABLE OF CONTENTS

Page

CHAPTER

Table of Contents (Continued)

Page

Table of Contents (Continued)

Page

Table of Contents (Continued)

Table of Contents (Continued)

Page

LIST OF FIGURES

List of Figures (Continued)

Figure Page

List of Figures (Continued)

List of Figures (Continued)

Figure Page

List of Figures (Continued)

List of Figures (Continued)

List of Figures (Continued)

List of Figures (Continued)

Figure Page

List of Figures (Continued)

Figure Page

LIST OF TABLES

CHAPTER ONE

INTRODUCTION

The electrospinning methods for fiber formation are first introduced, and the electrospinning setups and key parameters affecting the produced fibers are discussed.

1.1 History

The first patent showing the drawing of the electrospinning equipment was traced back to John Cooley in 1902 [1]. He filed another similar patent regarding electrospinning a year later in 1903 [2]. During 1934-1944, Anton Formhals made significant contributions to the development of electrospinning for the production of artificial threads using high electric field [3]. In the mid-1990s, nanofiber production has become a prominent research field. The most important research in this field has been conducted by the Reneker group at the University of Akron [4, 5] and the Rutledge group at MIT [6-9]. They have demonstrated that many organic polymers could be electrospun into nanofibers, and characterized these electrospun fibers. Since then, the publications on electrospinning on the Web of Science are increasing exponentially every year.

1.2 Electrospinning Equipment

A typical electrospinning setup (Figure 1.1) includes: a power source which is able to provide a high electric field (> 0.5 kV/cm); a syringe pump to control the liquid flow rate; a capillary (such as a metal needle or a pipette); and an electrode working as a fiber collector.

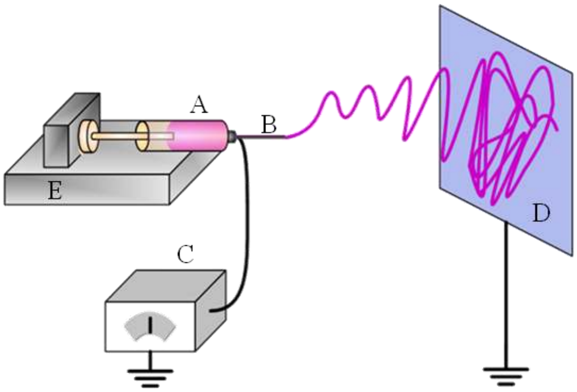

Figure 1.1. A schematic diagram of typical electrospinning setup. (A) syringe with polymer solution, (B) metal needle. (C) high voltage supply. (D) grounded collector. (E) syringe pump.

In the electrospinning process, a polymer solution is extruded through a spinneret (usually a metallic needle) forming a droplet at the tip. When an electric field is applied to the polymer solution, it pulls the droplet to form a conical meniscus which is called the Taylor cone [10, 11]. As soon as the repulsive electrostatic forces between the charges on the drop surface overcome its surface tension, a jet is ejected from the drop. On its way to the collector, the jet vigorously bends and spontaneously twists [6, 7]. This type of movement and additional spiraling and ballooning of the whipping jet leads to significant increase of its length and hence decrease of the jet diameter [12]. Simultaneously, the solvent evaporates during this motion, leaving only solid polymer residues on the collector.

1.3 Factors Affecting Electrospining

In the past decade, over 50 polymers have been electrospun successfully [13]. The cited review contains information about the solvents used, the polymer concentrations in different solvents, and the practical applications of the obtained fibers. However, many parameters affecting the results of electrospinning remain poorly understood. These parameters include (Table 1.1): (1) the solution properties, such as polymer concentration, polymer molecular weight, solvent system, viscosity, conductivity, and surface tension; (2) operation variables, such as flow rate, needle size, operating voltage, the gap between the needle and collector; and (3) electrospinning environment, such as temperature and humidity [3, 13-17].

Table 1.1. Illustration of the variables which should be taken into consideration.

Solution properties	Operating variables	Electrospinning environment
Concentration Molecular weight Viscosity Solvent Surface tension Conductivity	Voltage Needle size Flow rate Gap distance	Temperature Humidity

Among these parameters, the primary factor that influences the electrospinning process is the solution viscosity. As reported in Refs. [3, 14, 15], use of polymers with high molecular weight and solutions with significantly high concentration helps in the nanofiber formation. However, highly concentrated (or viscous) solutions usually hinder the flow through the capillary, thus negatively affecting the process. For this reason, finding an optimal range of polymer concentrations is considered the most important step for successful electrospinning of nanofibers.

Another important factor is the applied voltage. As mentioned previously, a jet can be produced if, and only if, the applied electrostatic force overcomes the droplet surface tension. At lower voltage, a pendant drop, usually sitting at the needle tip, cannot be detached from the tip. It is known [12, 18] that the fibers cannot be formed below a certain voltage because the repulsive force of the charged solution cannot overcome the solution surface tension. In addition, although fibers can be electrospun above a critical voltage, they will usually contain bead defects. Surface tension tries to minimize specific surface area by changing jets into spheres. On the contrary, an excess electrical charge tries to increase the surface area which results in thinner jets. Therefore, high surface tension liquids tend to form beads; decreasing the surface tension can make the beads disappear. These results show that the applied voltage should be optimized to produce defect-free fibers.

However, no theory exists that can take all factors into account and predict the fiber size. When the solution viscosity is increased, the number of beads on fibers and bead size increase as well. As the gap between the needle and collector increases, the jets become thinner. To successfully fabricate a thin and fine jet, it is important to find a balance of the abovementioned parameters.

1.4 Electrospinning Design

The focus of research in textile technology has recently shifted toward the design of electrospinning instruments to fabricate nanofibers with various fibrous assemblies [19-21]. In the Ramakrishna-Teo report [19], designs of different parts of electrospinning setups were reviewed and divided into three main groups: (1) fiber collectors; (2) tools for manipulation of electric field; and (3) solution delivery systems. These designs were compared and the advantages and disadvantages were listed.

1.4.1 Fiber Collectors

Several research groups have reported that it is possible to obtain aligned fibers by using a rapidly rotating collector [22-24]. Matthews et al. [22] proved that the rotating speed of a drum has influence on the degree of alignment of electrospun collagen fibers. As the rotating speed was less than 500 rpm, the randomly deposited collagen fibers were created on the collector. However, when the rotating speed was increased to 4,500 rpm (approximately 1.4 m/s at the surface of the drum), the collagen fibers exhibited good alignment along the rotation direction. Kim et al [25] concluded that the mechanical properties of the electrospun PET nonwovens strongly depended on the linear velocity of drum. They reported that the Young’s modulus, yield stress, and tensile strength of the electrospun PET nonwovens increased with increasing the linear velocity of the drum up to 30 m/min; however, the same parameters decreased when the linear velocity of the drum was set above 45 m/min. Another study by Zussman et al showed that the necking of the electrospun fibers can occur at high enough rotation speed [26]. Therefore, the rotating speed and the fiber orientation are closely linked and have a significant influence on the material properties.

Unlike the conventional electrospinning device with a solid collector, Smit et al [27] proposed to deposit electrospun fibers in a water (non-solvent) bath; this method provided a continuous yarn, which was collected on a rotating drum. After examining the SEM micrographs, these yarns showed that the electrospun fibers were aligned in the direction of the yarn axis. Although the electrospun fibers were randomly deposited on the water surface as a nonwoven web, the web was successfully converted into yarns. Three materials, poly(vinyl acetate), poly(vinylidene fluoride), and polyacrylonitrile, were successfully fabricated using this method. However, some defects on fibers such as beads and fiber loops were detected in the images [27]. No further studies were carried out to determine the yarn properties.

1.4.2 Tools for Manipulation of Electric Field

Li et al. [28] reported that the fibers can be aligned when two electrode collectors were placed parallel to each other. The advantage of this configuration is that it is easy to set up, and it allows formation of highly aligned fibers, which are easily transferable to another substrate. However, the main disadvantage is that the length of the aligned fibers is limited by the gap distance. At a wider gap, the electrospun fibers may not deposited across the gap or the fibers may break, especially if the fiber diameter is small. Another drawback is that the fibers lack the alignment when more fibers are deposited between the parallel electrodes [19]. This is probably due to the accumulation of residual charges on the deposited fibers which changes the desired electric field profile.

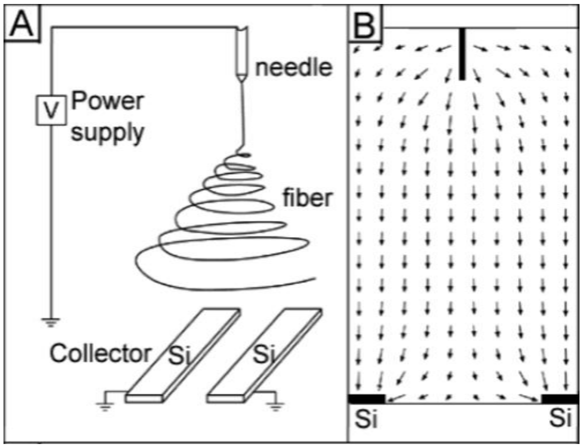

Figure 1.2. (A) A schematic of electrospinning setup to produce uniaxially aligned nanofibers [28]. The collector consisted of two pieces of conductive silicon stripes which were separated by a gap. (B) The electric field vectors were calculated in the region between the needle and the collector. The arrows indicate the direction of the electrostatic field lines [28].

1.4.3 Solution Delivery Systems

A major limitation of industrial applications of electrospinning is the rate of fiber production which is very much lower than the current fiber spinning technology can provide. A straightforward method of increasing the yield of electrospinning is by increasing the number of spinnerets used in the process [19]. However, the presence of adjacent spinnerets may influence the mutual Coulombic interactions, causing jet whipping [29].

Another approach to increase the productivity is using free liquid surface to produce numerous jets during electrospinning. This is called the needleless electrospinning [30, 31]. The idea and its initial implementation was reported by Yarin and Zussman [32]. They applied a strong magnetic field on a magnetic liquid to produce many spikes. The spikes became field concentrators and generated multiple jets. Jirsak et al. [33] observed the formation of multiple jets from a free liquid surface covering a slowly rotating horizontal cylinder. The multiple jets emanating from a free surface can be explained by the Larmor-Tonks-Frenkel instability [30, 33]. The success of the method was subsequently commercialized by Elmarco Company under the brand name of Nanospider^{TM}.

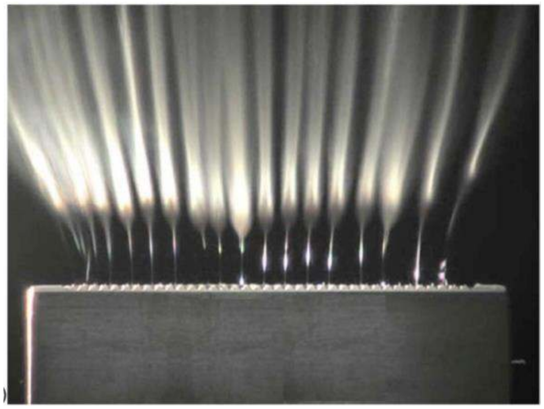

Figure 1.3. Multiple jets produced by cleft-like spinnerets (material: polyvinyl alcohol) [30].

1.5 Nanofibers with Surface Porosity

The major advantage of nanofibers is the high specific surface area needed in many applications, such as catalysis, filtration, and sensor technology. The surface area per unit mass in fiber mats increases as the average fiber diameter is reduced. The fiber diameter, generally, decreases when the concentration of polymer in solution decreases. However, as described before, there is a limiting concentration below which the solution cannot be spun into fibers [34]. In order to significantly increase the surface area of nanofibers, several approaches to modify the surface morphology of nanofibers have been discussed in the literature over recent years [35, 36].

1.5.1 Extraction of a Component from Bicomponent Nanofibers

The most common method employs the idea of electrospinning of a homogeneous mixture of two or more polymers in a common solvent [35, 36]. During the electrospinning, the polymer blends reach thermodynamic instability and turn into immiscible phases resulting in the phase separation. This instability is associated with a dramatic increase of polymer concentrations during the rapid solvent evaporation. The post-treatment of these phase-separated nanofibers by extraction with a selective solvent, which will remove one of the polymer components, causes the formation of pores or complex pore structures in the fibers. For example, Li and Nie [36] reported successful creation of ~30 nm nanopores after removing polyvinylpyrrolidone (PVP) from polyacrylonitrile (PAN)/PVP nanofibers by aqueous solutions.

1.5.2 Phase Separation during Electrospinning

Another approach employs the phase separation of solvent from polymer during electrospinnig using a single component dope [37-39]. These nanoporous morphologies are obtained when a single polymer is dissolved in a highly volatile solvent. The resulting fiber diameters are in the range of micrometers with pores in the range of several hundred nanometers. The average pore size depends on the processing conditions and polymer/solvent system used in the electrospinning. The real mechanism has not been fully understood yet; however, it is believed that the phase separation plays the main role in the formation of pores. Sometimes, this type of separation can be thermally-induced. Robolt et al. [37] showed that the porosity of polystyrene nanofibers was influenced by the solvent mixture of dimethyl formamide/tetrahydrofuran (DMF/THF). The porosity was reduced when the content of less volatile DMF was increased, and finally produced a smooth surface morphology.

Recently, the modification of tranditional electrospinning dope has appeared to be another promising method to fabricate porous fibers; the method is called the emulsion electrospinning [40-43]. The only difference between emulsion electrospinning and conventional electrospinning is that the polymer solution is replaced with an emulsion. The dispersed phase in the emulsion is usually not stable and may cause phase separation either spontaneously or during the electrospinning process. It has been reported that water-soluble drugs or proteins can be encapsulated into polymer fibers by electrospinning of water-in-oil (W/O) emulsion. These fibers are biodegradable and prevent burst release of drugs, prolonging the release time [44, 45]. Correspondingly, lipophilic functional compounds can be added into fibers by oil-in-water (O/W) emulsion. Velankar et al. [40] found that when the solvent evaporated and the viscosity of the emulsion increased more sharply than that of the polymer matrix, the drops did not deform and break up readily. Thus, solid particles or liquid drops can be encapsulated in the electrospun fibers. In this case, the fiber post-treatment by removing the oil or polymer drops results in porous fibers.

Nanofibers with porous structures have many potential applications in filtration, micro- and nano-fluidics, and liquid extraction [39, 46-49].

1.6 References

1. Cooley, J.F., *Apparatus for electrically dispersing fluids*. 1902: US 692631.

2. Cooley, J.F., *Electrical method of dispersing fluids*. 1903: US 745276.

3. Andrady, A.L., *Science and technology of polymer nanofibers*. 2008, Hoboken, N.J.: Wiley. xix, 403 p.

4. Doshi, J. and D.H. Reneker, *Electrospinning process and applications of electrospun fibers.* Journal of Electrostatics, 1995. **35**(2–3): p. 151-160.

5. Reneker, D.H. and I. Chun, *Nanometer diameter fibres of polymer, produced by electrospinning.* Nanotechnology, 1996. **7**(3): p. 216-223.

6. Shin, Y.M., M.M. Hohman, M.P. Brenner, and G.C. Rutledge, *Experimental characterization of electrospinning: the electrically forced jet and instabilities.* Polymer, 2001. **42**(25): p. 09955-09967.

7. Shin, Y.M., M.M. Hohman, M.P. Brenner, and G.C. Rutledge, *Electrospinning: A whipping fluid jet generates submicron polymer fibers.* Applied Physics Letters, 2001. **78**(8): p. 1149-1151.

8. Hohman, M.M., M. Shin, G. Rutledge, and M.P. Brenner, *Electrospinning and electrically forced jets. I. Stability theory.* Physics of Fluids, 2001. **13**(8): p. 2201-2220.

9. Hohman, M.M., M. Shin, G. Rutledge, and M.P. Brenner, *Electrospinning and electrically forced jets. II. Applications.* Physics of Fluids, 2001. **13**(8): p. 2221-2236.

10. Taylor, G., *Disintegration of Water Drops in an Electric Field.* Proceedings of the Royal Society of London. Series A. Mathematical and Physical Sciences, 1964. **280**(1382): p. 383-397.

11. Taylor, G., *The Coalescence of Closely Spaced Drops when they are at Different Electric Potentials.* Proceedings of the Royal Society of London. Series A. Mathematical and Physical Sciences, 1968. **306**(1487): p. 423-434.

12. Rutledge, G.C. and S.V. Fridrikh, *Formation of fibers by electrospinning.* Advanced Drug Delivery Reviews, 2007. **59**(14): p. 1384-1391.

13. Huang, Z.M., Y.Z. Zhang, M. Kotaki, and S. Ramakrishna, *A review on polymer nanofibers by electrospinning and their applications in nanocomposites.* Composites Science and Technology, 2003. **63**(15): p. 2223-2253.

14. Weiss, J., C. Kriegel, A. Arrechi, K. Kit, and D.J. McClements, *Fabrication, functionalization, and application of electrospun biopolymer nanofibers.* Critical Reviews in Food Science and Nutrition, 2008. **48**(8): p. 775-797.

15. Mikos, A.G., Q.P. Pham, and U. Sharma, *Electrospinning of polymeric nanofibers for tissue engineering applications: A review.* Tissue Engineering, 2006. **12**(5): p. 1197-1211.

16. Thompson, C.J., G.G. Chase, A.L. Yarin, and D.H. Reneker, *Effects of parameters on nanofiber diameter determined from electrospinning model.* Polymer, 2007. **48**(23): p. 6913-6922.

17. Theron, S.A., E. Zussman, and A.L. Yarin, *Experimental investigation of the governing parameters in the electrospinning of polymer solutions.* Polymer, 2004. **45**(6): p. 2017-2030.

18. Reneker, D.H. and A.L. Yarin, *Electrospinning jets and polymer nanofibers.* Polymer, 2008. **49**(10): p. 2387-2425.

19. Ramakrishna, S. and W.E. Teo, *A review on electrospinning design and nanofibre assemblies.* Nanotechnology, 2006. **17**(14): p. R89-R106.

20. Nayak, R., R. Padhye, I. Kyratzis, Y.B. Truong, and L. Arnold, *Recent advances in nanofibre fabrication techniques.* Textile Research Journal, 2012. **82**(2): p. 129-147.

21. Park, S., K. Park, H. Yoon, J. Son, T. Min, and G. Kim, *Apparatus for preparing electrospun nanofibers: designing an electrospinning process for nanofiber fabrication.* Polymer International, 2007. **56**(11): p. 1361-1366.

22. Matthews, J.A., G.E. Wnek, D.G. Simpson, and G.L. Bowlin, *Electrospinning of collagen nanofibers.* Biomacromolecules, 2002. **3**(2): p. 232-238.

23. Kameoka, J., R. Orth, Y.N. Yang, D. Czaplewski, R. Mathers, G.W. Coates, and H.G. Craighead, *A scanning tip electrospinning source for deposition of oriented nanofibres.* Nanotechnology, 2003. **14**(10): p. 1124-1129.

24. Moon, S. and R.J. Farris, *How is it possible to produce highly oriented yarns of electrospun fibers?* Polymer Engineering and Science, 2007. **47**(10): p. 1530-1535.

25. Kim, K.W., K.H. Lee, M.S. Khil, Y.S. Ho, and H.Y. Kim, *The effect of molecular weight and the linear velocity of drum surface on the properties of electrospun poly(ethylene terephthalate) nonwovens.* Fibers and Polymers, 2004. **5**(2): p. 122-127.

26. Zussman, E., D. Rittel, and A.L. Yarin, *Failure modes of electrospun nanofibers.* Applied Physics Letters, 2003. **82**(22): p. 3958-3960.

27. Smit, E., U. Buttner, and R.D. Sanderson, *Continuous yarns from electrospun fibers.* Polymer, 2005. **46**(8): p. 2419-2423.

28. Li, D., Y.L. Wang, and Y.N. Xia, *Electrospinning of polymeric and ceramic nanofibers as uniaxially aligned arrays.* Nano Letters, 2003. **3**(8): p. 1167-1171.

29. Theron, S.A., A.L. Yarin, E. Zussman, and E. Kroll, *Multiple jets in electrospinning: experiment and modeling.* Polymer, 2005. **46**(9): p. 2889-2899.

30. Lukas, D., A. Sarkar, and P. Pokorny, *Self-organization of jets in electrospinning from free liquid surface: A generalized approach.* Journal of Applied Physics, 2008. **103**(8).

31. Lukáš, D., A. Sarkar, L. Martinová, K. Vodsed'álková, D. Lubasová, J. Chaloupek, P. Pokorný, P. Mikeš, J. Chvojka, and M. Komárek, *Physical principles of electrospinning (Electrospinning as a nano-scale technology of the twenty-first century).* Textile Progress, 2009. **41**(2): p. 59-140.

32. Yarin, A.L. and E. Zussman, *Upward needleless electrospinning of multiple nanofibers.* Polymer, 2004. **45**(9): p. 2977-2980.

33. Oldrich Jirsak, Filip Sanetrnik, David Lukas, Vaclav Kotek, Lenka Martinova, and J. Chaloupek., *Method of nanofibres production from a polymer solution using electrostatic spinning and a device for carrying out the method*. 2009: US 7585437.

34. Tan, N.C.B., J.M. Deitzel, J. Kleinmeyer, and D. Harris, *The effect of processing variables on the morphology of electrospun nanofibers and textiles.* Polymer, 2001. **42**(1): p. 261-272.

35. Zhang, L.F. and Y.L. Hsieh, *Nano-porous ultra-high specific surface polyacrylonitrile fiber.* Abstracts of Papers of the American Chemical Society, 2005. **229**: p. U967-U967.

36. Li, X.S. and G.Y. Nie, *Nano-porous ultra-high specific surface ultrafine fibers.* Chinese Science Bulletin, 2004. **49**(22): p. 2368-2371.

37. Rabolt, J.F., S. Megelski, J.S. Stephens, and D.B. Chase, *Micro- and nanostructured surface morphology on electrospun polymer fibers.* Macromolecules, 2002. **35**(22): p. 8456-8466.

38. Greiner, A., M. Bognitzki, H.Q. Hou, M. Ishaque, T. Frese, M. Hellwig, C. Schwarte, A. Schaper, and J.H. Wendorff, *Polymer, metal, and hybrid nano- and mesotubes by coating degradable polymer template fibers (TUFT process).* Advanced Materials, 2000. **12**(9): p. 637-640.

39. Uyar, T. and A. Celebioglu, *Electrospun porous cellulose acetate fibers from volatile solvent mixture.* Materials Letters, 2011. **65**(14): p. 2291-2294.

40. Velankar, S.S., M. Angeles, and H.L. Cheng, *Emulsion electrospinning: composite fibers from drop breakup during electrospinning.* Polymers for Advanced Technologies, 2008. **19**(7): p. 728-733.

41. Agarwal, S. and A. Greiner, *On the way to clean and safe electrospinning-green electrospinning: emulsion and suspension electrospinning.* Polymers for Advanced Technologies, 2011. **22**(3): p. 372-378.

42. Shastri, V.P., J.C. Sy, and A.S. Klemm, *Emulsion as a Means of Controlling Electrospinning of Polymers.* Advanced Materials, 2009. **21**(18): p. 1814-1819.

43. Chen, H., J. Di, N. Wang, H. Dong, J. Wu, Y. Zhao, J. Yu, and L. Jiang, *Fabrication of hierarchically porous inorganic nanofibers by a general microemulsion electrospinning approach.* Small, 2011. **7**(13): p. 1779-83.

44. Jing, X.B., X.L. Xu, L.X. Yang, X.Y. Xu, X. Wang, X.S. Chen, Q.Z. Liang, and J. Zeng, *Ultrafine medicated fibers electrospun from W/O emulsions.* Journal of Controlled Release, 2005. **108**(1): p. 33-42.

45. Weiss, J., C. Kriegel, K.A. Kit, and D.J. McClements, *Nanofibers as Carrier Systems for Antimicrobial Microemulsions. Part I: Fabrication and Characterization.* Langmuir, 2009. **25**(2): p. 1154-1161.

46. Zhao, L.M., H.K. Lee, and R.E. Majors, *The Use of Hollow Fibers in Liquid-Phase Microextraction.* Lc Gc North America, 2010. **28**(8): p. 580-+.

47. Lee, J.Y., H.K. Lee, K.E. Rasmussen, and S. Pedersen-Bjergaard, *Environmental and bioanalytical applications of hollow fiber membrane liquid-phase microextraction: A review.* Analytica Chimica Acta, 2008. **624**(2): p. 253-268.

48. Lee, I.H., J.Y. Park, and B.W. Han, *Preparation of electrospun porous ethyl cellulose fiber by THF/DMAc binary solvent system.* Journal of Industrial and Engineering Chemistry, 2007. **13**(6): p. 1002-1008.

49. Whitesides, G.M., *The origins and the future of microfluidics.* Nature, 2006. **442**(7101): p. 368-373.

CHAPTER TWO

REVIEW OF BASIC PHYSICAL PHENOMENA USED FOR CHARACTERIZATION OF NANOFIBER YARNS

2.1 Surface Tension

From the macroscopic point of view, the transition layer separating two phases of materials can be considered as an infinitely thin membrane. Consider a soap film stretched on a wire frame with one side attached to a movable wire as shown schematically in Figure 2.1. Setting the movable wire free, one observes that this wire slides toward the film [1]. These experiments with soap films suggest that both surfaces of soap film are held under some tension. Therefore, a flat fluid/fluid interface is not stable but it tends to decrease its surface area. If the force acting per unit length of the soap film is denoted by σ one can measure this force by applying different weight W to the movable wire. It appears that the wire can sit in equilibrium only at a certain weight which is equal to $W = 2\sigma L$, where L is the wire length. This experiment shows that the surface tension of the soap film is constant and it does not depend on the surface deformation.

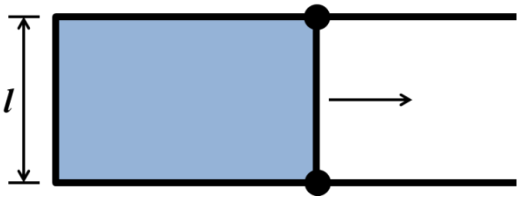

Figure 2.1. The concept of surface tension. A soap film is stretched on a wire frame with one side attached to a movable wire.

This concept appears to be applicable for any fluid/fluid interfaces, not necessarily soap films [1]. In order to characterize these interfaces, one can introduce a constant interfacial tension σ acting parallel to the surface separating two dissimilar fluids. In the SI units, the surface tension is measured in Newtons per meter (N/m). Table 2.1 lists the values of surface tension of different liquids at 20 °C in mN/m [2].

Table 2.1. Values of surface tension of different liquids at temperature of 20 °C [2].

Liquid	Surface tension (N/m)	Liquid	Surface tension (N/m)
Water	72.8×10^{-3}	*cis*-Decalin	32.2×10^{-3}
Glycerol	64×10^{-3}	Hexadecane	27.47×10^{-3}
Formamide	58×10^{-3}	Hexane	18.4×10^{-3}
Ethylene glycol	48×10^{-3}	Methanol	22.5×10^{-3}
Diiodomethane	50.8×10^{-3}	Ethanol	22.4×10^{-3}

The concept of surface tension can be put into a thermodynamic framework by considering an elementary act of formation of a new surface as an attachment of a “frozen” liquid platelet of infinitesimally small thickness and area $dxdy$ with the surface energy per unit area Σ. Placing a single elementary platelet at an empty spot, one changes the surface energy by $dU = \Sigma dxdy$. To keep this platelet in equilibrium, one needs to apply the force $dF = \sigma dy$. The work done by this force to support the platelet of width dx is equal to $dA = dxdF$. Therefore, the energy budget is written as $dU = dA$, leading to the identity $\Sigma = \sigma$. In this derivation, we assumed that the material does not deform during the creation of a new surface as if it were built from the Lego bricks.

2.2 Curved Interfaces. The Young-Laplace Equation

When the interface is curved, any elementary block containing the interface will result in a free body diagram where the normal components of the surface tension are not necessarily balanced (Figure 2.2). This misbalance leads to a pressure jump ΔP across the interface.

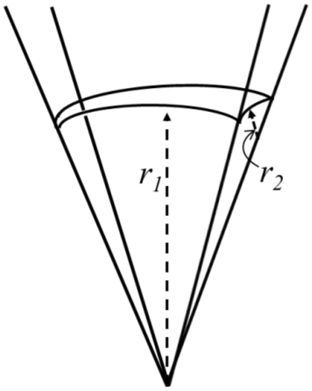

Figure 2.2. Two principle radii of curvature of an arbitrarily curved surface [1].

Let us consider a spherical soap bubble of radius r. The gas inside the bubble is held under an excess pressure ΔP measured relative to the reference atmospheric pressure. The force acting per unit length of the soap film equals to σ. The balance of forces acting on the cross-section of the hemi-sphere reads $\sigma \times 2\pi r = \Delta P \times \pi r^2$. Therefore the excess pressure in a spherical bubble is equal to $\Delta P = 2\sigma/r$. In the case of a cylindrical bubble of the same radius r and length L, one can consider a cross-section along the cylinder through its axis. The balance of forces acting on this cross-section is expressed as $\sigma \times 2L = \Delta P \times 2Lr$. Therefore the excess pressure is $\Delta P = \sigma/r$.

One can approach this problem from the energetic standpoint. Consider a spherical droplet of radius r. The droplet has the surface energy $4\pi r^2\sigma$. If the radius is decreased by dr, the surface energy is decreased by $8\pi r\sigma dr$. In order to support this change of the droplet radius, one needs to do the work $\Delta P 4\pi r^2 dr$. Thus, the energy budget reads $\Delta P 4\pi r^2 dr = 8\pi r\sigma dr$ resulting in the same equation $\Delta P = 2\sigma/r$ with the surface tension twice smaller than that of a soap film having two surfaces. Using the same arguments, one can estimate the pressure difference across the interface of a liquid cylinder with radius r and length L. In this case, the energy budget reads $\Delta P 2\pi r L dr = 2\pi\sigma L dr$ leading to twice smaller pressure difference $\Delta P = \sigma/r$.

In the general case, the pressure discontinuity across any curved surface with two principal radii of curvatures r_1 and r_2 (Figure 2.2) is expressed as [1]:

$$\Delta P = \sigma\left(\frac{1}{r_1} + \frac{1}{r_2}\right). \tag{2.1}$$

This is the Young-Laplace law, qualitatively described by Thomas Young in 1805 [3] and mathematically derived by Pierre-Simon Laplace in 1806 [4].

2.3 Wetting of Surfaces and Young's Equation

According to the IUPAC definition, wetting is a process by which an interface separating a solid from a gas is replaced by an interface separating the same solid from a liquid. Whether a liquid spreads over a given surface or not depends on the values of the surface tensions at liquid/solid, solid/gas and liquid/gas interfaces. In the cases when a liquid drop assumes a shape of a spherical cap on the solid surface the drop profile is completely specified by the contact angle, a physicochemical characteristic of the three dissimilar solid/liquid/gas phases meeting at a contact line. The contact angle is introduced as an angle at which the fluid/fluid interface meets a solid surface. For example, if one fluid is a gas, the balance of forces acting at the contact line in the plane parallel to the solid surface reads (Figure 2.3a) [5]:

$$\sigma_{lv} \cos\theta = \sigma_{sv} - \sigma_{sl} , \tag{2.2}$$

where σ_{lv}, σ_{sv}, and σ_{sl} are the surface tensions of liquid/gas, solid/gas, and solid/liquid, respectively. Eq. (2.2) is the Young's equation connecting the contact angle θ with the surface tensions of constituent phases.

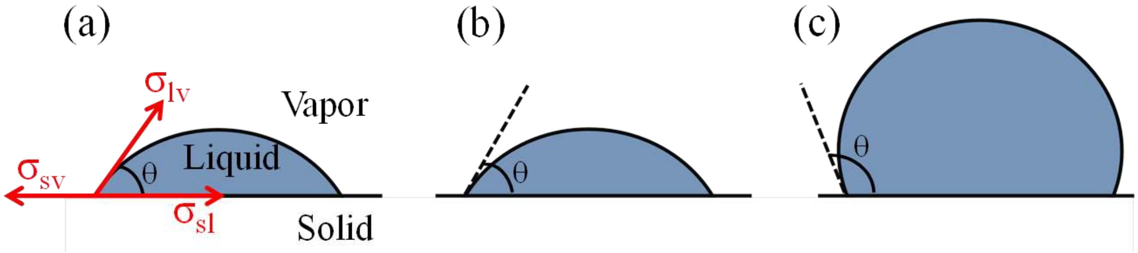

Figure 2.3. Illustration of the wettability of solid surfaces by a given liquid: (a) Forces acting at the contact line. (b) Good wetting, (c) Poor wetting.

Good wetting assumes that the contact angle formed by a droplet is acute. The material is considered poorly wettable if the drop beads on the surface forming the contact angle greater than 90^0. A useful parameter for determining the surface wettability is the spreading coefficient S defined as [6, 7]:

$$S = \sigma_{sv} - (\sigma_{sl} + \sigma_{lv}) . \tag{2.3}$$

If $S > 0$, the liquid spreads completely on a solid surface (complete wetting). If $S < 0$, the liquid does not totally wet a solid surface and forms a droplet on the surface (partial wetting).

2.4 Capillarity

Capillarity is a general term describing a broad class of phenomena associated with formation of liquid menisci. In many cases, capillarity is associated with the ability of a liquid to spontaneous flow into narrow spaces as can be found in numerous examples in our daily life. When a tube of a small radius is brought in contact with a wetting liquid, the liquid spontaneously invades the tube and rises up until it reaches some limiting height. In circular tubes, the liquid meniscus has a spherical shape. Figure 2.4b shows a schematic of meniscus of radius *R* in a capillary tube of radius *r*. Meniscus meets the tube wall at the contact angle θ. Thus, according to the Young-Laplace law, the pressure under meniscus P_l is expressed as $P_\mathrm{l} = P_\mathrm{a} - 2\sigma/R$, or

$$P_l = P_a - 2\sigma\cos\theta / r\,, \tag{2.4}$$

where P_a is the atmospheric pressure above the meniscus.

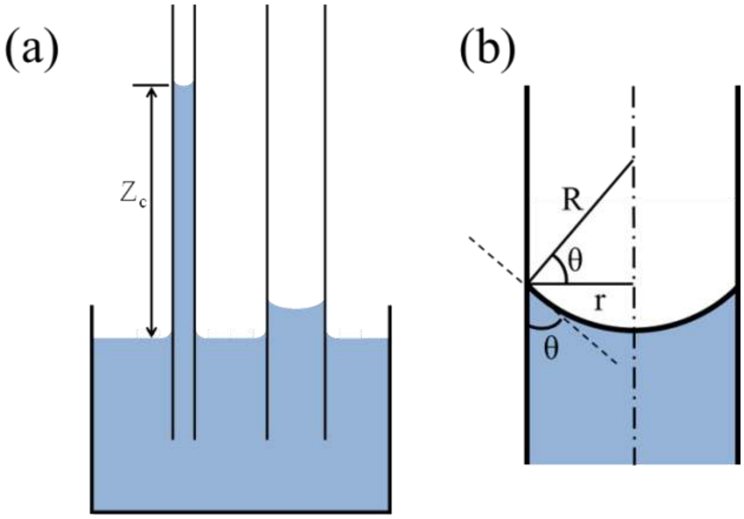

Figure 2.4. (a) The concept of Jurin height: the height of the liquid column is inversely proportional to the capillary radius. (b) A geometrical construction helping to relate the contact angle θ with the capillary radius *r*.

The pressure at the capillary entrance is equal to the atmospheric pressure P_a. When the liquid reaches the maximum equilibrium height Z_c, according to hydrostatics, the pressure under meniscus is equal to:

$$P_l = P_a - \rho g Z_c \,, \tag{2.5}$$

where g is the acceleration due to gravity, and ρ is the liquid density.

Substituting Eq. (2.4) into Eq. (2.5), one can find the equilibrium height of the liquid column, the so-called Jurin height [1, 8]:

$$Z_c = 2\sigma \cos\theta / (\rho g r) \,. \tag{2.6}$$

The lower the contact angle, the higher the liquid column. The Jurin height is large for capillaries of small diameter (Figure 2.4a).

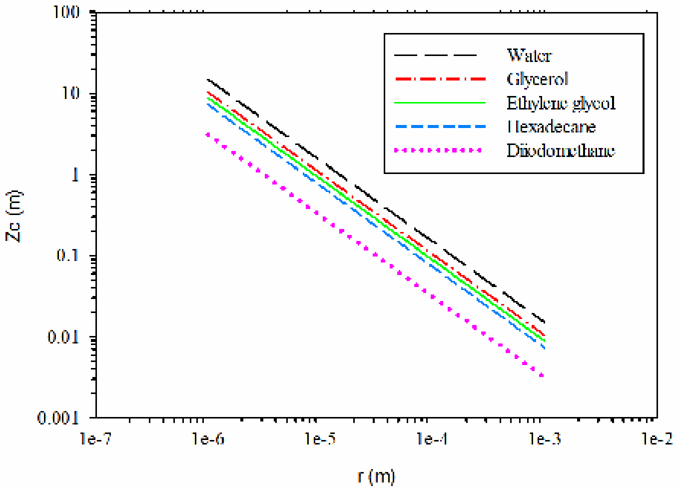

Figure 2.5. Jurin height of different liquids at different capillary radii. Assuming the contact angle $\theta = 0°$.

The Jurin height is graphed in Figure 2.5 for different liquids and capillary radii. For example, water reaches 15 meters in a 2 μm diameter capillary ($\theta = 0^0$) while in a

200 μm diameter capillary it rises only 15 centimeters ($\theta = 0^0$) above the free water surface of the reservoir (Figure 2.5).

There exists a characteristic capillary length, denoted by κ, specifying the condition when gravity becomes important and the associated hydrostatic pressure $\sim\rho g\kappa$ becomes comparable with the capillary pressure $\sim\sigma/\kappa$. Balancing these pressures, one obtains:

$$\kappa = \sqrt{\sigma/\rho g}\,. \tag{2.7}$$

The capillary length κ is generally of the order of few millimeters (Table 2.2), for example, for water it is approximately equal to 2.7 mm. When the following condition meets $r < \kappa$, it is considered that the liquid is in a zero-gravity environment and capillary effects prevail over the gravity. Accordingly, the meniscus in a capillary takes on an almost spherical shape. The opposite case, $r > \kappa$, is referred to as the "gravity-driven" regime, and the meniscus shape in a vertical tube will be affected by the gravity.

Table 2.2. Values of capillary length of different liquids. Surface tensions are taken from Ref. [2], and densities are taken from material safety data sheet (MSDS).

Liquid	**Surface tension (mN/m)**	**Density (kg/m^3)**	**Capillary length (mm)**
Water	72.8	1000	2.7
Glycerol	64.0	1260	2.3
Formamide	58.0	1130	2.3
Ethylene glycol	48.0	1110	2.1
Hexadecane	27.47	773	1.9
Hexane	18.40	650	1.7
Ethanol	22.4	789	1.7
Methanol	22.5	792	1.7
Diiodomethane	50.8	3325	1.2

2.5 Flow of Viscous Fluids through Tube-like and Slit-like Conduits

When the liquid flows through a capillary tube at low speed, the fluid movement can be viewed as a motion of a set of co-axial cylinders with radii r ranging from $r = 0$ at the center of the tube to $r = \mathrm{R}$ on its walls. Each cylinder moves with its own speed v which depends on its radius r. In the absence of gravity and when the flow is sufficiently slow, so that the inertia does not play any significant role, the balance of forces acting on such elementary cylinder with wall thickness dr and length dz is described as (Figure 2.6):

$$2\pi r\eta\frac{dV}{dr}dz-\pi r^2 Gdz=0, \tag{2.8}$$

where the first term is a friction force due to the viscous resistance and the second term is a driving force due to the pressure gradient in the liquid $G = dP/dz$, V is the liquid velocity, and η is the liquid viscosity.

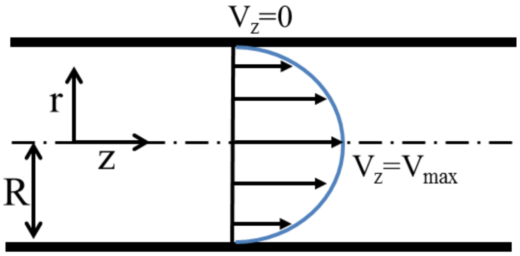

Figure 2.6. Schematic of liquid flow in a cylindrical tube.

Assuming no-slip condition, $V(R) = 0$ one can integrate Eq. (2.8) to obtain:

$$V(r)=(r^2-R^2)G/4\eta. \tag{2.9}$$

The volumetric discharge Q is found by integrating Eq. (2.9) over the tube cross-section:

$$Q = 2\pi \int_0^R V r dr = -\frac{\pi R^4 G}{8\eta}. \qquad (2.10)$$

This is the well-known Hagen-Poiseuille equation for the laminar flows in cylindrical tubes [1]. The mean velocity is defined as:

$$q = Q/(\pi R^2) = \frac{2}{R^2} \int_0^R V r dr = -\frac{R^2 G}{8\eta}, \qquad (2.11)$$

and it appears that the mean velocity is proportional to the square of tube radius.

The same approach is used to find the liquid discharge through a slit of thickness *H*. Assume that the liquid is viscous and incompressible and the flow through the slit with width *W* is laminar and unidirectional. The force balance for elementary volume of thickness *dx* and length *dz* is described as (Figure 2.7):

$$W\eta \frac{dV}{dx} dz - xWGdz = 0, \qquad (2.12)$$

where the first term is the friction force due to the viscous resistance and the second term is the pressure gradient term $G = dP/dz$.

Assuming no-slip condition, $V(H/2) = 0$, the liquid velocity at any point *x* can be obtained by integrating Eq. (2.12):

$$V(x) = (x^2 - \frac{H^2}{4})G/2\eta. \qquad (2.13)$$

The volumetric discharge *Q* is:

$$Q = W \int_{-H/2}^{H/2} V dx = -\frac{WH^3 G}{12\eta}. \qquad (2.14)$$

And the mean velocity is:

$$q = Q / WH = -\frac{H^2 G}{12\eta}. \quad (2.15)$$

This mean velocity is proportional to the square of the slit opening.

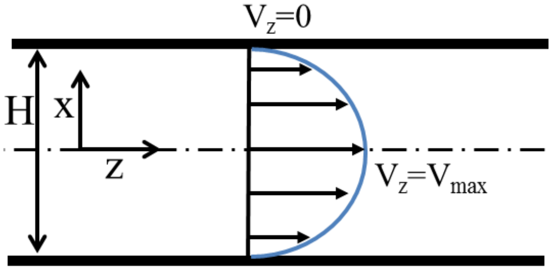

Figure 2.7. Schematic of liquid flow in a slit.

Assuming that a fluid (η is the same) flows through a tube-like conduit and a slit-like conduit with the same opening ($H = 2R$) and pressure gradient (G), the mean velocity of tube-like conduit (q_1) and slit-like conduit (q_2) can be calculated by Eq. (2.11) and Eq. (2.15). The ratio of $q_1/q_2 = 3/8$ indicating that the mean velocity of slit-like conduits will be larger than that of tube-like conduits when they have same opening size and pressure gradient.

2.6 Lucas-Washburn Equation of Spontaneous Uptake of Liquids by Capillaries

While the Jurin height is estimated from the balance of hydrostatic and capillary pressures, this analysis is insufficient to describe the kinetics of liquid uptake by capillaries. Bell & Cameron (1906) [9] studied the dynamics of uptake of water, alcohol, and benzene by a single capillary and found that the position of the wetting front, L, changes in time according to the square root of time kinetics, $L \propto t^{1/2}$. For a tube of a circular cross-section, Lucas (1918) [10] and Washburn (1921) [11] explained the square root of time kinetics by balancing the wetting force with the gravitation force and Poiseuille friction force (Figure 2.6).

The solution of Lucas-Washburn equation neglecting gravity is described here. Assuming that the liquid is incompressible and the flow discharge is constant along the tube $\partial Q/\partial z = 0$, it follows from Eq. (2.10) that the pressure in the liquid is a linear function of the front position, $d^2P/dz^2 = 0$ or $P(z) = az + b$. When the tube is immersed in a liquid reservoir, the pressure in the liquid equals to the atmospheric pressure $P(0) = P_1$. Taking this pressure P_1 as the reference pressure, the first boundary condition reads $P(0) = P_1 = 0$. At the moving front, $z = L(t)$, the pressure in the liquid is equal to the capillary pressure $P_2 = -P_c = -2\sigma cos\theta/R$. Therefore, the constants a and b are specified and the pressure distribution in the liquid column reads:

$$P(z) = \frac{P_2 - P_1}{L} z + P_1 . \tag{2.16}$$

The flow discharge through a tube is expressed as:

$$Q = \pi R^2 dL/dt. \tag{2.17}$$

Substituting Eq. (2.16) and Eq. (2.17) into Eq. (2.10), one finds:

$$\frac{dL}{dt} = -\frac{R^2}{8\eta}\frac{P_2 - P_1}{L} . \tag{2.18}$$

Eq. (2.18) can be integrated using the initial condition $L(0) = 0$ to give:

$$L(t) = \sqrt{\frac{\sigma \cos\theta R t}{2\eta}} . \tag{2.19}$$

For a slit, this equation is written as [where $P_2 = -P_c = -2\sigma cos\theta/H$]:

$$L(t) = \sqrt{\frac{\sigma \cos\theta H t}{3\eta}} \,. \tag{2.20}$$

The Lucas-Washburn (L-W) square root of time kinetics has been confirmed experimentally on many materials [12, 13]. Even in nanometer pores, this regime has been observed [14-16] and confirmed by molecular dynamic simulations [17].

Assuming that a fluid (η is the same) flows through a tube-like conduit and a slit-like conduit with the same opening ($H = 2R$) and pressure gradient (G), the wetting front position in tube-like conduit (L_1) and slit-like conduit (L_2) at a given time can be calculated by Eq. (2.19) and Eq. (2.20), the ratio of L_1/L_2 ~$(3/4)^{1/2}$ ~0.87. The results suggest that the liquid column in slit-like conduits will be longer than that in tube-like conduits, providing that they have the same opening size and pressure gradient. The comparisons of the mean velocity (q) and the wetting front position (L) of these conduits suggest that if the faster transport is of main concern, one needs to choose slit-like conduits.

2.7 Porosity

Porosity is an important physical parameter characterizing a porous material. Porosity is defined as a ratio of the pore volume (V_P) to the total volume of the material (V_T), $\varepsilon = V_P/V_T$. Material pores that are ended at the sample surface are called open pores. Closed pores are buried inside the material and are isolated from the sample surface. In the applications related to the liquid transport only open pores are of interest. Open pores, which are randomly distributed and uniform in size, can be viewed as capillary tubes, and the porous material can be modeled as a bundle of capillaries. In textile materials, the three main components of the material porosity are: (1) intrafiber porosity (formed by voids within the fibers); (2) interfiber porosity (formed by voids between fibers in the yarns), and (3) interyarn porosity (formed by voids between yams). All pores are open pores and the yarn/fabric can be considered as a bundle of capillary tubes with different effective diameters.

Assuming that the yarn cross-section is made of identical cylinders which are closely packed, forming a hexagonal elementary cell (Figure 2.8), the porosity is estimated as [18]:

$$\varepsilon \approx \frac{(\sqrt{3}-\pi/2)R^2}{\sqrt{3}R^2} \approx 0.093. \qquad (2.21)$$

If yarn is saturated with a liquid, the liquid can be trapped in the interfiber space in the middle of the yarn as well as in the space between fibers on the surface of the yarn (as shown by the dotted line in Figure 2.8). Therefore, the yarn porosity defined as $\varepsilon = V_P/V_T$, should be always larger than that obtained from Eq. (2.21).

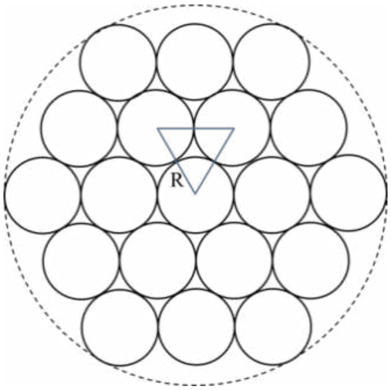

Figure 2.8. A schematic of cross-section of a yarn consisting of close-packed cylindrical fibers of equal radii [18].

2.8 Darcy's Law and Permeability

The description of fluid flow through a porous medium usually relies on Darcy's law, which states that the flow rate q is proportional to the pressure gradient ∇P driving the flow and inversely proportional to the dynamic viscosity of the liquid η. Darcy's law was derived by the French engineer, Henry Darcy (1856). Darcy analyzed experimental observations of the flow of water through sand filters. Darcy's law is written as [1, 13]:

$$q = \frac{Q}{A} = -\frac{k}{\eta} \nabla P \,, \tag{2.22}$$

where Q is the volumetric flow rate, A is the cross-sectional area, and k is the permeability of the porous media.

The structure of Eq. (2.22) is very similar to the structure of equations for the mean velocity through cylindrical tubes and slits. If the porous material is made of cylindrical tubes, Eq. (2.11) equals to Eq. (2.22) with $k = R^2/8$. In the case of slits, Eq. (2.15) equals to Eq. (2.22), and $k = H^2/12$. These simple models of porous materials suggest that the permeability is proportional to the square of pore opening, $k \sim R^2$.

The permeability k can be considered as an ability of a porous material to transport fluids through it. It significantly depends on the intersections between pores or geometrical structure of the medium. This parameter received great attention from materials scientists and engineers (Kozeny & Carman, Sheidegger, Dulien [13, 19-21]). In particular, Kozeny and Carman derived a very useful relation between the materials porosity and permeability considering the packed beads as a bundle of capillary tubes [20, 21]. They postulated that the total internal surface area and the total internal volume are equal to the particle surface area and to the pore volume, respectively (Figure 2.9).

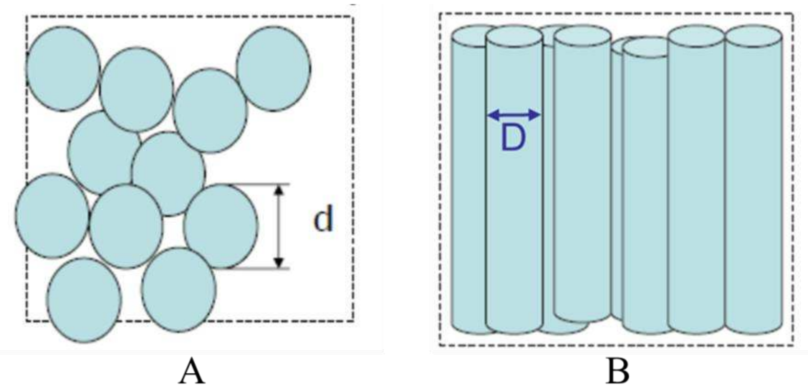

Figure 2.9. Schematics of the Kozeny-Carman's approach for the permeability evaluation of a granular bed. (a) the granular bed is made of spherical particles with diameter *d*, (b) the pores are built by a system of cylindrical tubes (diameter *D*).

The volume of particles (V_p) can be expressed as:

$$V_p = \frac{N_p \pi d^3}{6}, \tag{2.23}$$

where N_p is the number of particles and d is the diameter of spherical particles.

Considering an elementary volume (V_e) with porosity (ε), the volume of particles (V_p) can be also expressed as $V_p = V_e(1 - \varepsilon)$, and the elementary volume (V_e) and total pore volume (V_{pore}) are expressed as:

$$V_e = \frac{N_p \pi d^3}{6(1-\varepsilon)}, \tag{2.24}$$

$$V_{pore} = \varepsilon V_e = \frac{\varepsilon N_p \pi d^3}{6(1-\varepsilon)}. \tag{2.25}$$

Assuming that the same pore volume is occupied by a system of N tubes of diameter D with the same cross-sectional area A, perimeter I, and length L, the total pore volume V_{pore} is written as:

$$V_{pore} = NAL = \frac{\varepsilon N_p \pi d^3}{6(1-\varepsilon)}, \tag{2.26}$$

and the surface area of particles, Σ, as:

$$\Sigma = NIL = N_p \pi d^2. \tag{2.27}$$

Here, the hydraulic radius is introduced as $R_h = A/I$, which is related to $k \sim R_h^2$:

$$R_h = \frac{A}{I} = \frac{\varepsilon d}{6(1-\varepsilon)}. \tag{2.28}$$

And the permeability k of the granular bed:

$$k = \frac{\varepsilon^2 d^2}{k_{KC}(1-\varepsilon)^2}, \tag{2.29}$$

where the k_{KC} is the Kozeny-Carman constant. The Kozeny-Carman theory was examined on packed beads and its phenomenological constants were determined [13, 19-21].

Rahli et al. concluded experimental studies on the monodispersed randomly-packed fibrous mats and compared the experimental data with the Kozeny & Carman theory [22]. The Kozeny-Carman parameter was deduced from experimental permeability by fitting the theoretical formula [22] with experimental data:

$$k = \frac{\varepsilon^3}{k_{kc}(1-\varepsilon)^2 A_p^2}. \tag{2.30}$$

In Eq. (2.30), k_{kc} is the Kozeny-Carman constant, ε is the porosity of the medium, and A_p is the specific area of the particle which is defined as:

$$A_p = \frac{2(2AR+1)}{ARd}, \tag{2.31}$$

where *AR* is the fiber aspect ratio (*L*/*d*), which is calculated by dividing fiber length (*L*) by its diameter (*d*).

2.9 Yarn Flexibility

The Bernoulli-Euler theory of beam bending is typically employed to describe mechanics of fiber and yarn bending. This theory has two basic assumptions:

1. The material is *isotropic* and obeys the linear Hooke's law of elasticity. These properties remain unchanged during deformations;
2. The flat transverse planes of element (xy) in the unloaded beam will still be flat in the bent beam.

These assumptions are adequate for metals and glasses but hardly applicable for yarns. Internal structure of the nanofiber yarns is poorly understood; hence the Bernoulli-Euler beam theory has to be applied with a precaution. However, the estimates of the yarn flexibility based on the data on tensile experiments are worth to have. These estimates will provide a good benchmark to evaluate the yarn flexibility relative to existing textile materials.

2.9.1 Strain in a Bent Yarn

Consider a yarn bent in a loop of radius *R* as shown in Figure 2.10a. The bowed fiber lies in the *xy*-plane. The bending moments *M* are applied to the fiber ends and one needs to find a relation between the bending moments *M* and the fiber radius *R*. Bending moments have stretched the upper parts of the yarn and compressed the lower parts. Since the strain is proportional to the tensile stress, tensile stress across the yarn must be distributed linearly as shown in (Figure 2.10b). There is an intermediate filament in the fiber which is neither extended nor compressed. This filament is called neutral axis. Though it is neither stretched nor compressed (i.e. the length stays same) it is bent. The length of the neutral axis will be $2\pi R$, while the layers above and below this axis experience a change in length, $(2\pi R \pm 2\pi|y|) - 2\pi R = 2\pi y$, i.e. a tensile strain:

$$\varepsilon_{zz} = \pm |y| / R . \tag{2.32}$$

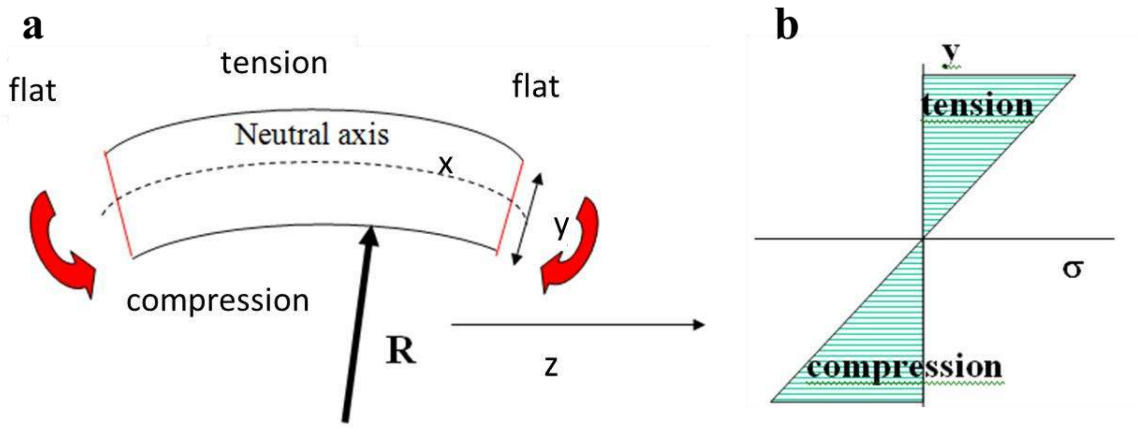

Figure 2.10. (a) Schematic of a curved yarn. The radius of curvature of the bow *R* is assumed to be much greater than the yarn diameter. (b) The distribution of tensile stress across the yarn

2.9.2 Stress in a Bent Yarn

The stress needed to produce this strain is:

$$\sigma_{zz} = E\varepsilon_{zz} = yE / R \ or \ \sigma_{zz} / y = E / R , \tag{2.33}$$

where *E* is the Young's modulus.

This relation holds true for any point along the yarn, even if it is bent in a more complicated shape, provided that $R = R(s)$, i.e. the local radius depends on the arclength s. Due to the second assumption, if the transverse planes are to remain flat, the total force acting on this cross-section should be zero. Therefore, the force distribution shown in Figure 2.10 should give no resultant force. The tensile force acting on the infinitesimal slice with the cross sectional area dA is written as:

$$dF = \sigma_{zz} dA . \tag{2.34}$$

The total force is $\int dF = \int \sigma_{zz} dA = 0$, or using Eq. (2.33) which gives:

$$\int \sigma_{zz} dA = E \int \frac{y}{R} dA = 0 . \tag{2.35}$$

This equation serves for specification of the neutral axis and the quantity $I_y = \int y dA$ is called the first moment of inertia.

2.9.3 Bending Moment

Consider the force moment as a resultant of the stress distribution of Eq. (2.33). In any fiber cross-section perpendicular to the loop plane and neutral axis, the force moment is written as:

$$dM = y \sigma_{zz} dA . \tag{2.36}$$

Substituting Eq. (2.33) into Eq. (2.36), one obtains:

$$dM = E y^2 dA / R . \tag{2.37}$$

Integrating Eq. (2.37), one finds the Bernoulli-Euler result:

$$M = EI / R \tag{2.38}$$

where $I = \int y^2 dA$ is the second moment of inertia. Hence, the bending moment has the right dimension [M] = [N/m^2] [m^4] / [m] = [N*m].

The product *EI* is called flexural rigidity and shows the yarn ability to resist bending. Consider a solid fiber with a circular cross-section and radius *R*,. Placing the origin of coordinates at the fiber center line ($x = 0$, $y = 0$), one has $y = r\sin\theta$, $x = r\cos\theta$, and $dA = rdrd\theta$. The second moment of inertia is calculated as:

$$I = \int_0^R \int_0^{2\pi} r^2 \sin^2 \theta r dr d\theta = \pi R^4 / 4 . \tag{2.39}$$

In the case of a yarn with a circular cross-section with the radius R_y and porosity ε, the elemental area occupied by the solid material is written as $dA = (1 - \varepsilon) rdrd\theta$:

$$I_y = \int_0^{R_y} \int_0^{2\pi} r^2 \sin^2 \theta (1-\varepsilon) r dr d\theta = \pi (1-\varepsilon) R_y^4 / 4 . \tag{2.40}$$

2.10 References

1. Adamson, A.W. and A.P. Gast. *Physical chemistry of surfaces*. 1997.
2. Van Oss, C.J., *Interfacial Forces in Aqueous Media*. 1994: Marcel Dekker.
3. Young, T., *An Essay on the Cohesion of Fluids.* Philosophical Transactions of the Royal Society of London, 1805. **95**: p. 65-87.
4. de LaPlace, P.S., *Supplément au Xe livre du Traité de mécanique céleste*. 1806: Courcier.
5. Berthier, J., *Microdrops and Digital Microfluidics*. 2008: William Andrew Publishing.

6. Gennes, P.-G.d., F. Brochard-Wyart, and D. Quéré, *Capillarity and wetting phenomena : drops, bubbles, pearls, waves*. 2004, New York: Springer.

7. Starov, V.M., M.G. Velarde, and C.J. Radke, *Wetting And Spreading Dynamics*. 2007: CRC PressINC.

8. Jurin, J., *An Account of Some Experiments Shown before the Royal Society; With an Enquiry into the Cause of the Ascent and Suspension of Water in Capillary Tubes. By James Jurin, M. D. and R. Soc. S.* Philosophical Transactions, 1717. **30**(351-363): p. 739-747.

9. Bell, J.M. and F.K. Cameron, *The Flow of Liquids through Capillary Spaces.* The Journal of Physical Chemistry, 1905. **10**(8): p. 658-674.

10. Lucas, R., *Ueber das Zeitgesetz des Kapillaren Aufstiegs von Flussigkeiten.* Kolloid-Z., 1918. **23**: p. 15-22.

11. Washburn, E.W., *The Dynamics of Capillary Flow.* Physical Review, 1921. **17**(3): p. 273.

12. Fisher, L.R. and P.D. Lark, *Experimental-study of the Washburn equation for liquid flow in very fine capillaries.* Journal of Colloid and Interface Science, 1979. **69**(3): p. 486-492.

13. Scheidegger, A.E., *The physics of flow through porous media*. 1957: University of Toronto Press.

14. Neimark, A.V., S. Ruetsch, K.G. Kornev, P.I. Ravikovitch, P. Poulin, S. Badaire, and M. Maugey, *Hierarchical Pore Structure and Wetting Properties of Single Wall Carbon Nanotube Fibers.* Nano Letters, 2003. **3**(3): p. 419-423.

15. Callegari, G., I. Tyomkin, K.G. Kornev, A.V. Neimark, and Y.L. Hsieh, *Absorption and transport properties of ultra-fine cellulose webs.* Journal of Colloid and Interface Science, 2011. **353**(1): p. 290-293.

16. Tsai, C.C., P. Mikes, T. Andrukh, E. White, D. Monaenkova, O. Burtovyy, R. Burtovyy, B. Rubin, D. Lukas, I. Luzinov, J.R. Owens, and K.G. Kornev, *Nanoporous artificial proboscis for probing minute amount of liquids.* Nanoscale, 2011. **3**(11): p. 4685-4695.

17. Martic, G., F. Gentner, D. Seveno, D. Coulon, J. De Coninck, and T.D. Blake, *A molecular dynamics simulation of capillary imbibition.* Langmuir, 2002. **18**(21): p. 7971-7976.

18. Raheel, M., *Modern Textile Characterization Mthds*. 1996: Marcel Dekker.

19. Dullien, F.A.L., *Porous media: fluid transport and pore structure*. 1992: Academic Press.

20. Carman, P.C., *Fluid flow through granular beds.* Transactions of the Institution of Chemical Engineers, 1937. **15**: p. 150-166.

21. Kozeny, J., *Ueber kapillare Leitung des Wassers im Boden.* Sitzungsberichte Akademie der Wissenschaften, Wien, 1927. **136**: p. 271-306.

22. Rahli, O., L. Tadrist, M. Miscevic, and R. Santini, *Fluid Flow Through Randomly Packed Monodisperse Fibers: The Kozeny-Carman Parameter Analysis.* Journal of Fluids Engineering, 1997. **119**(1): p. 188-192.

CHAPTER THREE

FABRICATION OF YARNS FROM ELECTRSPUN FIBERS

A modified electrospinning setup was constructed. This setup enabled control of the properties of electrospun yarns. A library of e-spinnable polymers was generated and the polymers successfully electrospun into yarns. The breaking strength, elongation at break, and Young's modulus of these yarns were studied. The electrospun yarns appeared to be much more flexible than traditional textile fibers and yarns.

3.1 Introduction

Although several groups have developed different techniques to produce nanofiber yarns, none of them demonstrated that the resulting yarns had the repeatable transport and mechanical properties [1-7]. Precision control of these properties, however, is critical for the performance of the probes. In this chapter, the development of an industrially scalable method of yarn formation that provides reproducible mechanical characteristics to these yarns was discussed. A home-made electrospinning collector and a twisting device were developed in this study, and used for the yarn formation. The electric field between the needle and two arm collector was simulated using COMSOL$^{®}$ software which explained the enhancement of fiber alignment between two conductive parallel plates. The process of yarn formation was recorded using a high speed camera (MotionPro X3, IDT Inc.) at 1,000 frames per second (fps), and the yarn length and cone angle changing with time were studied. A geometric structure of twisting device was created and the theoretical relation between the yarn length and cone angle was calculated by this model. The theoretical calculations explained the experimental observations. A library of polymers that can be successfully electrospun into yarns were created. The SEM micrographs showed that fibers in a yarn are highly oriented after twisting. The produced yarns were very uniform in diameter, eg. for 200 μm diameter yarns, the standard deviations were about 5 μm. We also examined the tensile properties of yarns using the stress-strain curves obtained on Instron machine. The results exhibited that the yarns produced following the same experimental protocol had repeatable breaking stress, elongation at break, and Young's modulus. Yarns made from different polymers exhibited different tensile stress–strain behavior suggesting that these electrospun fiber yarns can be used in different applications.

3.2 Modified Electrospinning Setup

As presented in the literature review in chapter one, different spinning collectors and different configurations of electric field have been employed to obtain aligned fibers. However, prior to this work, there were no industrially scalable methods to form nanofiber yarns. The proposed protocol consists of two steps: in the first step, one needs to prepare an array of oriented fibers, which can be gathered in the second step by using a special device. The proposed technique takes advantage of the most popular method of formation of ordered fiber arrays suggested by Li et al. [8] where the fiber orientation is significantly improved by making the target electrode from unipolar parallel bars.

A home-made collection and twisting device for the yarn formation was developed by modifying the traditional electrospinnning setup [9]. The stationary grounded collector (Figure 1.1) was replaced by a rotating disk with four aluminum bars (Figure 3.1A). During electrospinning process, the aligned fibers are collected between each pair of bars. The distance between each pair of bars can be adjusted. In this setup, the interbar distance can be changed from 10 to 30 cm in order to control the yarn length. In the second step, a special twisting device (Figure 3.1B) is used to collect and then twist the aligned nanofibers into a yarn. The twisting device has two main functions: one is to collect fibers from each pair of bars; the other one is to twist fibers into a yarn.

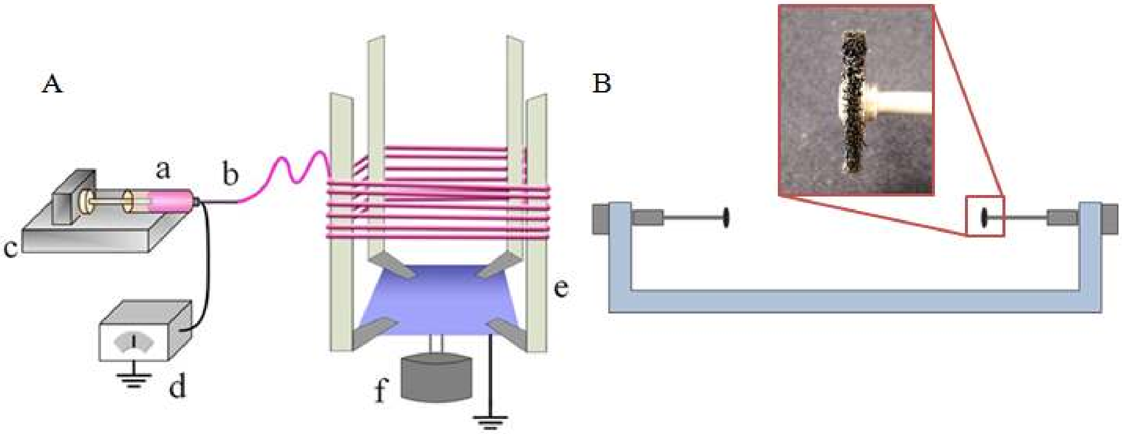

Figure 3.1. (A) A schematic diagram of modified electrospinning setup [9]. (a) syringe with polymer solution, (b) metal needle, (c) syringe pump, (d) high voltage supply. (e) grounded collector with four bars. (f) motor. (B) Schematic diagram of the twisting device to produce yarns. The inset is the magnified brush.

3.3 Electric Field between Needle and Two-Arm Collector

The electric field between the needle and two-arm collector was calculated using

COMSOL® modeling software[1]. The needle was charged to 10 kV, the distance between needle and two-arm collector was 30 cm, the gap between two arms was 20 cm, and the collector was grounded. As shown in Figure 3.2, the red arrows represent the direction of the electrostatic field, and different colors in the plane correspond to different potentials specified in the vertical bar.

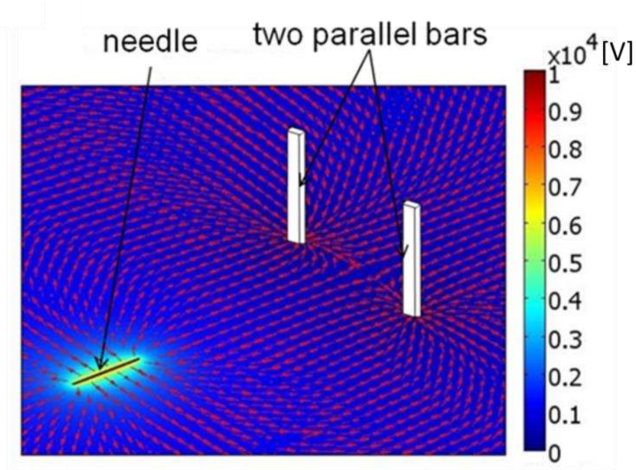

Figure 3.2. The perspective view of electric field in the region between the needle and two-arm collector. The red arrows denote the direction of the electrostatic field, and different colors in the plane correspond to different potentials specified in the vertical bar. The needle is charged to 10 kV and the bars are grounded [9].

As demonstrated in Figure 3.2, the electric field near the plates is almost two-dimensional. Since both plates are kept at the same voltage, the electric field lines branch out from a singular line, which divides the interplate gap in half. Near the two charged plates, the electric field vector E has opposite directions. Therefore, if two identical charges q are situated in different halves of the interplate gap, they will be pushed by the force $F = qE$ toward different plates. For the jet, this specific electrode geometry works as a natural stretching device. As a charged jet approaches the electrodes and is about to

---

[1] I acknowledge Dr. Binyamin Rubin for his help in the simulation of the electric field distribution.

land in between, the electric force pulls the jet in different directions. Because the nanofibers are charged, they repel each other. As a result, the nanofibers align perpendicularly to the plates and do not touch each other.

3.4 Fabrication of Yarns from Electrospun Fibers

The oriented fibers were collected on the rotating disk with four aluminum bars as shown in Figure 3.3a. In order to collect the fibers and twist them into a yarn, a special twisting device was designed and produced. This twisting device consists of two circular wire brushes mounted co-axially and attached to two miniature DC motors. The two arms of the collector support the rolled brushes (Figure 3.3b). The fibers are gathered as a fibrous cylindrical shell attached from its ends to the brushes. The same device is used to form yarns by spinning the brushes in opposite directions: the brushes twist the fibrous shell to a predetermined density, thus forming a yarn (Figure 3.3c). The twisting device allows one to control the yarn diameter and its compactness by changing the total number of revolutions of the brushes. After twisting, the yarn was cut off as a single piece (Figure 3.3d). Using this method, we formed yarns from different materials. By controlling the electrospinning parameters, such as flow rate, polymer concentration, distance between needle and collector etc., one can form a densely-packed or loosely-packed yarn by controlling the electrospinning time and number of twists applied to a yarn.

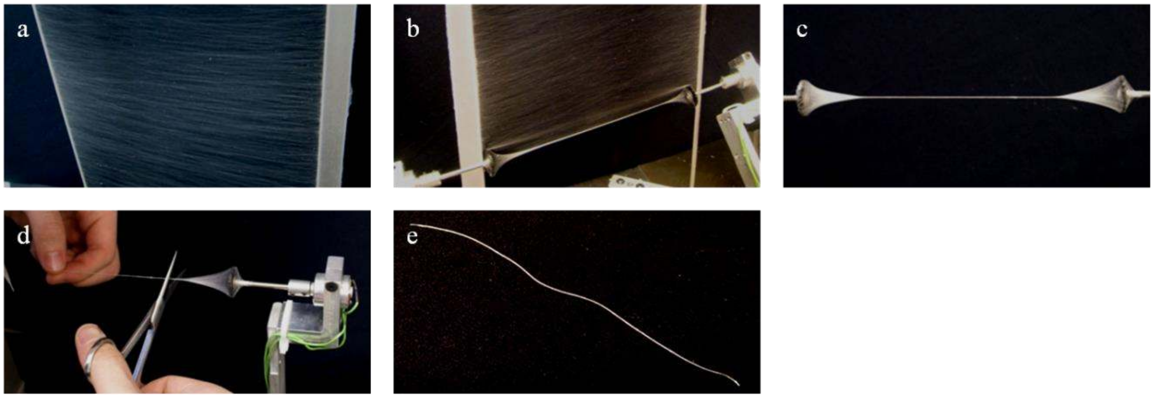

Figure 3.3. Steps of yarn formation: (a) Ordered nanofibers forming a band on the two-arm collector. (b) Gathering nanofibers with the brushes moving along the electrodes rails. (c) Yarn formed after 120 twists. (d) Removal of the yarn using a scissors. (e) The produced yarn [9].

3.5 Process of Yarn Formation

As shown in Figure 3.4a, the fibers were gathered in a fibrous cylindrical shell by rolling the brushes over the electrode rails in the same direction. Once the shell was formed, the brushes were set to rotate in the opposite directions to form a yarn. A high speed camera (MotionPro X3, IDT Inc.) was employed to record the process of yarn formation with a recording frequency of 1,000 frames per second (fps). As shown in Figure 3.4b, the yarn formation started by creating a singular point where two cones of the fibers shell met at the center at the first moment. The brushes keep rotating and the two cones get separated. Two vertexes of the cones move towards the brushes bearing a twisted yarn in-between (Figure 3.4c). Finally, a yarn of known length was formed (Figure 3.4d) and then cut into the required length for further usage.

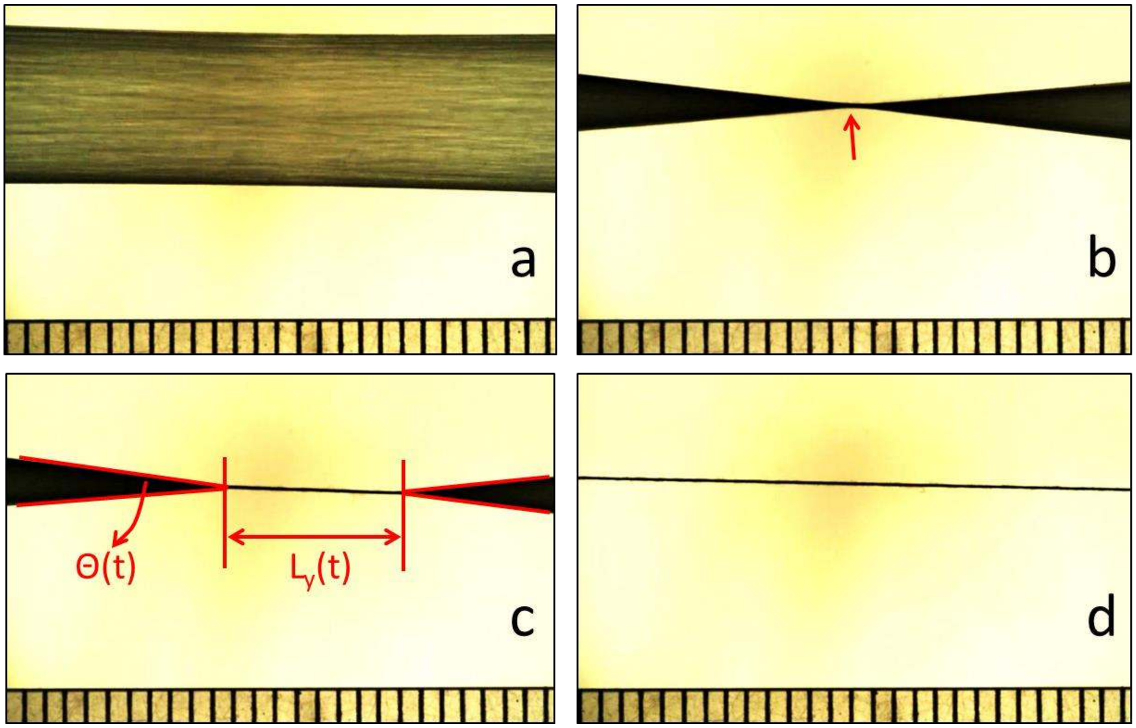

Figure 3.4. Process of yarn formation by rotating the brushes in opposite directions. (a) Fibers were collected as a cylindrical shell. (b) Upon twisting the shell, two cones were developed. These cones met at a singular point, a yarn nucleus. (c) Formation of yarn of length *L* at moment *t*. (d) The produced yarn. A ruler on the bottom of each image was used as a reference scale to calculate the yarn length.

The revolution rate of each brush was determined first. A high speed camera (MotionPro X3, IDT Inc.) recorded the spinning brushes at 500 fps. Nine revolutions took 300 milliseconds (ms) and 18 revolutions took 600 ms. Therefore, the brushes spun at the rate w = 1,800 revolutions per minute (rpm) = 30 revolutions per second (rps).

Two series of experiments were performed to study the rate of yarn formation depending on the gap width between two brushes. In the first series of experiments, the gap between two brushes was set L_g = 13 cm; four experiments were conducted to find a relation of yarn length (L_y) on time (t). In the second series of experiments, the gap between two brushes was decreased to L_g = 10 cm. A high speed camera (MotionPro X3, IDT Inc.) at 1,000 fps was used to record the process of yarn formation. The yarn length (L_y) and cone angle (θ) (Figure 3.4c) were analysed using ImageJ software (NIH).

The yarn length displayed a linear dependence with time (Figure 3.5a). The slope for the 13 cm gap is larger than that for the 10 cm gap which suggests that the yarn formation rate for the 13 cm gap is faster. The yarn formation rate for the 13 cm gap is ~100 mm/s showing that it takes one second to produce a 10 cm yarn length. At the same time, 60 revolutions were applied to the yarn (= 30 rps × 1 s × 2, because two brushes rotated in opposite direction). Here the yarn compactness is characterized by the number of twists per unit length of the yarn; thereafter the yarn compactness is specified by the turns per centimeter (tpcm). Therefore, 60 revolutions applied to the 10 cm yarn leads to yarn twist of 60/10 = 6 tpcm. On the other hand, it takes ~1.4 seconds to rotate the brushes to form a 5 cm yarn at 10 cm gap, and the yarn twist is calculated as ~17 tpcm. That is, the yarn compactness can be designed as long as one identifies the yarn length and brush rotation time.

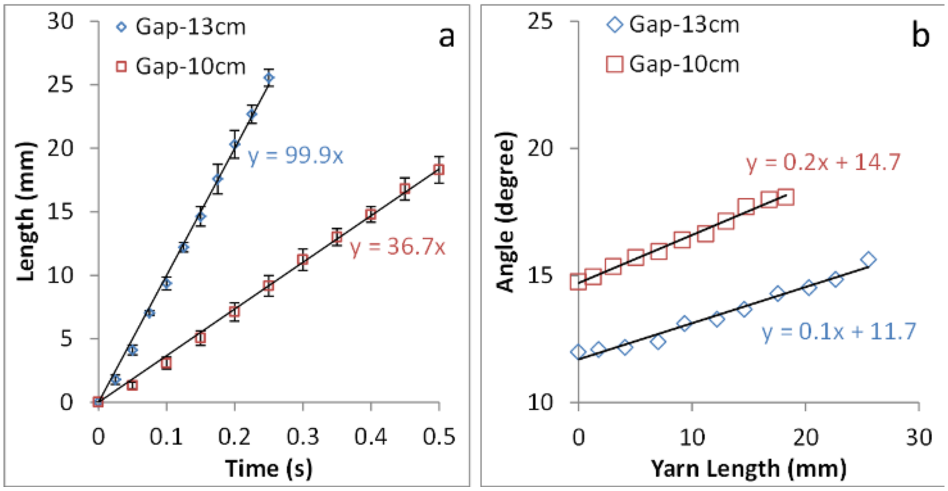

Figure 3.5. (a) Comparison of yarn formation rates for 13 cm and 10 cm gaps. The error bars correspond to the standard deviations. (b) The yarn length-cone angle curve of 13 cm gap and 10 cm gap.

The cone angles were also studied and shown in Figure 3.5b. Since the diameter of brush is constant, the longer the gap between two brushes, the smaller the initial cone angle (Figure 3.5b). When the yarn length (L_y) is getting longer, the cone endpoints approach the two brushes causing an increase in cone angles. The cone angles, however, do not increase significantly, not greater than ~3 degrees, following a linear dependence with the yarn length (Figure 3.5b).

A schematic diagram (Figure 3.6a) shows the geometry of the twisting device and two cones creating a yarn "nucleus" at the center. With the notations shown in Figure 3.6a, where the diameter of brush is D, the gap width is L_g, and the cone angle is θ, the equation relating the cone angle with the geometrical parameters of the yarn twisting device is written as:

$$\tan(\frac{\theta}{2}) = \frac{D/2}{(L_g - L_y)/2} = \frac{D}{(L_g - L_y)}, \tag{3.1}$$

where $L_y(t)$ is the yarn length which is a time-dependent function.

Solving Eq. (3.1) for θ, we obtain:

$$\theta = 2\tan^{-1}(\frac{D}{L_g - L_y}). \tag{3.2}$$

That is, the relation between the cone angle and yarn length can be established as long as the diameter of brush (D) and the gap distance between two brushes (L_g) are known. Giving the experimental parameters: D = 1.4 cm and L_g = 13 cm (or 10 cm), the yarn length-cone angle curve corresponding to the experimental parameters was created (Figure 3.6b). Comparing Figure 3.5b and Figure 3.6b, one concludes that the experimental observation of the cone angle-yarn length dependence is in agreement with the geometrical model.

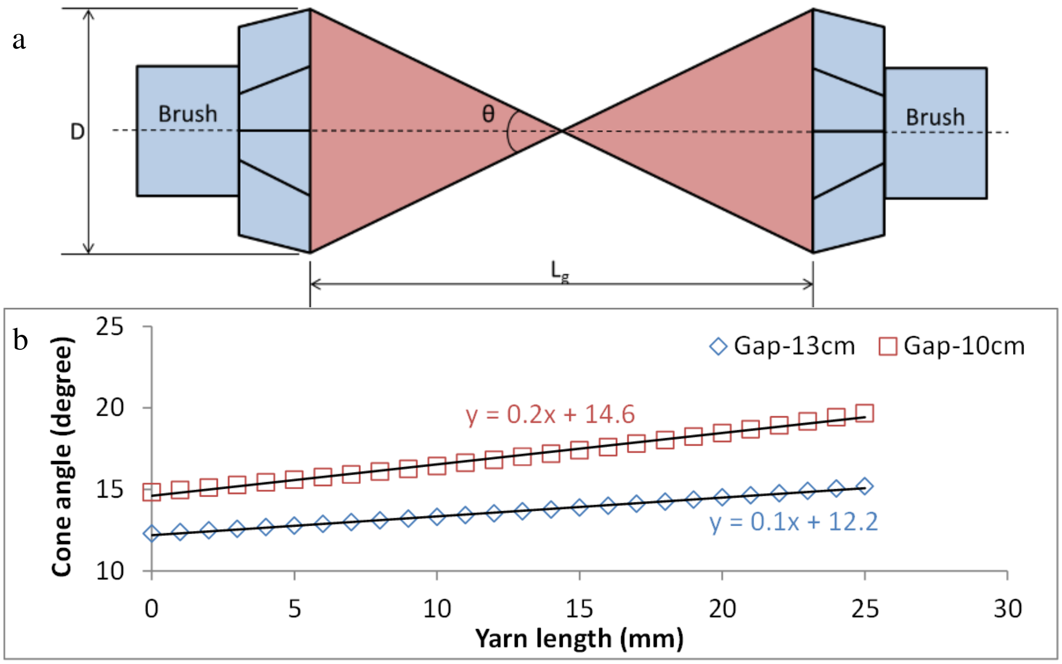

Figure 3.6. (a) Schematic diagram of the geometry of the twisting device. (b) The theoretical relation between cone angle and yarn length calculated from Eq. (3.2) corresponding to the experimental range yarn lengths.

This model can be used to estimate the yarn length-cone angle dependence when the yarn length is longer than 25 mm. As shown in Figure 3.7, the yarn length-cone angle relation significantly deviates from the linear dependence as the cone endpoints approach the brushes. Thus, the yarn density is expected to change as well. In practical applications, one needs to stay within the linear range of θ-L_y dependence ensuring yarn uniformity.

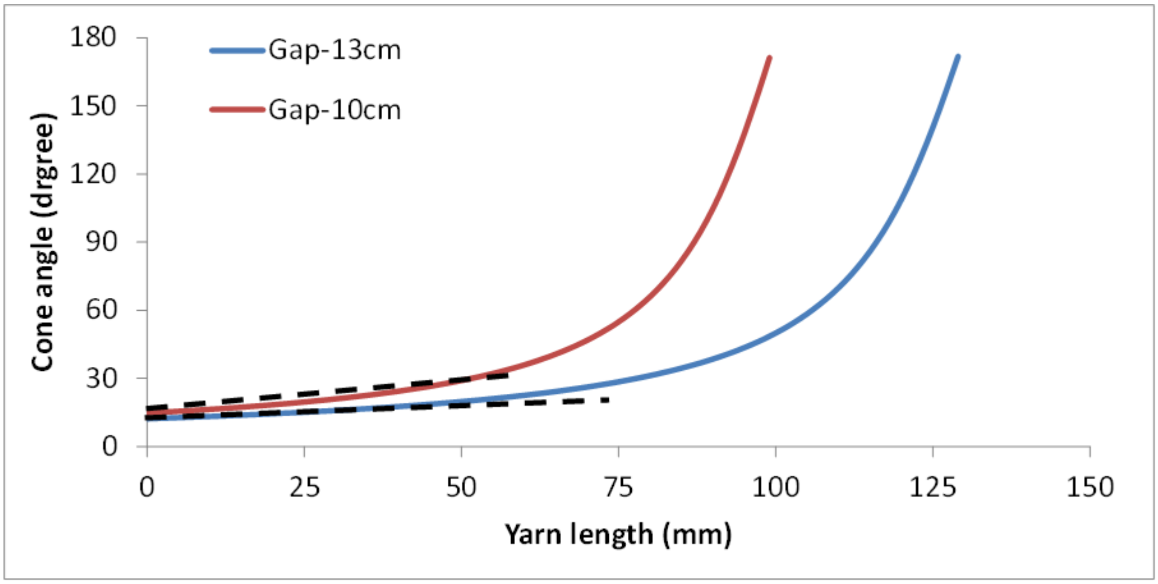

Figure 3.7. The theoretical relation between cone angle and yarn length calculated from Eq. (3.2).

3.6 A Library of Materials

Table 3.1 lists different polymers and their blends that were electrospun and twisted into yarns using the proposed protocol. Not all polymers can be twisted into yarn because of rigidity and poor elastic properties of the nanofibers. It was impossible to produce yarns from pure polyvinylidene fluoride (PVDF) and cellulose acetate (CA) nanofibers: the produced nanofibers broke as soon as a small twist was applied. Hence, certain amount of additives; for example, polyethylene oxide (PEO) or polymethyl methacrylate (PMMA), were added in order to produce longer fibers and yarns. Table 3.1 shows the experimental parameters: solvents, polymer concentrations, distance between needle and collector, applied voltage, flow rate, and the longest length of yarns which we were able to produce.

Table 3.1. The list of polymers which can be used for yarn formation with the proposed device[2].

Polymer	Solvent	Conc. (wt %)	Gap btw Needle and collector (cm)	Voltage (kV)	Flow Rate (ml/hr)	Yarn Length (cm)
CA/PEO	DMAc Acetone	8 ~ 17	20 ~ 30	6 ~ 8	0.2 ~ 0.8	10 ~ 15
CA/PMMA	DMAc Acetone	12 ~ 16	12 ~ 15	6 ~ 8	0.2 ~ 2.0	10 ~ 15
PAN/PMMA	DMAc Acetone	10 ~ 20	15 ~ 20	12 ~ 15	0.4 ~ 0.8	15 ~ 20
PAN/CA	DMAc Acetone	10 ~ 17	12 ~ 15	8 ~ 10	0.2 ~ 0.4	10 ~ 15
PVDF/PEO	DMAc (>50^{0}C)	12 ~ 18	30 ~ 40	9 ~ 13	0.2 ~ 0.4	15 ~ 20
PAN	DMAc	8 ~ 15	10 ~ 12	8 ~ 15	0.2 ~1.0	2 ~ 5
PMMA	DMAc MEK Acetone DCM	10 ~ 16	13 ~ 15	7 ~ 15	0.4 ~ 1.0	5 ~ 10
PEO	DMAc (>50^{0}C) Water	2 ~ 5	10 ~ 15	6 ~ 9	0.2 ~ 0.4	2 ~ 5
PVA	Water	10 ~ 16	10 ~ 14	15 ~ 18	0.2 ~ 0.4	5 ~ 10

PVA

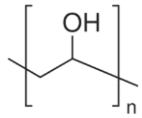

PEO

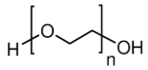

PAN

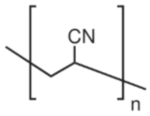

PMMA

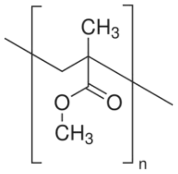

PVDF

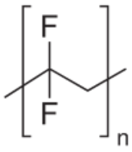

CA

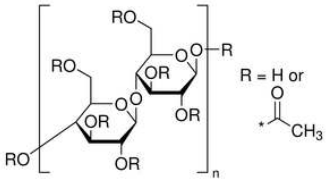

---

[2] Abbreviation: PEO: Poly(ethylene oxide); CA: Cellulose acetate; PMMA: Poly(methyl methacrylate); PAN: Polyacrylonitrile; PVA: Polyvinyl alcohol; PVDF: Polyvinylidene fluoride; DMAc: Dimethylacetamide; MEK: Methyl Ethyl Ketone; DCM: Dichlormethane.

3.7 Analysis of Electrospun Nanofiber Yarns

3.7.1 Yarn Diameters

Fibers on each pair of four bars of the rotating collector were collected and twisted into yarns yielding four yarns simultaneously. CA/PMMA fibers were produced by spinning one hour and 12 tpcm twists were applied to form the yarns. As shown in Figure 3.8, fibers in the produced yarn are highly oriented in the Z-twist type with ~70^0 angles.

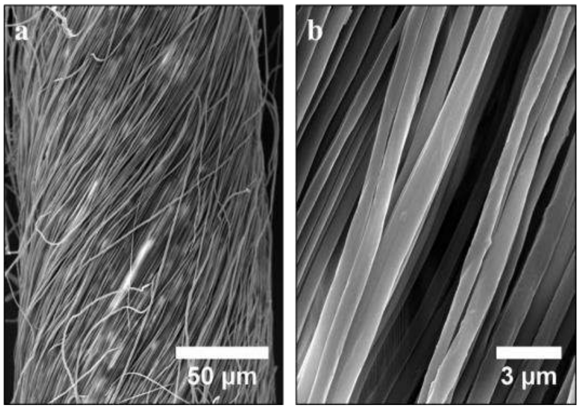

Figure 3.8. The SEM (FESEM-Hitachi 4800) micrographs of electrospun CA/PMMA yarns produced by the proposed method.

The first series of experiments was designed to confirm that the yarns can be made with the same diameters. Three materials, CA/PMMA, PAN/PMMA, and PVDF/PEO were used for the examination of yarn diameters. These yarns were prepared by electrospinning one hour and application of 12 tpcm twists. Four yarns were produced in each electrospinning run and their diameters were examined using the optical microscope (Olympus BX-51) at 10 points along each yarn. The average yarn diameter and standard deviations are presented in Figure 3.9a. It is clearly seen that the yarn diameters of each material are very consistent and the standard deviations are small. For example, the standard deviation of 200 µm yarns is only 5 µm which is about 1/40 of the yarn diameter.

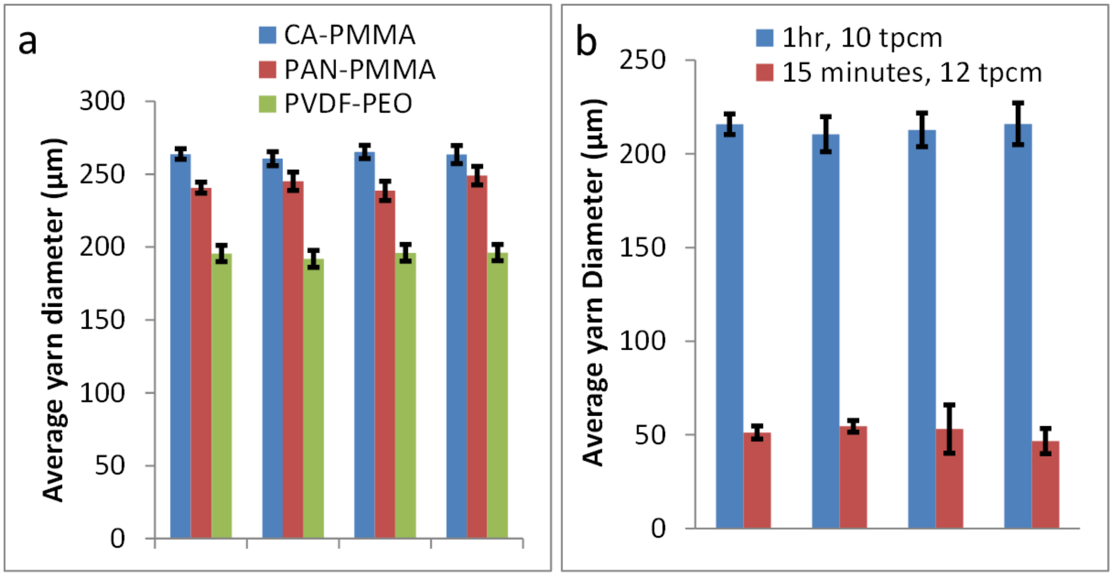

Figure 3.9. (a) The average diameters of CA/PMMA, PAN/PMMA, and PVDF/PEO yarns prepared by electrospinning one hour and application of 12 tpcm twists. The blue columns correspond to CA/PMMA yarns, the red columns correspond to PAN/PMMA yarns, and the green columns correspond to PVDF/PEO yarns. The error bars are the standard deviations. (b) The average diameters of PVDF/PEO yarns produced from the different collection times and number of twists applied to the yarns.

In the second series of experiments, the diameters of yarns produced at different collection times and number of twists were studied. The first experiment was set at the condition of 15 minutes collection following 12 tpcm twists applied to the yarns, and then the collection time was increased to one hour and 10 tpcm twist was applied to the yarns. Again, four yarns were examined using the optical microscope (Olympus BX-51) at 10 points along each yarn, and the average yarn diameter and standard deviations were reported. As shown in Figure 3.9b, the average yarn diameters are. The thicker the fiber band to start with, the easier it is to produce yarns with reproducible diameters. The thinnest reproducible yarns were 20 μm in diameter. These results show that the proposed device is able to fabricate yarns with controlled properties.

3.7.2 Elasticity

The tensile stress-strain test is the simplest mechanical test providing the Young's modulus of the material, and the strength characteristics of the yarns. Tensile stress-strain characteristics are determined by monitoring the force and the yarn elongation. The Young's modulus is usually defined at small strains where the stress-strain curve is approximately linear.

The stress σ is defined as:

$$\sigma = \frac{F}{A_0}, \tag{3.3}$$

where F is the force applied perpendicularly to the specimen cross-section and A_0 is the original cross-sectional area of the yarn before loading. Typical units of stress are megapascals, MPa (SI), or pounds force per square inch, psi.

The definition of strain ε is:

$$\varepsilon = \frac{l_i - l_0}{l_0} = \frac{\Delta l}{l}, \tag{3.4}$$

where l_0 is the original yarn length before loading and l_i is the yarn length under the load, and Δl is the yarn extension. The strain is unitless. It is common to express strain in percent:

$$\varepsilon(\%) = \frac{l_i - l_0}{l_0} \times 100 = \frac{\Delta l}{l} \times 100. \tag{3.5}$$

If stress and strain are proportional to each other:

$$\sigma = E\varepsilon , \tag{3.6}$$

one says that the material is linearly elastic. Eq. (3.6) is known as the Hooke's law, and the slope *E* (usually measured in GPa or psi) is the modulus of elasticity or Young's modulus. The greater the modulus, the stiffer the material.

Three materials, CA/PMMA, PAN/PMMA, and PVDF/PEO, were used for the examination of tensile properties of the yarns. These yarns were prepared by one hour fiber collection with 12 tpcm twists applied. An Instron machine (model 5582) was used in these experiments. The experimental procedure of American Society for Testing and Materials (ASTM D-3822, Standard Test Method for Tensile Properties of Single Textile Fibers) was employed. The yarns were cut and placed in the U-shaped frames (Figure 3.10) and each end was fixed with scotch tape. The prepared sample was mounted in the jaws clamps of the Instron machine without stretching the yarn. After the sample was fixed between the clamps, the U-shaped frame was cut in half leaving the testing yarn hung between the clamps. The crosshead speed was set 10 mm/min for all materials. Four yarns of each material were examined and the average breaking strength, elongation at break, and Young's modulus were collected and these results were presented in Table 3.2. As shown in Table 3.2, the yarns produced from the same materials have repeatable mechanical properties as demonstrated by their relatively small standard deviations.

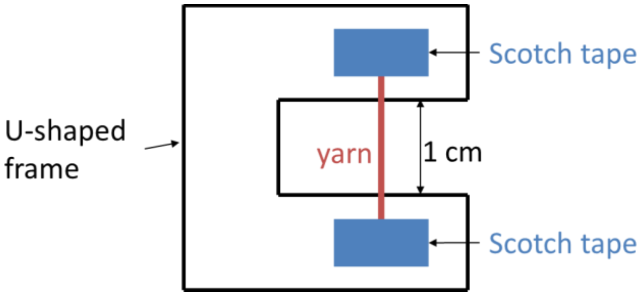

Figure 3.10. Schematic of the U-shaped frame.

Table 3.2. Summary of elastic properties of CA/PMMA, PAN/PMMA, and PVDF/PEO yarns. The data present the average ± standard deviations.

Material	Breaking Stress (MPa)	Elongation at break (%)	Young's Modulus (GPa)	Fiber diameter/ Yarn diameter
CA/PMMA	59.4 ± 3.7	49.1 ± 3.3	0.47 ± 0.03	~0.8 μm/260 μm
PAN/PMMA	24.7 ± 1.3	63.8 ± 2.6	0.44 ± 0.04	~1.5 μm/240 μm
PVDF/PEO	37.0 ± 1.2	458.1 ± 16.4	0.26 ± 0.03	~2 μm/200 μm

The stress-strain curves of the three different materials are presented in Figure 3.11. Three materials exhibited different stress-strain behavior. Both PAN/PMMA and CA/PMMA yarns can be stretched almost in 1.5 times while the PVDF/PEO yarns can be extended in 5.5 times. As mentioned in the previous section, pure PVDF fibers are rigid and it is difficult to twist them into yarns. After addition of PEO, longer fibers can be formed. Most likely, the viscoelastic properties of solution were significantly improved enabling one to electrospin longer fibers which can be further twisted into yarns [10]. Remarkably, the extension of the resulting PVDF/PEO yarn is much greater relative to that of the PAN/PMMA and CA/PMMA yarns. In particular, the modulus of PVDF/PEO yarns is decreased significantly to ~0.3 GPa which is much smaller than the modulus of pure PVDF fibers or films ~3.5 GPa [11, 12]. It is noticeable that the Young’s moduli of CA/PMMA, PAN/PMMA, and PVDF/PEO yarns were very close to each other as shown in the inset of Figure 3.11. This suggests that the yarn deformation at this range of loads is mostly caused by the nanofibers repacking within the yarn core. This hypothesis requires further analysis.

The tensile stress-stress curves of electrospun fiber yarns show that these yarns are much more elastic than textile fibers and yarns, which typically have Young's moduli measured in the gigapascals range [13, 14].

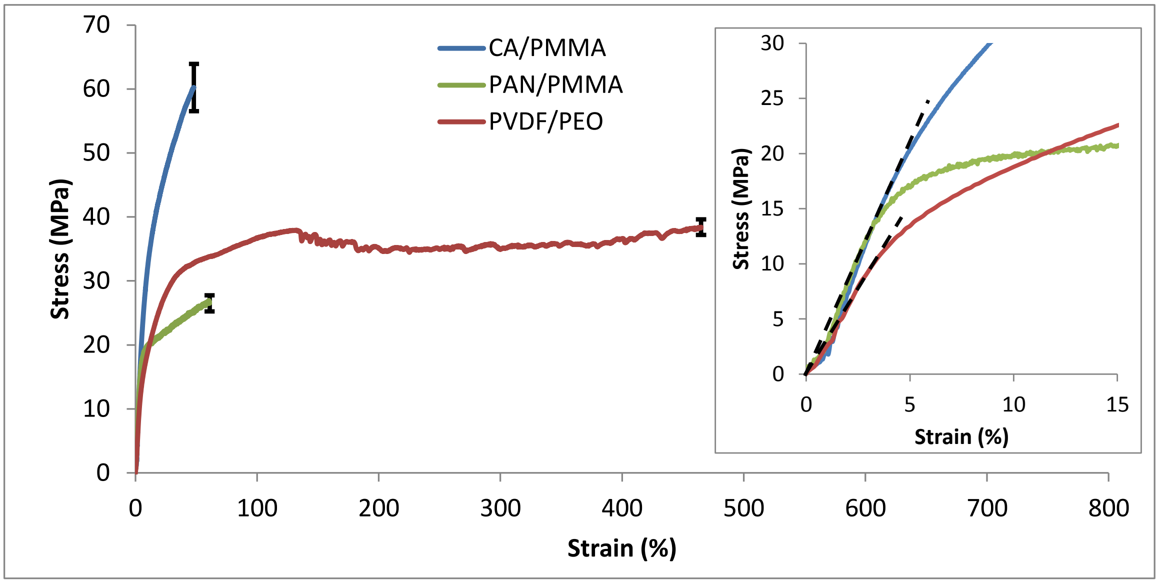

Figure 3.11. The experimental stress-strain curves of CA/PMMA, PAN/PMMA, and PVDF/PEO yarns. The inset presenting the linear stress-strain behavior, were used to calculate the Young's moduli.

3.7.3 Yarn Flexibility

As mentioned in the first chapter, the advantage of using polymeric nanofiber yarns as probe materials is that the probes can be manipulated with external fields. Therefore, the probe needs to be made from flexible materials.

As a measure of fiber flexibility, it is convenient to choose the inverse of the product, $f = 1/(MR) = 1/(EI_y)$. In this definition, the smaller the bending moment leading to the fiber bending, the greater the fiber flexibility. Also, the smaller the loop which this fiber can form, the greater its flexibility. As follows from Eq. (2.40), the flexibility of a cylindrical yarn is inversely proportional to the Young's modulus of the material (E) and the yarn radius (R_y) to the fourth power. The Young's modulus (E) and the yarn radius (R_y) were taken from Table 3.2, and the resulting yarn flexibility is presented in Table 3.3.

Table 3.3. Summary of flexibility of CA/PMMA, PAN/PMMA, and PVDF/PEO yarns. The data present the average ± standard deviations.

Material	**Flexibility ($N^{-1}m^{-2}$)**	**Porosity (%)**
CA/PMMA	$1.4 \pm 0.5 \times 10^7$	33 ± 3
PAN/PMMA	$2.4 \pm 0.2 \times 10^7$	59 ± 5
PVDF/PEO	$1.7 \pm 0.3 \times 10^8$	58 ± 1

Traditional textile fibers and yarns typically have Young's moduli measured in the gigapascals range [13, 14]. Therefore, the flexibility of electrospun yarns is much greater. That is, these yarns show a potential for their manipulation by external forces, such as electric or magnetic fields, and can be used as probes to grab hazardous liquids. For example, PVDF/PEO yarns are very flexible and easy to bend. Therefore, these yarns are excellent candidates for many flexible grabbers. The CA/PMMA and PAN/PMMA yarns are much stiffer than the PVDF/PEO yarns and hence suitable for the bioassay applications requiring punching and piecing tissue samples.

3.8 Methods and Materials

3.8.1 Polymer Solution Preparation

Polyacrylonitrile (PAN, MW=150 kDa), Polyethylene oxide (PEO, MW=1000 kDa), Cellulose acetate[3] (CA, MW: ~37 kDa), Polymethyl methacrylate (PMMA, MW: ~996 kDa) were obtained from Sigma-Aldrich. Polyvinylidene fluoride (PVDF) was purchased from Goodfellow. Dimethylacetamide (DMAc) was purchased from Alfa Aesar. All chemicals were used as received without further purification. DMAc was used as a solvent to prepare polymer solutions: a. 12.28 wt% CA/PMMA mixture with the CA/PMMA ratio = 5:2 (by weight); b. 19.35 wt% PAN/PMMA mixture with the PNA/PMMA ratio = 1:1; c. 18.03 wt% PVDF/PEO mixtures with the PVDF/PEO ratio = 10:1 (by weight).

3.8.2 Porosity (ε)

The porosity of different materials was estimated by the formula $\varepsilon = (m_w - m_d) / (\rho V_y)$, where m_w is the mass of wet yarn, m_d is the mass of dry yarn, ρ is the liquid density, and V_y is the yarn volume. The yarn volume was calculated as $V_y = \pi R_y^2 L_y$, where R_y is the radius of yarn which was measured by the optical microscope Olympus BX-51, and L_y is the length of the yarn. The yarn was placed vertically with one end sealed with plasticine and another end submersed in hexadecane. The mass change was measured by Cahn DCA-322 DCA analyzer. The porosity was examined on three samples for each material.

---

[3] The CA is actually cellulose diacetate with a degree of substitution (DS) of approximate 2.3.

3.9 Conclusions

A technique to fabricate electrospun fiber yarns was successfully developed by industrially scalable methods using a modified collector and a twisting device. Various polymer fibers were electrospun into ordered bands and subsequently twisted into yarns. The process of yarn formation was studied and compared with a geometrical model; the time dependence of the yarn length and cone angle was in agreement with theoretical calculations. The fibers in the produced yarns appeared oriented after twisting. The yarns produced were very uniform. The tensile properties of yarns were examined by Instron machine The measured mechanical characteristics of the yarns were very repeatable. The yarns appeared much more flexible comparing with the textile fibers and yarns. The results suggest that these electrospun yarns may have various applications in micro- and nano-mechanical devices. For example, to probe, one needs fibers flexible enable to penetrate capillaries and small pores; and PVDF/PEO yarns are the best candidates. For piercing tissue and for biopsy, one needs stiff materials preventing deformation during punching and piercing. Thus, CA/PMMA and PAN/PMMA yarns are the best candidates for these applications.

3.10 References

1. Lin, T., *Nanofibers - production, properties and functional applications*. 2011: InTech. 458 p.

2. Ramakrishna, S. and W.E. Teo, *A review on electrospinning design and nanofibre assemblies.* Nanotechnology, 2006. **17**(14): p. R89-R106.

3. Ali, U., Y.Q. Zhou, X.G. Wang, and T. Lin, *Direct electrospinning of highly twisted, continuous nanofiber yarns.* Journal of the Textile Institute, 2012. **103**(1): p. 80-88.

4. Dabirian, F., S.A.H. Ravandi, R.H. Sanatgar, and J.P. Hinestroza, *Manufacturing of Twisted Continuous PAN Nanofiber Yarn by Electrospinning Process.* Fibers and Polymers, 2011. **12**(5): p. 610-615.

5. Smit, E., U. Buttner, and R.D. Sanderson, *Continuous yarns from electrospun fibers.* Polymer, 2005. **46**(8): p. 2419-2423.

6. Zhou, F.L. and R.H. Gong, *Manufacturing technologies of polymeric nanofibres and nanofibre yarns.* Polymer International, 2008. **57**(6): p. 837-845.

7. Usman Ali, Y.Z., Xungai Wang, and Tong Lin, *Electrospinning of Continuous Nanofiber Bundles and Twisted Nanofiber Yarns, Nanofibers - Production, Properties and Functional Applications, Dr. Tong Lin*. 2011: InTech.

8. Li, D., Y.L. Wang, and Y.N. Xia, *Electrospinning of polymeric and ceramic nanofibers as uniaxially aligned arrays.* Nano Letters, 2003. **3**(8): p. 1167-1171.

9. Tsai, C.C., P. Mikes, T. Andrukh, E. White, D. Monaenkova, O. Burtovyy, R. Burtovyy, B. Rubin, D. Lukas, I. Luzinov, J.R. Owens, and K.G. Kornev, *Nanoporous artificial proboscis for probing minute amount of liquids.* Nanoscale, 2011. **3**(11): p. 4685-4695.

10. Bazilevsky, A.V., K.G. Kornev, A.N. Rozhkov, and A.V. Neimark, *Spontaneous absorption of viscous and viscoelastic fluids by capillaries and porous substrates.* Journal of Colloid and Interface Science, 2003. **262**(1): p. 16-24.

11. Du, C., B. Zhu, and Y. Xu, *Hard elasticity of poly(vinylidene fluoride) fibers.* Journal of Materials Science, 2005. **40**(4): p. 1035-1036.

12. Vinogradov, A. and F. Holloway, *Electro-mechanical properties of the piezoelectric polymer PVDF.* Ferroelectrics, 1999. **226**(1): p. 169-181.

13. Hongu, T., G.O. Phillips, and M. Takigami, *New millenium fibers*. 2005, Cambridge, England: Woodhead Publishing Ltd.

14. Lee, S.M., *Handbook of Composite Reinforcements*. 1992: Wiley.

CHAPTER FOUR

PERMEABILITY OF ELECTROSPUN FIBER YARNS

A novel technique was developed enabling determination of the permeability of electrospun yarns. Analyzing kinetics of liquid wicking into a yarn-in-a-tube composite conduit it was found that this kinetic is very specific and distinguishable. The liquid was pulled by the capillary pressure associated with the meniscus in the tube while the main resistance comes from the yarn. Therefore, the yarn permeability can be separated from the capillary pressure which cannot be done in wicking experiments with single yarns. Surface tensiometer (Cahn®) was employed to collect the data on wicking kinetics of hexadecane into the yarn-in-a-tube conduits. Yarns from different polymers and blends were electrospun and characterized using the proposed protocol. The permeability of electrospun yarns can be varied in a broad range from 10^{-14} m^2 to 10^{-12} m^2 by changing the fiber diameter and packing density.

4.1 Introduction

For probe applications, the controlled fluid wicking is the main concern. A detailed understanding of yarn wetting and wicking is required in order to develop probes with reproducible absorption properties. However, characterization of the transport properties of nanofiber yarns is a challenging task because of their size, geometry, and many other variables affecting the liquid transport in fibrous materials. This chapter discusses the characterization of transport properties of nanofiber yarns in terms of their permeability, which is the main factor affecting the fluid flow in a porous material. The permeability k can be considered as an characteristic of a porous material to transport fluids through it. Fluid flow through a porous medium can be described by Darcy's law (Figure 4.1), which relates the filtration velocity, q, with the pressure gradient, ∇P, and dynamic viscosity of the liquid, η [1, 2]:

$$q = \frac{Q}{A} = -\frac{k}{\eta} \nabla P, \tag{4.1}$$

where Q is the volumetric flow rate, A is the sample cross-sectional area through which the liquid is flowing, and k is the permeability of the porous medium. Figure 4.1 represents a schematic of fluid flow through a porous cylinder.

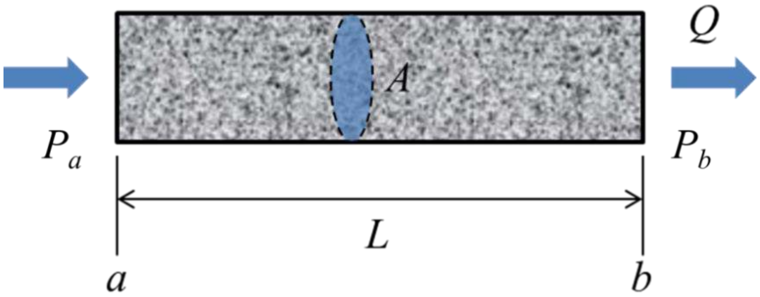

Figure 4.1. Fluid flow through a porous cylinder of length L is described by Darcy's law $Q/A = (k/\eta)(P_a - P_b)/L$. Q is the volumetric flow rate, A is the sample cross-sectional area through which the liquid is flowing, and the pressure gradient is expressed as $\nabla P = (P_b - P_a)/L$.

Nanofiber yarns are attractive candidates for probing of different liquids because they generate very high capillary pressure. In order to illustrate great potential of nanofiber yarns, consider a simple yarn model as a fiber bundle. Making this model even simpler, the interfiber channel is assumed cylindrical with radius R. Then the capillary pressure generated by a liquid meniscus is estimated as (see Chapter 2, Eq. (2.4)):

$$P_c = -2\sigma \cos\theta / R, \tag{4.2}$$

where σ is the surface tension of the liquid/air interface and θ is the contact angle that the meniscus makes with the channel wall. Therefore, when the yarn is dipped into a liquid, the meniscus at the wetting front pulls the liquid from the reservoir by creating a pressure drop P_c.

Combining Eq. (4.1) and Eq. (4.2), and expressing the volumetric flow rate as the velocity of the wetting front $Q = \varepsilon A dL/dt$, we obtain:

$$\varepsilon \frac{dL}{dt} = -\frac{kP_c}{\eta L} = \frac{2k\sigma\cos\theta}{\eta L R}, \tag{4.3}$$

where L is the wetting front position at time t and ε is the porosity of the yarn.

Eq. (4.3) can be immediately integrated to give the well-known Lucas-Washburn law [3, 4]:

$$L = \sqrt{\frac{2kP_c}{\varepsilon\eta}t} = 2\sqrt{\frac{k\sigma\cos\theta}{\varepsilon\eta R}t}\,. \tag{4.4}$$

As follows from Eq. (4.4), in order to interpret the experimental $L(t)$ dependency, one needs to know porosity ε, capillary pressure P_c, and permeability of the given yarn k. Conventional wicking experiments cannot independently provide the capillary pressure and permeability because these parameters cannot be separated in Eq. (4.4). Available experimental techniques assume dealing with large samples. In addition to their small size, nanofiber yarns pose another challenge: the capillary pressure created by the yarns becomes very high, making the analysis of the Jurin length problematic [5]. For example, a water column is supposed to reach 15 meters in a 2 μm diameter pore (Figure 2.5) indicating that the Jurin experiment cannot be used for characterization of these yarns. Recent progress in the electrospinning of nanofibers and nanofiber yarns calls for development of new characterization methods of their analyses.

This challenge is addressed by developing a novel technique enabling determination of the permeability of nanofiber yarns without knowing its capillary pressure. If one embeds the nanofiber yarn in a capillary letting a piece of yarn to stick out of the capillary, the yarn and capillary will work as a complex conduit with a composite permeability. This permeability can be directly evaluated from the same capillary rise experiment: one needs to fill the yarn with the liquid and let meniscus to propagate through the capillary. Meniscus position is determined by the yarn permeability k_y ($k_y = r^2/8$, where r is the capillary radius [1, 6]). The driving force for the capillary rise is the wetting force, $F_w = 2\pi r\sigma\cos\theta$, where θ is the contact angle that meniscus makes with the capillary wall. Thus, the driving force can be separated from the yarn permeability.

An engineering model was developed to describe this wicking experiment. The model leads to the Lucas-Washburn equation with the modified permeability. The model reveals interesting kinetics specific for the yarn-in-a-tube system allowing extraction of the yarn permeability directly from the wicking experiments. An experimental setup utilizing the capability of a Cahn surface tensiometer was developed. Different nanofiber yarns were electrospun and their permeabilities were measured using the proposed theory and experimental protocol. It has been shown that the technique of nanofiber yarn formation developed in Chapter 3 allows one to spin yarns with a wide range of permeability, from 10^{-14} to 10^{-12} m^2. The permeabilities of the tested CA/PMMA yarns were very close from one sample to another sample suggesting that the produced yarns have repeatable transport properties.

4.2 Experimental Setup

In order to analyze the permeability of electrospun fiber yarns, a setup schematically shown in Figure 4.2a was employed. Cahn DCA-322 Dynamic Contact Angle Analyzer was able to detect an incremental change of the sample weight with the 1 μg accuracy. A 5 mm long piece of an electrospun fiber yarn was cut with a razor blade, and the cut end was embedded into a capillary tube. The embedded part was approximately 1 mm long and the remaining 4 mm of the yarn stuck out from the capillary. The tube holding the yarn was then freely hung on the loop A of the Cahn balance arm (Figure 4.2a). A schematic of the mechanical principle of force measurement by Cahn DCA-322 Analyzer is shown in Figure 4.2a. There are two loops used for weight measurements (loop A and loop B). Loop A is more sensitive and can measure a force up to 150 mg force; loop B is less sensitive and can measure a force up to 750 mg force. A reference weight placed on loop C is used to counter balance the sample weight providing maximum sensitivity to the system. The ratio of the weights on three loops of the instrument was chosen as follows: loop A: loop B: loop C = 1: 5: 1 meaning that 100 mg weight on loop A or loop C creates the same amount of torque as that of 500 mg weight on loop B.

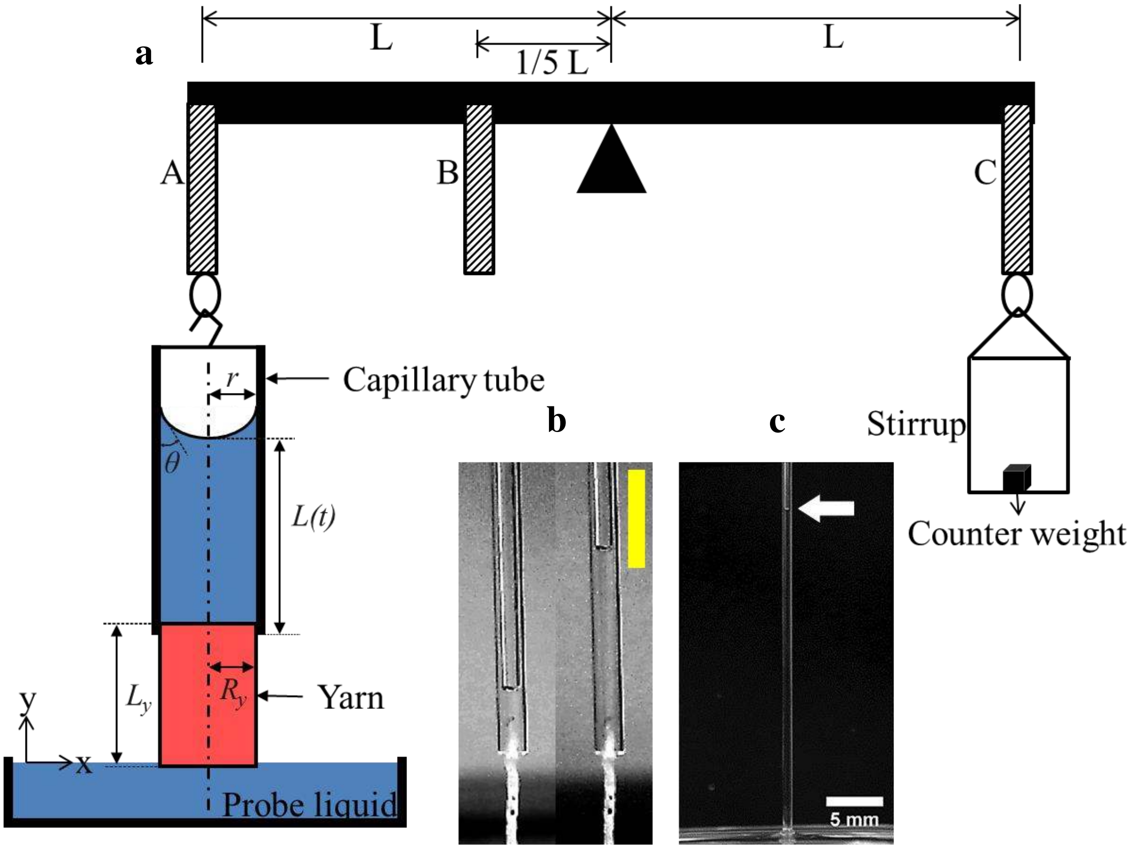

Figure 4.2. (a) A schematic of the experimental setup showing the principle of operation of Cahn DCA-322 Analyzer. A capillary tube with embedded yarn is connected to the balance arm through a hook. The weight of the absorbed liquid is measured by the balance arm as the meniscus crawls up the capillary bore. (b) The position of liquid meniscus before and after wicking experiments. Scale bar is 2 mm. (c) An example of measurement of Jurin length (Z_c) which is shown as the white arrow.

4.3 Data Acquisition

The free end of capillary tube was attached to the hook on loop A of the Cahn DCA-322 Analyzer, the other end of the tube holding the yarn was set suspended above the free liquid surface. The stage with the liquid container moving up at the speed of 200 μm per second, the free end of the yarn was brought to in contact with the liquid surface.

A special function of Cahn DCA-322 analyzer software, called the Zero Depth of Immersion (ZDOI), can set the starting moment of weight measurements. The ZDOI point was chosen as the moment the end of yarn first touched the liquid surface. This was experimentally found by setting a minimum force threshold at the F_{min} = 500 μgf level. With this choice of the ZDOI point, the stage with the liquid kept moving up if the measured force was less than 500 μgf. The balance was first zeroed, and the force was kept at the zero level when the stage was moved up (Figure 4.3). When the yarn touched the liquid surface, the force jumped up reflecting the action of the wetting force (red arrow in Figure 4.3) which appeared significantly larger than the ZDOI threshold [7]. When the yarn first touched the liquid surface and the measured force became greater than F_{min}, the stage continued to raise up 0.1 mm with 200 μm/sec speed to confirm that the yarn was immersed in liquid. A negative slope in Figure 4.3 is associated with the immersion process and it is caused by the increase of the buoyancy and viscous friction forces at the meniscus when the yarn gets immersed into liquid [7]. Then, the stage position was fixed. Stabilization of the entire setup required five minutes; then the force change was acquired for the next 50 minutes, red line in Figure 4.3.

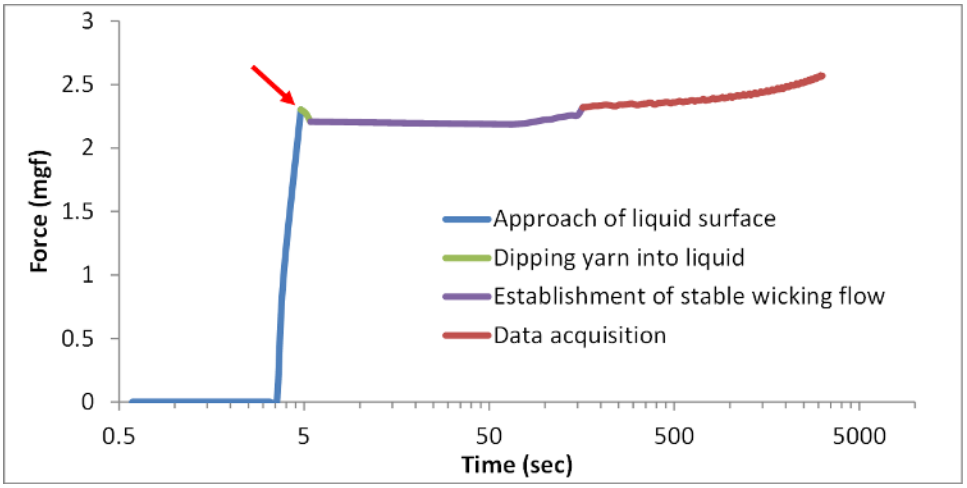

Figure 4.3. A typical experimental curve showing force changes at different steps: a steep jump of the blue line allows one to define the ZDOI point. The stage was moving until the immersed part reached 0.1 mm (green line), then we waited for 5 minutes (purple line), and started collecting the change of water weight for 50 minutes (red line).

After the stage position was fixed, a meniscus was observed inside the capillary (Figure 4.2b) and all incremental changes of force detected by the analyzer were attributed to the incremental change of weight of the liquid column invading the tube due to capillary action.

4.4 Model of Fluid Uptake by a Yarn-In-A-Tube Composite Conduit

4.4.1 The Liquid Discharge through the Yarn (Q_1)

The center of Cartesian coordinates is taken at the liquid surface with the *y*-axis pointing upwards (Figure 4.2). The flow is assumed one-dimensional with non-zero velocity component directed along the yarn and capillary axes. It is convenient to introduce a flow potential Φ as the sum of the pressure in liquid, *P(y),* at the position *y*, and hydrostatic pressure due to weight of the liquid column:

$$\Phi = P(y) + \rho g y, \tag{4.5}$$

where ρ is the liquid density and g is acceleration due to gravity.

In this definition, the pressure at the liquid surface is zero and the potential is zero as well. Therefore, Darcy's law is written through the flow potential as $Q = -(k_y A/\eta)(\partial\Phi/\partial y)$, where k_y is the permeability of the yarn, η is the liquid viscosity, $\partial\Phi/\partial y$ is the potential gradient taken along the yarn, and $A = \pi R_y^2$ is the cross-sectional area of the yarn of radius R_y.

The liquid is assumed not volatile (eg. Hexadecane, vapor pressure: 1 mmHg @ 105°C), hence, the mass conservation equation reads $\partial Q_y/\partial y = \partial^2\Phi_y/\partial y^2 = 0$. Integrating this equation, one obtains the linear distribution of the potential along the liquid column, $\Phi_y = ay + b$, where a and b are time-dependent functions that can be found from the boundary conditions. The boundary conditions state that the pressure at the liquid surface, $y = 0$, is equal to zero, hence $b = 0$. At the embedded end of the yarn $y = L_y$, $P_y + \rho g L_y = aL_y$. From this equation, it follows that $a = (P_y + \rho g L_y)/L_y$. With the obtained constants, the liquid discharge through the yarn is expressed as:

$$Q_1 = -\frac{\pi R_y^2 k_y}{\eta}\left(\frac{P_y + \rho g L_y}{L_y}\right). \tag{4.6}$$

4.4.2 The Liquid Discharge through the Capillary (Q_2)

The flow of the liquid column through the capillary can be described by the Hagen–Poiseuille law [6] which is written in Darcy's form as $Q_2 = -\left(k_c A/\eta\right)\left(\partial\Phi_c/\partial y\right)$ with $k_c = r^2/8$. Subscript "c" refers to the capillary. Once again, using the mass conservation equation, we obtain $\partial Q_c/\partial y = \partial^2\Phi_c/\partial y^2 = 0$. Integrating this equation, one infers the linear distribution of the potential along the liquid column, $\Phi_c = cy + d$, where c and d are time-dependent functions that can be found from the boundary conditions. The boundary conditions state that the pressure at the embedded end of yarn must be equal to the pressure in the liquid column at the same position $y = L_y$. Therefore, $P_y + \rho g L_y = cL_y + d$. At the wetting front $y = L(t)$, the pressure is below atmospheric pressure and the jump is equal to capillary pressure P_c. From this equation it follows that $-P_c + \rho g L = cL + d$. From these two boundary conditions it follows that $c = (P_y + P_c + \rho g[L_y - L])/[L_y - L]$ and $d = P_y + \rho g L_y - (P_y + P_c + \rho g[L_y - L])L_y/[L_y - L]$. With the obtained constants, the liquid discharge through the capillary is expressed as:

$$Q_2 = -\left(k_c A/\eta\right)c = -\frac{\pi r^4}{8\eta}(P_y + P_c + \rho g[L_y - L])/[L_y - L]. \tag{4.7}$$

4.4.3 Meniscus Motion through Capillary

The liquid discharge through the capillary is the same as that given by Eq. (4.7). Once again, the conservation of mass requires the following equality $Q_1 = Q_2$,

$$-\frac{\pi R_y^2 k_y}{\eta}\left(\frac{P_y + \rho g L_y}{L_y}\right) = -\frac{\pi r^4}{8\eta}(P_y + P_c + \rho g[L_y - L])/[L_y - L]. \tag{4.8}$$

Solving Eq. (4.8) for P_y, we can express pressure P_y through the meniscus position $L(t)$:

$$P_y = \left(\frac{\dfrac{r^4}{8(L_y - L)}}{\dfrac{R_y^2 k_y}{L_y} - \dfrac{r^4}{8(L_y - L)}} \right) \left[P_c + \rho g (L_y - L) - \frac{8\rho g R_y^2 k_y (L_y - L)}{r^4} \right]. \tag{4.9}$$

Plugging Eq. (4.9) into Eq. (4.7) and expressing its left hand side through the meniscus velocity $Q_2 = \pi r^2 dL/dt$, we obtain the basic equation describing kinetics of meniscus propagation through the capillary:

$$\frac{dL}{dt} = \frac{r^2}{8\eta} \frac{\left(P_c - \rho g L\right)}{L - L_y + \dfrac{r^4 L_y}{8R_y^2 k_y}}. \tag{4.10}$$

4.4.4 Engineering Parameters of Yarns

Eq. (4.10) contains many geometrical and physical parameters. This equation can be significantly simplified by introducing dimensionless variables. In order to see this, we normalize the meniscus position by the Jurin length Z_c which is defined as the maximum possible height of the liquid column coexisting with the liquid reservoir [5], $Z_c = P_c/\rho g = 2\sigma\cos\theta/(\rho g r)$. The time in Eq. (4.10) is convenient to normalize by the following characteristic time:

$$t_0 = \frac{8\eta Z_c}{\rho g r^2} = \frac{8\eta P_c}{\rho^2 g^2 r^2}. \tag{4.11}$$

This time is approximately equal to the time required for a liquid meniscus to reach the Jurin height. As seen from Eq. (4.11), this time depends on fluid viscosity η. With this normalization, $L^* = L/Z_c$, $t^* = t/t_0$, Eq. (4.10) is rewritten as:

$$\frac{dL^*}{dt^*} = \frac{1-L^*}{L^*+\alpha}, \tag{4.12}$$

where

$$\alpha = \frac{r^4 L_y}{8 Z_c R_y^2 k_y} - \frac{L_y}{Z_c}. \tag{4.13}$$

If the yarn length is much smaller than the Jurin length ($L_y << Z_c$), the effect of gravity, the second term on the right-hand side of Eq. (4.13), can be neglected, and Eq. (4.13) is simplified as:

$$\alpha = \frac{r^4 L_y}{8 Z_c R_y^2 k_y}. \tag{4.14}$$

Eq. (4.12) is a familiar Lucas-Washburn equation describing capillary rise in the tubes [3, 4], which has the solution:

$$-L^* - (1+\alpha)\ln(1-L^*) = t^*. \tag{4.15}$$

Thus, using the introduced normalization, one can interpret the experimental data in a much easier way by first measuring the Jurin length Z_c then calculating the characteristic time t_0 and then fitting the experimental curve $L^*(t^*)$ adjusting parameter α. After determination of this parameter α, the permeability of the yarn is calculated as:

$$k_y = \frac{L_y r^4}{8\alpha Z_c R_y^2}\,. \tag{4.16}$$

4.4.5 The Effect of Parameter *α* on Capillary Rise Kinetics

Using the introduced normalization, all physical parameters are collapsed into a dimensionless parameter α. The dimensionless parameter α can be considered as the ratio of the liquid discharge through the capillary tube (Q_2) to the liquid discharge through the yarn (Q_1). That is, the larger the α, the smaller the permeability, provided that the sizes of yarn and capillary do not change.

It appears that the nonlinear kinetic equation for liquid uptake by the yarn-in-a-tube conduit significantly depends on parameter α. Figure 4.4 shows the dependence of the normalized meniscus position (L^*) on the normalized time (t^*) at different parameters α. For $\alpha > 5{,}000$, the wicking kinetics can be considered linear with the time range of interest. On the other hand, for $\alpha < 5{,}000$, the kinetics of liquid imbibition becomes nonlinear.

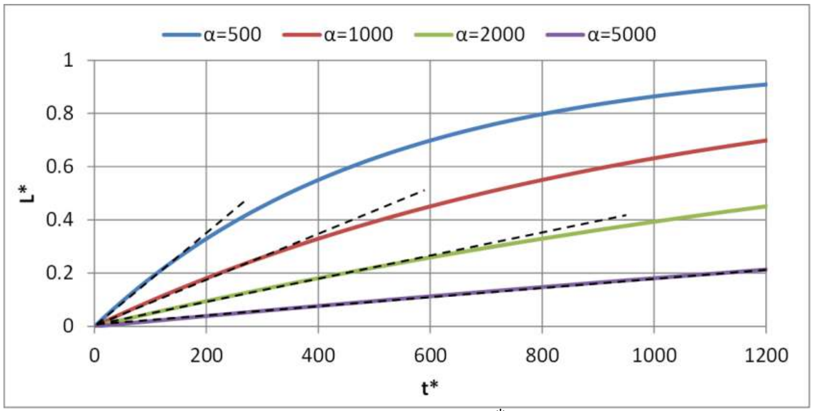

Figure 4.4.The normalized liquid front position (L^*) versus the normalized time (t^*) for the different values of parameter α. $t^* = t/t_0$, $L^* = L/Z_c$.

4.5 Results

4.5.1 Analysis of Experimental Data

The weight gain (ΔW) increasing with time t was acquired by the Cahn DCA-322 Analyzer. Therefore, the weight gain $W(t)$ was converted to dimensionless length $L^*(t^*)$. The meniscus position L at time t is written as $L = \Delta V/\pi r^2 = \Delta W/\rho\pi r^2$, where ρ is the liquid density and r is the capillary radius. Then L was divided by Z_c to obtain L^*, and t was divided by t_0 to obtain t^*. The Jurin length was measured in an independent experiment (Figure 4.2c) and for hexadecane it was $Z_c = 0.029$ m. The characteristic time t_0 was calculated using Eq. (4.11), for hexadecane, it was estimated as ~ 2.32 seconds. Figure 4.5 shows the typical curves of dimensionless meniscus position (L^*) versus dimensionless time (t^*) from different materials acquired by the DCA-322 analyzer. For samples of $L_y = 5$ mm long, α parameters of different materials were obtained by using a Matlab code by fitting the experimental data, black solid lines in Figure 4.5 correspond to the fitting curves.

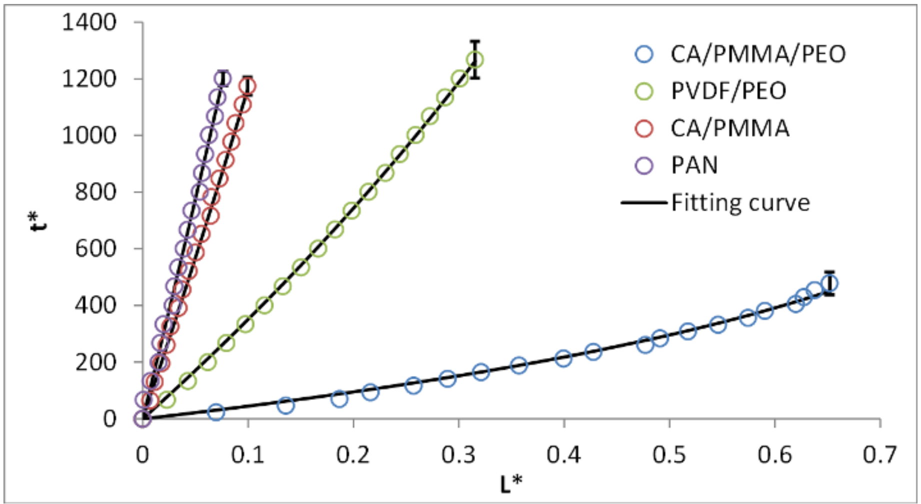

Figure 4.5. The dimensionless meniscus position (L^*) versus dimensionless time (t^*) in the yarn-in-a-tube conduit. The black solid lines represent the fitting curves.

Taking CA/PMMA/PEO as an example and using $Z_c = 0.029$ m, $r = 200$ μm, $R_y = 138$ μm, $L_y = 5$ mm, one obtains $\alpha \approx 431$ and consequently, the permeability k_y was calculated by Eq. (4.16) as $k_y = 4.15 \times 10^{-12}$ m^2. Four experiments were conducted and the average permeability was found as $k_y = 4.2 \pm 0.6 \times 10^{-12}$ m^2. The scaling arguments based on the Hagen-Poiseuille law suggest that the interfiber distance (d) of the yarn can be estimated as $d \sim (8k)^{1/2} \sim 6$ μm. The same procedures were used to calculate the permeability of other materials, and a summary of the obtained results is presented in Figure 4.6. The results show that the permeability spreads over two order of magnitudes from 10^{-14} to 10^{-12} m^2. For example, the permeability of CA/PMMA/PEO yarns is almost fifty-times larger than that of the PAN yarns. During the yarn formation, 12 turns per centimeter twist was applied to these materials. The SEM micrographs of these four materials were examined to reveal the effect of the fiber diameters (D_f) on the yarn permeability. ImageJ (NIH) was used to analyze the fiber diameters and interfiber distance.

Porosity was calculated as $\varepsilon = V_p/V_y$, where V_p is the pore volume and V_y is the yarn volume. The pore volume was estimated as $V_p = (m_w\text{-}m_d)/\rho$, where m_w is the mass of wet yarn, m_d is the mass of dry yarn, ρ is the liquid density. The mass of dry and wet samples was measured using Cahn DCA-322 Analyzer (see Methods). A summary of the results is presented in Figure 4.6.

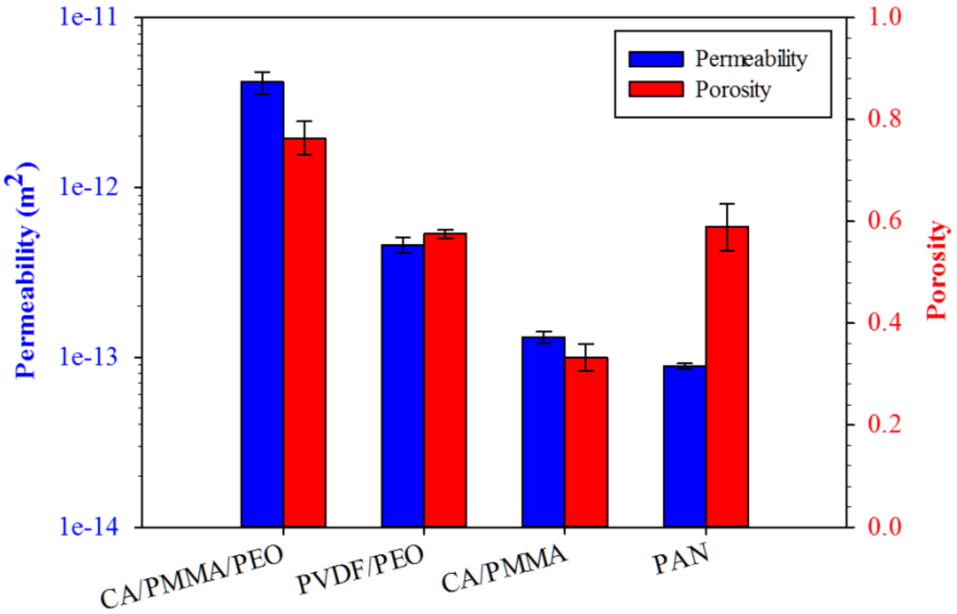

Figure 4.6. A summary of permeabilities and porosities of different materials. The *y* axis of permeability is represented in logarithmic scale, and error bars are the standard deviations.

Table 4.1. A summary of parameter α, permeability k_y, interfiber distance *d*, and fiber diameter D_f of different materials.

	α	k_y (m^2)	*d* (µm)	D_f (µm)
CA/PMMA/PEO	431 ± 58	$4.2 \pm 0.6 \times 10^{-12}$	5.8 ± 0.4	~6
PVDF/PEO	3752 ± 390	$4.6 \pm 0.5 \times 10^{-13}$	1.9 ± 0.1	~2
CA/PMMA	14098 ± 696	$1.3 \pm 0.1 \times 10^{-13}$	1.0 ± 0.04	~1
PAN	15248 ± 568	$8.8 \pm 0.3 \times 10^{-14}$	0.8 ± 0.02	~0.6

As shown in Figure 4.7, the interfiber distance is proportional to the fiber diameter. This tendency shows that when the fiber diameter is increased, the interfiber distance is also increased. As follows from Figure 4.7E, the interfiber distance (*d*) is almost equal to the fiber diameter (D_f), $d \approx D_f$. Since $d \sim (8k_y)^{1/2}$, we found that the permeability is $k_y \sim D_f^2/8$.

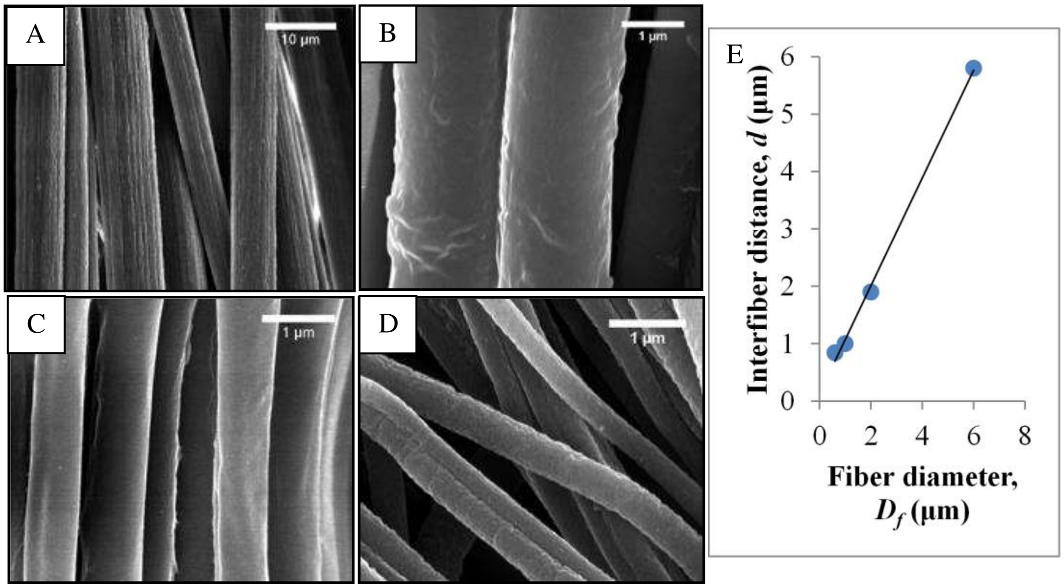

Figure 4.7. The SEM micrographs of electrospun fiber yarns: (A) CA/PMMA/PEO, fiber diameters $D_f \sim$ 6μm, (B) PVDF/PEO, fiber diameters $D_f \sim$ 2μm, (C) CA/PMMA, fiber diameters $D_f \sim$ 1μm, and (d) PAN, fiber diameters $D_f \sim$ 0.6μm. (e) The corresponding relation between the interfiber distance (*d*) and fiber diameter (D_f).

4.5.2 Reproducible Permeability

Figure 4.8 is the permeability for four electrospun CA/PMMA nanofiber yarns produced during one hour fiber electrospinning time followed by application of a 12 tpcm twist. Three more samples of each yarn were examined, and a summary of the obtained results is given in Figure 4.8. It is clearly seen that the permeabilities are close to each other, suggesting that the yarn properties are very repeatable from one sample to another. These results confirm that electrospun fiber yarns produced by the experimental protocol in Chapter 3 have the reproducible properties. The electrospinning time and applied twist are the main parameters controlling the yarn properties.

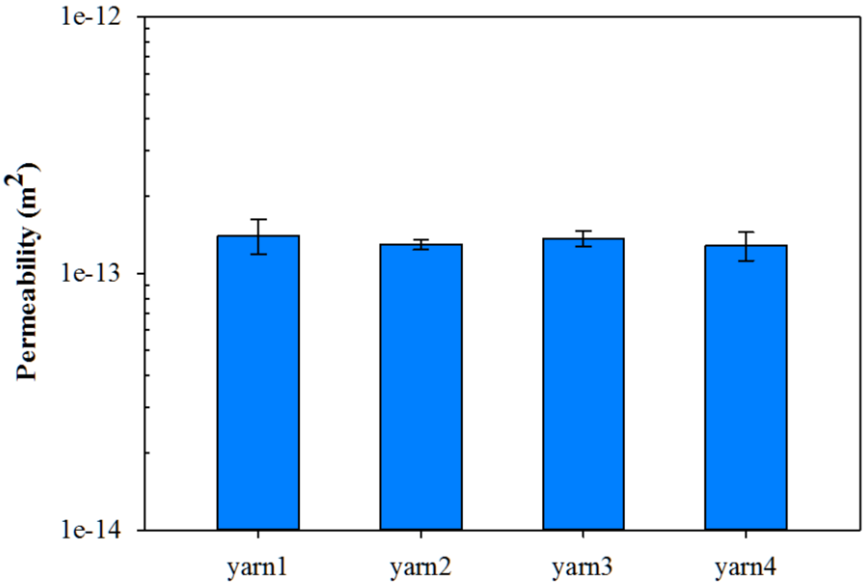

Figure 4.8. The permeability of four electrospun CA/PMMA nanofiber yarns. The *y* axis is presented in the logarithmic scale and error bars correspond to the standard deviations.

4.6 Methods and Materials

4.6.1 Polymer Solution Preparation

Polyacrylonitrile (PAN, MW=150 kDa), Polyethylene oxide (PEO, MW=1000 kDa), Cellulose acetate (CA, MW: ~37 kDa), Polymethyl methacrylate (PMMA, MW: ~996 kDa) were obtained from Sigma-Aldrich. Polyvinylidene fluoride (PVDF) was purchased from Goodfellow. Dimethylacetamide (DMAc) was purchased from Alfa Aesar. All chemicals were used as received without further purification. DMAc was used as a solvent to prepare polymer solutions: a. 12.28 wt% CA/PMMA mixture with the CA/PMMA ratio= 5:2 (by weight); b. 10 wt% PAN; c. 13.42 wt% CA/PMMA/PEO mixture with the CA/PMMA/PEO ratio =8:5:2 (by weight); d. 18.03 wt% PVDF/PEO mixtures with the PVDF/PEO ratio =10:1 (by weight).

4.6.2 Yarn Formation

The yarns were formed by using the method of Tsai et. al. [8]. The prepared polymer solutions were placed in a 10 mL syringe. A syringe pump (New Era Pump System, NE-300) was used to control the flow rate. A home-made rotating mandrel with four alumina bars separated from each other by 20 cm was used as a fiber collector [8]. A high voltage power supply (Glassman High Voltage, Inc.) was connected to the syringe through a stainless-steel needle (Gauge 20, EXEL). The needle was placed 15 cm apart from the nearest face of the collector. A positive voltage was applied to the needle until the Taylor cone was produced. When the nanofibers were collected on the mandrel, a home-made collecting and twisting device to form yarns was employed [8]. The twisting device consists of two circular wire brushes with the ¾ inches diameter each, mounted co-axially on the holder [8]. 12 turns per centimeter (tpcm) twist was applied to the yarns. It has been demonstrated the electrospinning time and number of twists are the main parameters controlling the yarn properties (diameter, porosity, and permeability) [8].

4.6.3 SEM Characterization

The surface morphology of the CA/PMMA, PAN, PVDF/PEO, and CA/PMMA/PEO fibers and yarns were examined with a Hitachi Field Emission scanning electron microscope (FESEM-Hitachi 4800). The samples were sputter-coated with a few nanometer thickness of gold prior to SEM examination.

4.6.4 Surface Tension

The surface tension of hexadecane was measured using Wilhelmy Plate method using Cahn DCA-322 DCA analyzer. A platinum wire with a 250 μm diameter was used as the standard probe. The platinum wire was cleaned with ethanol and an oxidizing flame to heat it to red-hot. The Wilhelmy equation $F= \sigma P$ was used to evaluate the surface tension, where F is the measured force, σ is the surface tension of the liquid, P is the perimeter of the wire. Hexadecane was examined three times and gave the surface tension $\sigma = 23.5 \pm 0.2$ mN/m.

4.6.5 Jurin Length (Z_c)

To use the dimensionless parameters L^* and t^*, one needs to know the Jurin length (Z_c). The Jurin length of Hexadecane (η = 3.03 cp, ρ = 773 kg/m^3) was determined by measuring the equilibrium height of liquid column in the capillary tube. A glass capillary tube with 200 μm in radius (r) was used in these experiments. Three experiments were conducted and the average Jurin length was measured as $Z_c = 0.029 \pm 0.0003$ m. The characteristic time t_0 was calculated using Eq. (4.11), $t_0 = 2.32$ seconds.

4.6.6 Porosity (ε)

The porosity of different materials was estimated by the formula $\varepsilon = (m_w\text{-}m_d) / (\rho V_y)$, where m_w is the mass of wet yarn, m_d is the mass of dry yarn, ρ is the liquid density, and V_y is the yarn volume. The yarn volume was calculated as $V_y = \pi R_y^2 L_y$, where R_y is the radius of yarn which was measured by the optical microscope Olympus BX-51, and

L_y is the length of the yarn. The yarn was placed vertically with one end sealed with plasticine and another end submersed in hexadecane. The mass change was measured by Cahn DCA-322 DCA analyzer. The porosity was examined on three samples for each material.

4.6.7 Reynolds Number (Re)

The Hagen-Poiseuille equation was used to describe the liquid flow in a cylindrical tube. The assumptions are the fluid is viscous and incompressible, and the flow is laminar. For a flow in a pipe or tube, the Reynolds number is defined as:

$$\mathrm{Re} = \frac{\rho v D}{\eta}, \tag{4.17}$$

where ρ is the liquid density, v is the mean liquid velocity, D is the hydraulic diameter of the pipe, and η is the liquid viscosity.

The Reynolds number is a dimensionless parameter and represents the ratio of inertial forces to viscous forces. High values of the parameter indicate that the viscous forces are small and the flow is controlled by inertia. In the opposite case, the flow is controlled by viscosity. Darcy’s law requires that the flow at the level of pores must be laminar and Reynolds numbers must be small.

In order to check the validity of the Hagen-Poiseuille equation used in our system, the Reynolds number (Re) was calculated using experimental parameters. Eq. (4.17) expresses the kinetics of meniscus propagation through the capillary, and the meniscus velocity was taken as the liquid velocity *dL/dt* in the Eq. (4.10). The Reynolds number becomes a time dependent function. The Reynolds numbers for the different materials were calculated and are summarized in Figure 4.9. As shown in Figure 4.9, the assumption of laminar flow in our system is valid.

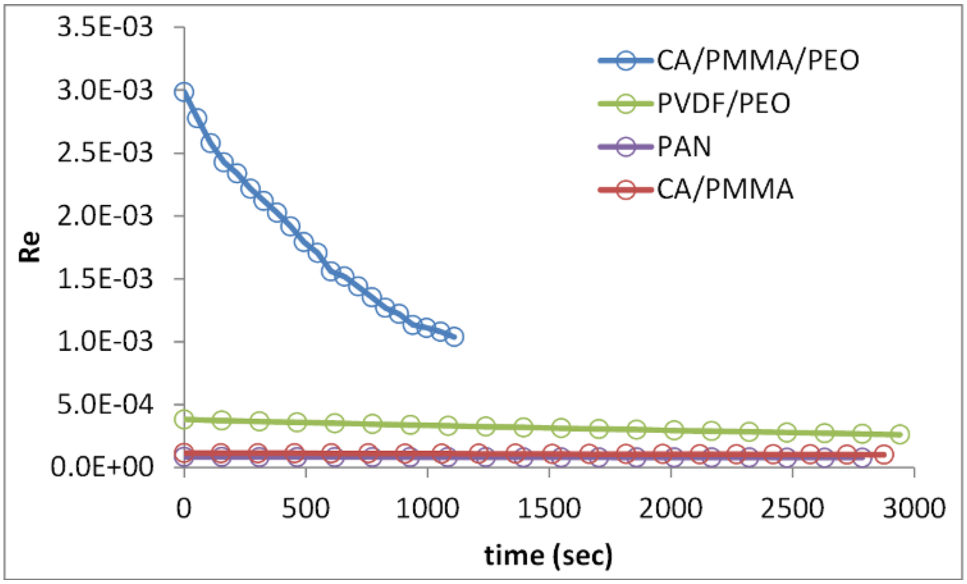

Figure 4.9. The Reynolds number versus time for hexadecane: $\eta = 3.03$ mPa·s, $\rho = 773$ kg/m^3.

4.7 Conclusions

A characterization technique was developed enabling to specify the permeability of electrospun yarns using wicking experiments on complex conduits made of yarn-in-a-tube pairs. This method takes advantage of the distinctive capillary pressure produced by the meniscus in a tube; this pressure is significantly different from the capillary pressure produced by menisci in the pores of the yarn. Therefore, the driving capillary pressure does not depend on the pore size and can be measured independently using the Jurin capillary rise technique. A mathematical model describing the kinetics of wicking of wetting liquids into yarn-in-a-tube conduit was developed and used for interpretation of experiments. Yarns from CA/PMMA, PAN, PVDF/PEO, and CA/PMMA/PEO were electrospun and characterized using the proposed technique. The produced yarns showed permeability spinning two orders of magnitude (10^{-14}~10^{-12} m^2).

4.8 References

1. Scheidegger, A.E., *The physics of flow through porous media*. 1957: University of Toronto Press.

2. Adamson, A.W. and A.P. Gast. *Physical chemistry of surfaces*. 1997.

3. Lucas, R., *Ueber das Zeitgesetz des kapillaren Aufstiegs von Flussigkeiten.* Kolloid Zeitschrift, 1918. **23**: p. 15-22.

4. Washburn, E., *The Dynamics of Capillary Flow.* Phys. Rev. Physical Review, 1921. **17**(3): p. 273-283.

5. Jurin, J., *An account of some experiments shown before the Royal Society; with an enquiry into the cause of the ascent and suspension of water in capillary tubes.* Philosophical Transactions of the Royal Society, 1917-1919. **30**(351-363): p. 739-747.

6. Adamson, A.W. and A.P. Gast, *Physical chemistry of surfaces*. 1997, New York: Wiley.

7. Miller, B., L.S. Penn, and S. Hedvat, *Wetting force measurements on single fibers.* Colloids and Surfaces, 1983. **6**(1): p. 49-61.

8. Tsai, C.C., P. Mikes, T. Andrukh, E. White, D. Monaenkova, O. Burtovyy, R. Burtovyy, B. Rubin, D. Lukas, I. Luzinov, J.R. Owens, and K.G. Kornev, *Nanoporous artificial proboscis for probing minute amount of liquids.* Nanoscale, 2011. **3**(11): p. 4685-4695.

CHAPTER FIVE

WETTING PROPERTIES OF ELECTROSPUN YARNS

Wetting properties of CA/PMMA yarns and their constituent films were studied in this chapter. The contact angles of flat films were measured by the sessile drop technique while the contact angles of electrospun yarns were characterized by the capillary rise method. The contact angles extracted from wicking experiments were close to the contact angles on the flat CA and PMMA films. The surface of CA/PMMA fibers was very smooth with roughness measured in nanometers. Therefore, as expected the contact angle in the yarn is very close to that on flat surface of CA or PMMA. On the contrary, the surface morphology of microfibers formed from the polymer blends is drastically different from that of the films: the films were rough while the microfibers were smooth. This resulted in distinct wetting properties of yarns and films made of the same materials.

5.1 Introduction

Recently, nanofibers have attracted great attention as promising materials for building different constructs and nanodevices [1-3]. Nanofibers can be made porous or hollow and can be bundled and twisted into yarns [1-4]. Because of their flexibility and porosity, nanofiber yarns and webs show great potential for probing and scanning tissues. The wettability of electrospun yarns is the essential requirement for the fiber-based probes [5]. The material wettability depends on the surface energy of the material, which is evaluated by analyzing the contact angle using different probe liquids [6-9]. For a flat and smooth solid surface, the sessile drop technique is traditionally used to examine the contact angle. However, the determination of the contact angle on fibrous materials becomes a challenging task. The apparent contact angle significantly depends on the surface roughness [10, 11]. In addition, the liquid droplet may rapidly penetrate into the fiber structure making the sessile drop measurement questionable.

One straightforward method to overcome these problems is to use the capillary rise method. The contact angle can be obtained from the analysis of the wicking kinetics [12-16]. Owing to the complex fibrous structure of electrospun yarns, the contact angle of flat polymer films was first studied. The upward wicking of hexadecane and water into yarns was then analyzed. The Cahn surface tensiometer was employed for these studies. The water contact angle of CA/PMMA yarns was ~74° which was close to water contact angle on flat CA or PMMA films (~ 71 - 72°). In contrast, the surface morphology of the CA/PMMA films was very rough: one observed bumps and valleys. The water contact angle on CA/PMMA films was measured to be ~63°. However, the electrospun CA/PMMA fibers appeared smooth, no defects were noticed. The wicking experiments on yarns made of CA/PMMA fibers led to the conclusion that the contact angles of these fibers is very close to those measured on the films made from CA and PMMA.

5.2 Wettability of CA, PMMA, and CA/PMMA Films

5.2.1 Preparation of CA, PMMA, and CA/PMMA Films

The surface wettability is usually characterized by measuring the contact angle of a liquid on a solid surface. For a flat and smooth solid surface, the most common method is the sessile drop technique. The 10 wt% CA, 10 wt% PMMA, and 12.28 wt% CA/PMMA solutions were independently prepared for the CA, PMMA, and CA/PMMA films, respectively. The CA to PMMA ratio of CA/PMMA solution was prepared the same as the solutions prepared for the electropinning of CA/PMMA fibers. A 1,200 rpm speed was set on the spin coater (Headway Research Inc., MP-101) to make uniform films by rotating for 30 seconds. Glass slides (Corning Inc., 2947-3x1) were used as the coating substrates. The prepared films were dried overnight at room temperature in the hood and then dried at room temperature under vacuum (approximately 10 mmHg pressure) for 4 hours.

5.2.2 Contact Angles of CA, PMMA, and CA/PMMA Films

Hexadecane (HEX) and deionized water (Water) were chosen for the wettability experiments. HEX was chosen as a standard non-polar hydrocarbon solvent, and Water was chosen as the standard polar solvent. The measurements were done at room temperature using the sessile drop method: equilibration time was ~ 20 seconds. Results were recorded on the Contact Angle Measuring instrument (Krüss, FM40MK2 Easydrop) using the DSA software. Contact angles for each sample were measured at least five droplets, and the average values were reported. The contact angles of HEX on the CA and PMMA film surface were 0°, the droplets spread on the surface within 5 seconds. The contact angles of HEX on the CA/PMMA film surface were definitely less than 10° and we used 0° assuming complete wetting. The contact angles of each probe liquid are summarized in Table 5.1.

Table 5.1. Liquid properties and contact angles of liquids on CA, PMMA, and CA/PMMA films.

	Water	**HEX**
σ (mN/m)	71.4 ± 0.5	23.5 ± 0.2
η (cp)	1	3.03
Polymers	**Contact angles (°)**	
CA	71 ± 1.1	0
PMMA	72.2 ± 0.6	0
CA/PMMA	63.2 ± 0.6	0

It should be noted that the surface of CA/PMMA films is very rough and presented as a system of islands (Figure 5.1). Most likely the CA and PMMA phases separated during the spin coating and subsequent solvent evaporation [17-20]. The CA was the major component in the CA/PMMA film (*f* ~ 70%) and became the continuous phase during phase separation, and PMMA formed isolated islands surrounded by the CA polymer. Thus, the roughness and bump-and -valley structures lead to smaller contact angle; this result is in agreement with the Wenzel theory [21]. According to the Wenzel theory, water wets both bumps and valleys and hence the apparent contact angle decreases.

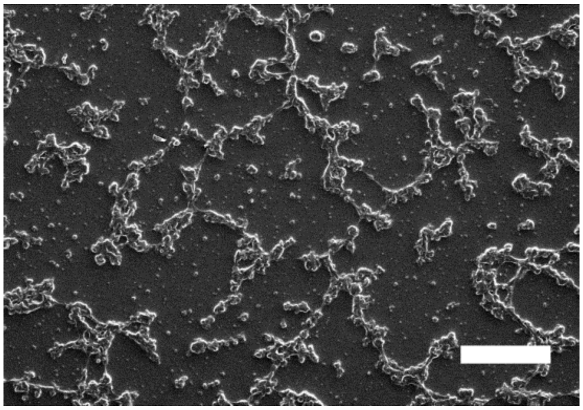

Figure 5.1. SEM micrographs of CA/PMMA films, scale bar is 200 μm.

The contact angles of different liquids on PMMA films were very close to those given in Ref. [9] which are ~ 72°. However, the contact angles of different liquids on CA films were higher than those given in Ref. [9], eg. $\theta_{\mathrm{Water}} = 54.5°$. The CA used in these experiments had a degree of substitution of ~2.3. Hence, the difference of the measured contact angle with that of Ref. [9] might be due to difference in the degree of substitution of their polymers.

5.3 Wettability of CA/PMMA Electrospun Yarns

One of the most popular methods of contact angle characterization of porous materials relies on the analysis of the wicking kinetics [22, 23]. The Lucas-Washburn equation, Eq. (4.4), reads:

$$L = \sqrt{\frac{2k_y P_c}{\varepsilon\eta} t}\,, \tag{5.1}$$

where ε is the yarn porosity, η is the liquid viscosity, k_y is the yarn permeability, and $P_c = 2\sigma\cos\theta / R_{eff}$ is the capillary pressure. R_{eff} is the effective pore radius in the yarn and σ is the liquid surface tension. The wicking constant (C_L), the slope of Eq. (5.1), is expressed as:

$$C_L = \sqrt{\frac{2k_y P_c}{\varepsilon\eta}} = \sqrt{\frac{4\sigma\cos\theta k_y}{\varepsilon\eta R_{eff}}}\,. \tag{5.2}$$

Thus, once the Lucas-Washburn wicking constant was determined, the capillary pressure P_c as well as the contact angle θ can be calculated from Eq. (5.2).

5.3.1 Experiments on Upward Yarn Wicking

In order to analyze the wicking kinetics of electrospun fiber yarns, the setup schematically shown in Figure 5.2 was employed. Again, the Cahn DCA-322 Dynamic Contact Angle Analyzer was used to record the weight change (*W*) as a function of time (*t*). The working principles of Cahn DCA-322 Analyzer have been discussed in detail in Chapter 4. In this chapter, we focus on the spontaneous wicking kinetics of yarns without embedding it in the capillary tube (compare with Figure 4.2a). A 20 mm long piece of an electrospun fiber yarn was cut with a razor blade, and the cut end was sealed with plasticine about 2 mm long and attached to a hook. Plasticine was used to connect the yarn to the hook and prevent wetting of the hook. The whole assembly, the hook with the plasticine sealed yarn, was attached to the hook of loop A of the Cahn DCA-322 Analyzer, and the other end of the yarn was set suspended above the free liquid surface. The stage with the liquid container moving up at the speed of 80 μm per second, the free end of the yarn was brought into contact with the liquid surface.

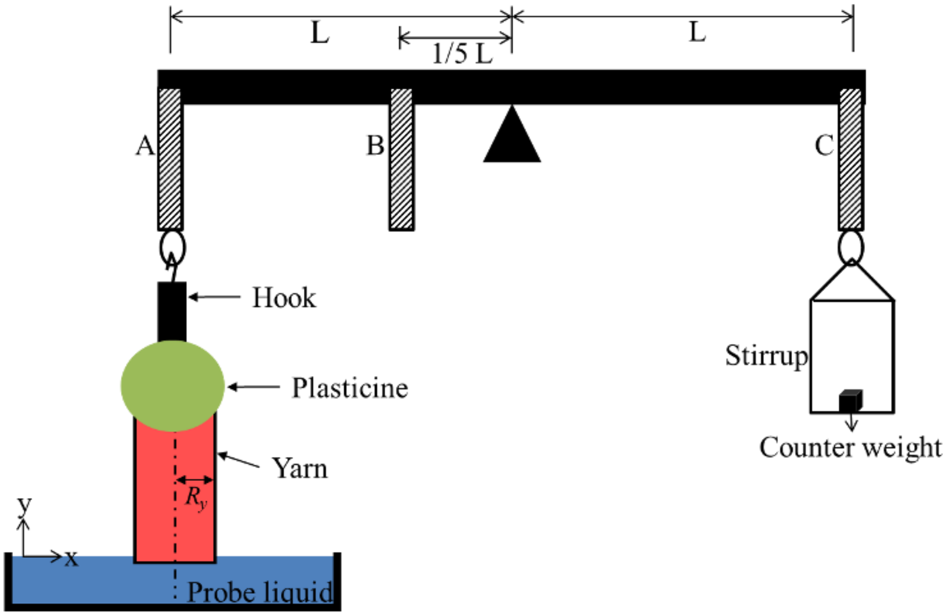

Figure 5.2. A schematic of the experimental setup showing the principle of operation of Cahn DCA-322 Analyzer. A hook with the plasticine sealed yarn is connected to the balance arm. The weight of the absorbed liquid is measured by the balance arm.

Here the Zero Depth of Immersion (ZDOI) was set at the level of F_{min} = 1 mgf. The balance was first zeroed, and the force was kept at the zero level when the stage was moved up (Figure 5.3). When the yarn touched the liquid surface, the force jumped up reflecting the action of the wetting force (red arrow in Figure 5.3) which appeared significantly larger than the ZDOI threshold [24]. When the yarn first touched the liquid surface, the stage was fixed and then the Cahn DCA-322 immediately started acquiring the force change over the next 5 minutes (red line in Figure 5.3). When the yarn just contacts the liquid surface, a wiggling behavior shown in the very beginning of red line was observed. This might be due to the formation of wetting meniscus and the observed vibration of the sample [24]. Therefore, it takes several seconds to stabilize the entire setup.

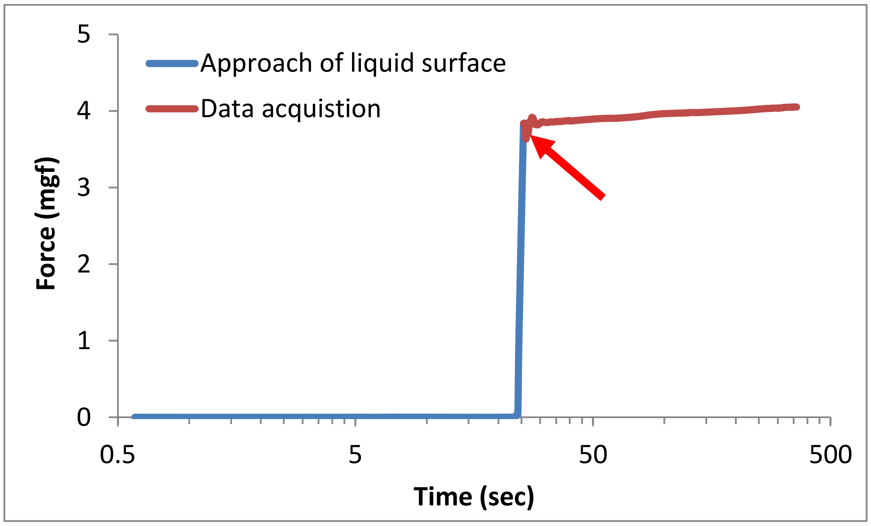

Figure 5.3. A typical experimental curve showing force changes at different steps: a steep jump of the blue line allows one to define the ZDOI point. The change of liquid weight was collected for 5 minutes (red line).

5.3.2 Analysis of Experimental Data

In the upward wicking, the driving force is the capillary pressure which is typically much greater than the hydrostatic pressure due to weight of the liquid column ρgL. For example, a water column should reach 15 meters for a 2 μm diameter pore (if $\theta = 0°$). In the prepared 2 cm long sample, the effect of gravity can be ignored, and the wicking kinetics are expected to follow the square-root-of-time behavior. The capillary pressure P_c can be obtained by examining the experimental data using Eq. (5.2).

The weight gain (ΔW) increasing with time t was converted to the meniscus position $L(t)$ as $L = \Delta W/\rho\varepsilon\pi R_y^2$, where ρ is the liquid density, ε is the yarn porosity, and R_y is the yarn radius. The Lucas-Washburn regime shows the linear dependence of L versus $t^{1/2}$ and can be observed as the black dashed line in Figure 5.4. The solution of Eq. (5.1) is modified to:

$$L - L_0 = C_L (t - t_0)^{1/2}, \tag{5.3}$$

where C_L is the wicking constant expressed by Eq. (5.2).

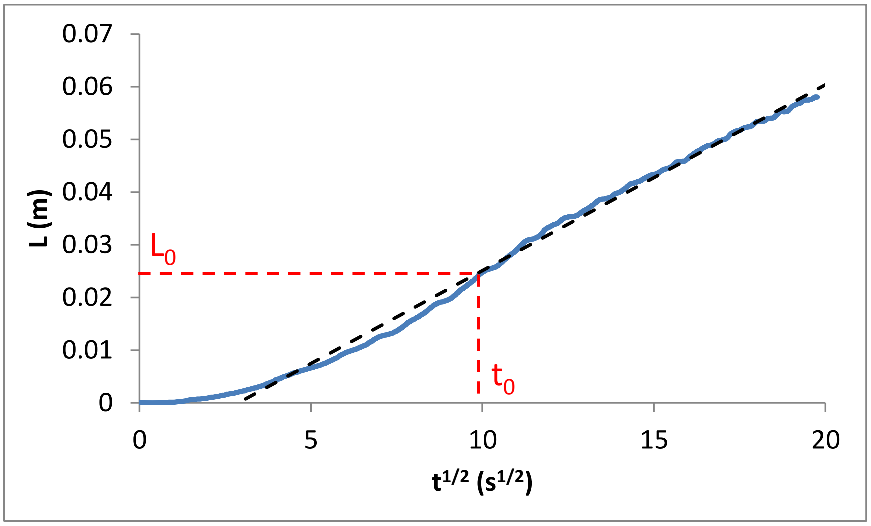

Figure 5.4. An experimental curve showing the wetting front position as a function of square-root-of-time. The black dashed line represents the fit which can be used for the description of the wicking kinetics when the time $t > t_0$.

The CA/PMMA yarns were prepared using the experimental protocol of yarn formation developed in Chapter 3, and the yarn permeability $k_y = 1.3 \times 10^{-13}$ m^2 and yarn porosity $\varepsilon = 0.33$ were obtained using the yarn-in-a-tube technique developed in Chapter 4. The hexadecane (HEX) and deionized water (Water) were selected as the probe liquids for the wicking experiments. Four samples were examined, and the average and standard deviation values were reported for each liquid. As one obtains the wicking constant (C_L), the capillary pressure can be determined from Eq. (5.2). For HEX, the slope was determined as $C_L = 3.2 \pm 0.4 \times 10^{-3}$ m/s$^{1/2}$ (Figure 5.5). Substituting the yarn permeability k_y, yarn porosity ε, surface tension σ (Table 5.1), and viscosity $\eta = 3.03$ cp of HEX into Eq. (5.2), we estimated the capillary pressure as $P_c \sim 3.7 \pm 0.8 \times 10^4$ Pa. The contact angle of HEX is assumed zero as shown by the film experiments. The capillary pressure P_c is related to the effective pore radius R_{eff} by the Laplace law of capillarity $P_c = 2\sigma/R_{eff}$. We found the effective pore radius as $R_{eff} \sim 1.3 \pm 0.3$ µm.

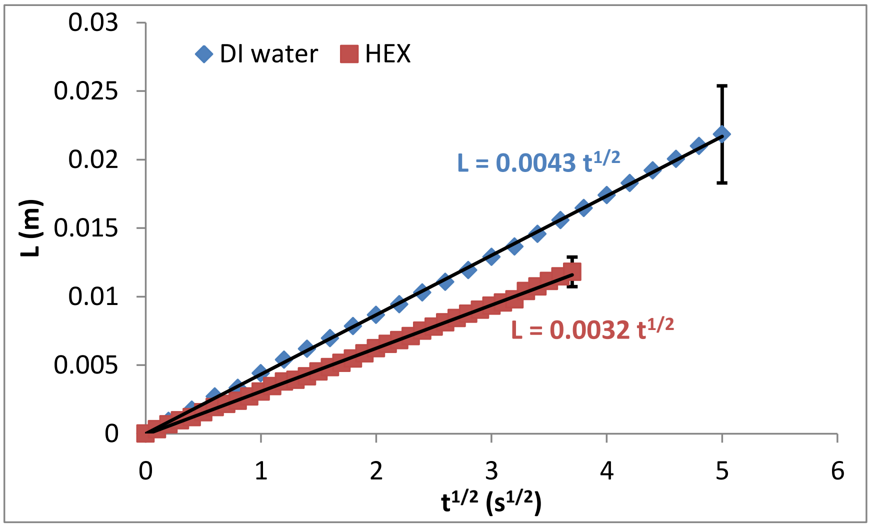

Figure 5.5. The wetting front position as a function of square-root-of-time for hexadecane and DI water. The black lines correspond to the Lucas-Washburn prediction.

Once again, one can determine the capillary pressure when Water was used as the probe liquid. The capillary pressure was found as $P_c = 2\sigma cos\theta/R_{eff} = 2.9 \pm 0.4 \times 10^4$ Pa. Because of high surface tension of DI water (Table 5.1), the contact angle cannot be assumed 0°. The effective pore radius R_{eff} ~1.3 µm found from the HEX wicking experiments was used for determination of the water contact angle. The water contact angle was obtained as ~ 74.3 ± 2.5°.

5.3.3 The Pore Size of the CA/PMMA Yarns

If the porous material is made of cylindrical tubes, one can consider that the liquid velocity of porous material is equal to the mean velocity of cylindrical tubes. As described in Chapter 2, the scaling arguments show that $k_y = R_p^2/8$, where R_p is the pore radius. This model of porous materials suggests that the yarn permeability is proportional to the square of pore opening R_p. The radius R_p was found as $R_p = (8k_y)^{1/2} = (8\times1.3\times10^{-13})^{1/2} \sim 1$ μm, which is close to $R_{eff} \sim 1.3$ μm determined by wicking experiments. Thus, this analysis allows one to assume that the transport pores and capillary pressure pores are the same. For this pore radius, the Jurin height Z_c of HEX will be ~ 5 m, which is much larger than the prepared yarn length, 2 cm, and the initial assumption of negligible gravity is valid for the capillary rise experiments.

5.3.4 Discussions

The contact angles extracted from wicking experiments on CA and PMMA yarns (~74°) were close to the contact angles measured on flat CA and PMMA films (~71-72°). The surface morphology of the CA/PMMA yarns was examined using a scanning electron microscope. As shown in Figure 5.6, the surface of CA/PMMA fibers was very smooth with roughness measured in nanometers. Therefore, as expected the contact angle in the yarn is very close to that on flat surface of CA or PMMA.

Comparing Figure 5.1 and Figure 5.6, the surface morphology of microfiber in the yarns is extremely different from that of the films. This leads to distinct wetting properties of yarns and films made of same CA/PMMA blends.

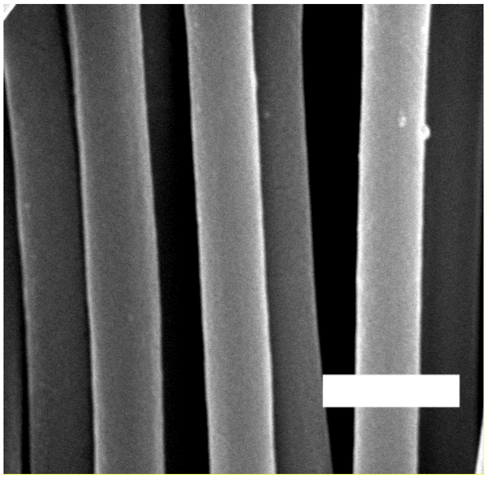

Figure 5.6. SEM micrographs of CA/PMMA yarns, scale bar is 1 μm.

5.4 Conclusions

In order to study the wetting properties of CA/PMMA electrospun yarns, flat films were prepared and used to estimate the surface compositions of the CA/PMMA fibers. On flat CA films, the water droplet makes a ~ 71° contact angle; on flat PMMA films, the water droplet makes a ~ 72° contact angle. Based on the analysis of surface morphology, the CA/PMMA films were nonuniform making the water contact angles lower.

The effective pore radius and water contact angle of CA/PMMA yarns were extracted from capillary rise method by HEX and DI water. The effective pore radius R_{eff} ~1.3 μm was close to the interfiber pore radius ~1 μm examined by the permeability. These results suggest that the transport pores and capillary pressure pores are the same for the CA/PMMA yarns. The water contact angle was ~74° which was close to the water contact angle on CA or PMMA films. On the contrary, the bump-and-valley structure of the CA/PMMA films results in improved wetting as suggested by the Wenzel theory.

Thus, the different surface morphology leads to distinct wetting properties of yarns and films made of CA/PMMA blends.

5.5 Methods

5.5.1 SEM Characterization

The surface morphology of the CA/PMMA fibers and films were examined with a Hitachi Field Emission scanning electron microscope (FESEM-Hitachi 4800). The samples were sputter-coated with a few nanometer thickness of gold prior to SEM examination.

5.5.2 Volume Ratio of Each Component on the Fiber (f)

Assuming that the solvent was totally evaporated and only solid polymers left in the fiber, the volume ratio of each component (f_i) can be calculated as:

$$f_i = \frac{m_i/\rho_i}{\sum(m_i/\rho_i)} \tag{5.4}$$

where m_i is the mass of each component in the fiber and ρ_i is the density of each component in the fiber. Giving the experimental compositions of CA/PMMA solution, the volume ratio of CA on the fiber is $f_1 \sim 0.7$.

5.5.3 Measurements of Surface Tension (σ)

The surface tension of hexadecane and deionized water was measured using the Wilhelmy method with a Cahn DCA-322 [25]. A platinum wire with a 250 μm diameter was used as the standard probe [24]. The wire was cleaned with ethanol and heated to red-hot with an oxidizing flame. The Wilhelmy equation $F=\sigma P\cos\theta$ was used, where F is the wetting force, σ is the surface tension of the probe liquid, P is the perimeter of the probe, and θ is the contact angle. We assumed that the contact angle is $\theta = 0°$ or $\cos\theta = 1$ because of the high surface energy of the platinum. Hexadecane and deionized water were measured three times, yielding an average surface tension of $\sigma_{HEX} = 23.5 \pm 0.2$ mN/m and $\sigma_{Water} = 71.4 \pm 0.5$ mN/m, respectively.

5.6 References

1. Reneker, D.H. and A.L. Yarin, *Electrospinning jets and polymer nanofibers.* Polymer, 2008. **49**(10): p. 2387-2425.

2. Rutledge, G.C. and S.V. Fridrikh, *Formation of fibers by electrospinning.* Advanced Drug Delivery Reviews, 2007. **59**(14): p. 1384-1391.

3. Dzenis, Y., *Structural Nanocomposites.* Science, 2008. **319**(5862): p. 419-420.

4. Ramakrishna, S. and W.E. Teo, *A review on electrospinning design and nanofibre assemblies.* Nanotechnology, 2006. **17**(14): p. R89-R106.

5. Tsai, C.C., P. Mikes, T. Andrukh, E. White, D. Monaenkova, O. Burtovyy, R. Burtovyy, B. Rubin, D. Lukas, I. Luzinov, J.R. Owens, and K.G. Kornev, *Nanoporous artificial proboscis for probing minute amount of liquids.* Nanoscale, 2011. **3**(11): p. 4685-4695.

6. Wu, S., *Calculation of interfacial tension in polymer systems.* Journal of Polymer Science Part C: Polymer Symposia, 1971. **34**(1): p. 19-30.

7. Fowkes, F.M., *Attractive forces at interfaces.* Industrial & Engineering Chemistry, 1964. **56**(12): p. 40-52.

8. Owens, D.K. and R.C. Wendt, *Estimation of the surface free energy of polymers.* Journal of Applied Polymer Science, 1969. **13**(8): p. 1741-1747.

9. Van Oss, C.J., *Interfacial Forces in Aqueous Media*. 1994: Marcel Dekker.

10. Cassie, A.B.D. and S. Baxter, *Wettability of porous surfaces.* Transactions of the Faraday Society, 1944. **40**: p. 546-551.

11. Baxter, S. and A.B.D. Cassie, *8—The water repellency of fabrics and a new water repellency test.* Journal of the Textile Institute Transactions, 1945. **36**(4): p. T67-T90.

12. Kissa, E., *Wetting and Wicking.* Textile Research Journal, 1996. **66**(10): p. 660-668.

13. Perwuelz, A., P. Mondon, and C. Caze, *Experimental Study of Capillary Flow in Yarns.* Textile Research Journal, 2000. **70**(4): p. 333-339.

14. Brugnara, M., E. Degasperi, C. Della Volpe, D. Maniglio, A. Penati, and S. Siboni, *Wettability of porous materials. II. Can we obtain the contact angle from the Washburn equation.* Contact Angle, Wettability and Adhesion, 2006. **4**(143-164): p. 192.

15. Callegari, G., I. Tyomkin, K.G. Kornev, A.V. Neimark, and Y.L. Hsieh, *Absorption and transport properties of ultra-fine cellulose webs.* Journal of Colloid and Interface Science, 2011. **353**(1): p. 290-293.

16. Nyoni, A.B. and D. Brook, *Wicking mechanisms in yarns-the key to fabric wicking performance.* Journal of the Textile Institute, 2006. **97**(2): p. 119-128.

17. Lee, W.H., D. Kwak, J.E. Anthony, H.S. Lee, H.H. Choi, D.H. Kim, S.G. Lee, and K. Cho, *The Influence of the Solvent Evaporation Rate on the Phase Separation and Electrical Performances of Soluble Acene-Polymer Blend Semiconductors.* Advanced Functional Materials, 2012. **22**(2): p. 267-281.

18. Heriot, S.Y. and R.A.L. Jones, *An interfacial instability in a transient wetting layer leads to lateral phase separation in thin spin-cast polymer-blend films.* Nature Materials, 2005. **4**(10): p. 782-786.

19. DalnokiVeress, K., J.A. Forrest, J.R. Stevens, and J.R. Dutcher, *Phase separation morphology of spin-coated polymer blend thin films.* Physica A, 1997. **239**(1-3): p. 87-94.

20. Liu, T., R. Ozisik, and R.W. Siegel, *Phase separation and surface morphology of spin-coated films of polyetherimide/polycaprolactone immiscible polymer blends.* Thin Solid Films, 2007. **515**(5): p. 2965-2973.

21. Wenzel, R.N., *Surface Roughness and Contact Angle.* The Journal of Physical and Colloid Chemistry, 1949. **53**(9): p. 1466-1467.

22. Lucas, R., *Ueber das Zeitgesetz des kapillaren Aufstiegs von Flussigkeiten.* Kolloid Zeitschrift, 1918. **23**: p. 15-22.

23. Washburn, E., *The Dynamics of Capillary Flow.* Phys. Rev. Physical Review, 1921. **17**(3): p. 273-283.

24. Miller, B., L.S. Penn, and S. Hedvat, *Wetting force measurements on single fibers.* Colloids and Surfaces, 1983. **6**(1): p. 49-61.

25. Adamson, A.W. and A.P. Gast, *Physical chemistry of surfaces*. 1997, New York: Wiley.

CHAPTER SIX

NANOPOROUS ARTIFICIAL PROBOSCIS FOR PROBING MINUTE AMOUNT OF LIQUIDS

The challenge of making probes with fast absorption rates was addressed theoretically and experimentally. This work shows that the probe should possess two levels of pore hierarchy: nanopores are needed to enhance the capillary action and micrometer pores are required to speed up fluid transport. The model of controlled fluid absorption was verified in experiments. The artificial proboscises can be remotely controlled by electric or magnetic fields were demonstrated. Using an artificial proboscis, one can approach a drop of hazardous liquid, absorb it and safely deliver it to an analytical device. With these materials, the paradigm of a stationary microfluidic platform can be shifted to the flexible structures that would allow one to pack multiple microfluidic sensors into a single fiber.

6.1 Introduction

Many butterflies, moths, and other insects easily probe and identify potable liquids with their proboscises. The ability to manipulate the proboscis, which can be coiled and uncoiled like a party noisemaker, is closely linked to its remarkable fluid transport capabilities. In addition, the proboscis can be flawlessly positioned in a targeted liquid drop. As shown in Figure 6.1A, a butterfly can position proboscis in a spot with sugar solution and can effectively withdraw sugar solution from the pores of paper towel.

Insect proboscises feature integrated sensors and filters that distinguish foods and chemicals. Integrating all these features—ability to deploy, sense and sample, and identify low-volume fluids—into a single micro–nanofluidic device is attractive and promising for many engineering applications. Therefore, it becomes a challenging and rewarding task to fabricate an artificial, biomimetic proboscis that possesses many properties of its natural cousin.

As recently shown in Ref. [1, 2], the butterfly proboscis has a two-level pore hierarchy. The proboscis is nanoporous in its lateral dimension, which comprise the first level of pore hierarchy. These nanopores are created by overlapping legulae. The legulae are formed like a fence on two tubular musculature structures—galeas, Figure 6.1B. Galea tubes have lateral indentations, so that when galeas are locked by legulae, these two indentations form the food canal. The food canal, whose diameter ranges from a few to tens of micrometers, forms the second level of pore hierarchy.

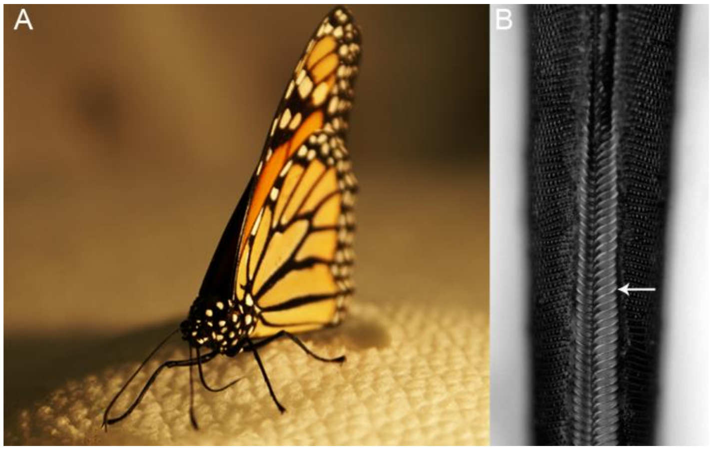

Figure 6.1. (A) Butterfly drawing sugar solution from paper towel. The dorsal side of the proboscis is pushed toward the porous surface, (B) The legulae (arrow), looking like a fence at the dorsal side of the proboscis. The liquid wicks into the food canal through the nanopores formed by two nearest legulae.

In this chapter, a method of fabrication of nanoporous flexible probes which work as artificial proboscises is described. The challenge of making probes with fast absorption rates and good retention capacity was addressed theoretically and experimentally. The probe material requires at least a double porosity with nanometer pores that provide strong capillary action, and micrometer pores that provide rapid wicking. The model of controlled fluid absorption was verified in experiments. Materials and design strategies were focused on making artificial proboscises that feature an unprecedented flexibility, deployability, and absorptive capacity.

Recently, electrospun nanofibers have gained considerable attention as building blocks for various constructs and nanodevices [3-7]. Nanofibers can be made porous and hollow, and can be bundled and twisted into yarns. These materials constitute a broad class of flexible, lightweight structures that can be utilized in many applications dealing with liquid handling and manipulation [8-11]. Precision control of these properties, however, is critical for performance of the probe design. As an illustration of robustness of the proposed method, an artificial proboscis was made from polyvinylidene fluoride (PVDF) fibers. PVDF is well-known for its chemical inertness and thermal stability due to the presence of -CF_2- groups [4, 6]. Another advantageous PVDF property is that the $C_2H_2F_2$ molecular units of the polymer chains possess large dipole moments. These dipoles point from the electronegative fluorine to the electropositive hydrogen. Under certain solidification conditions, the dipoles form ordered structures that make the material ferroelectric [12-20]. Hence, the produced probes can be manipulated with electric fields to grab and absorb droplets of hazardous liquids. The PVDF fibers can be made porous by adding a removable polymer to the dope prior to electrospinning. The probes made of these nanoporous fibers do exhibit an increased rate of liquid absorption.

The artificial proboscises can be remotely controlled with electric or magnetic fields. Using an artificial proboscis, one can approach a drop of hazardous liquid, absorb it and safely deliver it to an analytical device. With these materials, the paradigm of a stationary microfluidic platform can be shifted to the flexible structures that would allow one to pack multiple microfluidic sensors into a single fiber.

Artificial proboscises made of nanofibers with the proposed pore structure will find many applications as active elements in nanofluidic devices, chemical and biomedical sensors, forensic probes, and in many other fields where probing minute amounts of liquids is a crucial step of material processing and analysis.

6.2 Fabrication of Artificial Proboscis

The proposed yarn formation protocol developed in Chapter 3 was used to fabricate yarns from PVDF/PEO blends. The electrospinning parameters, such as flow rate, applied voltage, and gap between the needle and collector, are given in Table 3.1.

The morphological structure of the PVDF/PEO nanofiber surfaces and yarns was examined with a Field Emission Scanning Electron Microscope (FESEM, Hitachi 4800) and shown in Figure 6.2. The solid nonporous fibers and porous fibers were fabricated during winter and summer, respectively. The temperature and relative humidity (RH) in the hood were measured using a hygrometer (Fisher Scientific, S/N: 80614641). It was observed that the RH was 50-65 % during summer while the RH was 25-35 % during winter, but the ambient temperature was not significantly changed ~23-25 °C. The electrospinning parameters were all maintained at the same conditions except humidity. Hence, the resulting fibers were solid when produced at 25-35% RH. In contrast, nanoporous fibers could be produced at 50~65 RH% without the additional step of PEO removal. The diameters of porous fiber range between 0.8 and 1.8 µm, giving an average diameter of ~1.2 µm.

The probable reason is that the solvent, DMAC, had absorbed some water. Hence, since the solvent evaporated during electrospinning process, water that was held mostly by PEO was evaporated and the porous structure formed. Therefore, humidity is a significant factor for the production of PVDF/PEO nanoporous fibers.

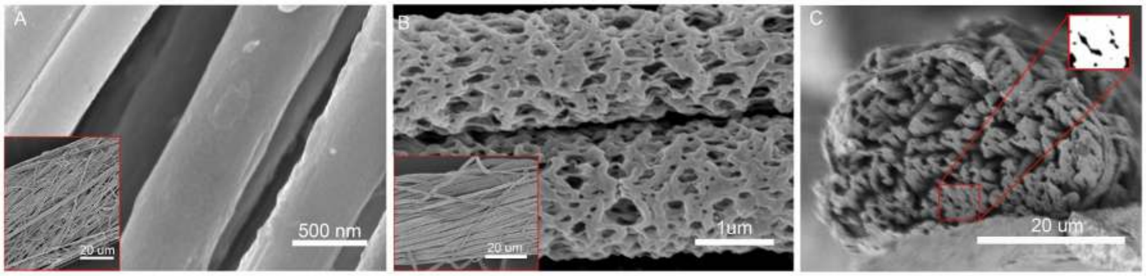

Figure 6.2. SEM images of the electrospun PVDF/PEO fibers. (A) Solid non-porous fibers, (B) Porous fibers, (C) The cross-section of PVDF/PEO yarns. The black areas in the insert show the pores in an undisturbed spot after the yarn cutting. This area suggests that the porosity is close to 10%.

6.3 Experimental

6.3.1 Fiber Porosity[4]

To determine the fiber porosity, a micropiece of as-spun fiber was cut using the tip of the AFM (Dimension 3100 AFM, Veeco Inc). Then, this piece was glued to the

---

[4] I acknowledge Dr. Ruslan Burtovyy for the help in the measurements of fiber porosity.

AFM tip for further analysis. The idea of porosity measurements using AFM is that the resonance frequency of the AFM cantilever is very sensitive to minute changes in mass. If one manages to fill all pores in the attached fiber with certain liquid of a known density, the resonance frequency should depend on the mass of absorbed liquid, i.e. on its volume (see Methods 6.7.2). Hence the porosity, which is the ratio of the pore volume to the fiber volume, can be estimated directly.

Assuming that all pores are filled completely with the liquid, the fiber porosity is estimated as:

$$\varepsilon_{\mathrm{f}} = \frac{V_{\mathrm{liquid}}}{V_{\mathrm{liquid}} + V_{\mathrm{matrix}}} = \frac{1}{1 + V_{\mathrm{matrix}} / V_{\mathrm{liquid}}} = \frac{1}{1 + V_{\mathrm{matrix}} \rho_{\mathrm{liquid}} / M_{\mathrm{liquid}}}, \tag{6.1}$$

where V_{liquid} is the volume of absorbed liquid which is equal to the volume of open pores and V_{matrix} is the volume of polymer matrix calculated through the fiber mass, mass fractions (M) of the used polymers, and their densities (ρ) as:

$$\begin{aligned} V_{\mathrm{matrix}} &= V_{\mathrm{PEO}} + V_{\mathrm{PVDF}} \\ &= \frac{M_{\mathrm{PEO}}}{M_{\mathrm{PEO}} + M_{\mathrm{PVDF}}} \frac{M_{\mathrm{fiber}}}{\rho_{\mathrm{PEO}}} + \frac{M_{\mathrm{PVDF}}}{M_{\mathrm{PEO}} + M_{\mathrm{PVDF}}} \frac{M_{\mathrm{fiber}}}{\rho_{\mathrm{PVDF}}} . \end{aligned} \tag{6.2}$$

To ensure complete filling of nanopores in the fiber, we chose Galwick (Porous Materials, Inc) as the filler. Galwick has very low surface tension ($\sigma = 16$ mN/m) and it wets PVDF and PEO surfaces completely. Using AFM, the tip with attached fiber was immersed into a Galwick drop. Then, the new value of the resonance frequency was measured. Since the elastic constant of this complex spring is maintained, the change of the resonance frequency is mostly controlled by the added mass. M_{Galwick} and M_{fiber} were measured. Substituting in Eqs. (6.1) and (6.2) the measured ratio $M_{\mathrm{galwick}}/M_{\mathrm{fiber}} = 5.12$, and the given values $M_{\text{PEO}}/M_{\text{PVDF}}$ = 0.1, ρ_{Galwick} = 1.82 g/cm^3, ρ_{PVDF} = 1.76 g/cm^3, ρ_{PEO}=1.13 g/cm^3, we estimated the porosity of single fibers as ε_f = 0.82. This high porosity suggests that even a single fiber appears to be a good candidate for design of nanoprobes enabling one to collect and retain liquids in pores. When the fibers are twisted in the yarn, thus forming large micropores between them, one expects that the transport properties of yarns will be significantly enhanced.

6.3.2 Absorbency of Artificial Proboscises

Porous and nonporous PVDF/PEO fiber yarns were prepared using the experimental protocol of yarn formation developed in Chapter 3. In a first series of experiments, the wicking properties of the produced yarns were studied. Droplets of wetting nonvolatile liquids, hexadecane (HEX) and tributyl phosphate (TBP), Table 6.1, were used for the evaluation of wicking properties of the yarns. These liquids were chosen as simulants of hazardous liquids [21-27]. Droplets with initial volume V_0 were deposited on yarns, as shown in Figure 6.3b. The drop volume $V(t)$ was defined at each increment of time t by fitting the drop profile with Carrol's unduloid[5] [28, 29], an analytical solution of the Laplace equation of capillarity that describes the drop shape as a function of its volume. Figure 6.3b shows a sequence of pictures of a HEX droplet during its absorption by the yarn. To confirm that the droplet does not evaporate during absorption experiment, but gets absorbed by the yarn, a reference HEX droplet was

---

[5] I acknowledge Yu Gu and Dr. Monaenkova for their help in the development of Matlab® codes for the droplet volume analysis.

placed on a copper wire. As clearly seen from Figure 6.3b, this reference droplet does not visibly change its volume, thus, proving that the yarn does take the drop in.

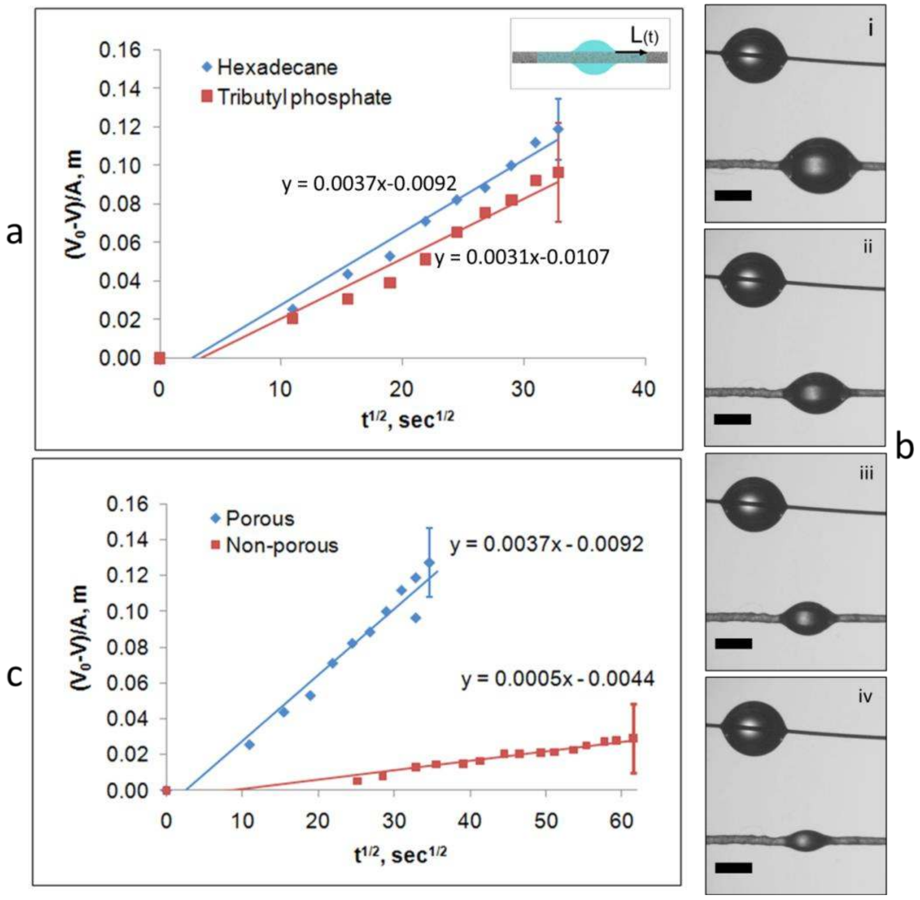

Figure 6.3. (a) Comparative absorption kinetics of hexadecane and TBP droplets on yarns made of porous PVDF/PEO fibers. *A* is the yarn cross-section, V_0 is the initial drop volume, and *V* is the drop volume at time *t*. The insert is the schematic used for modeling of drop penetration into yarn. The front position is shown by the black arrow. (b) A series of pictures illustrating the absorption kinetics of hexadecane droplet into the PVDF/PEO yarn made of nanoporous fibers. An 80-μm copper wire with a hexadecane droplet of the same initial volume was used as the reference. Scale bar: 500μm. (c) Comparative absorption kinetics of hexadecane droplets by yarns made of porous and non-porous fibers. The error bar corresponds to the highest standard deviation in the experiments.

The change of the droplet volume (V_0-$V(t)$) as a function of time was filmed and analyzed. Figure 6.3a shows the results of these absorption experiments conducted on four porous yarns. The absorption kinetics for both tested liquids followed the square-root-of-time law, also known as the Lucas–Washburn law [30, 31]. The slope of the fitting lines in Figure 6.3a, or wicking constants are close to each other (HEX: 0.0037 $m/s^{1/2}$; TBP: 0.0031 $m/s^{1/2}$). The results suggest that the yarn properties are very repeatable from one sample to another and that the given similarity is not just a chance event, but an expected consequence of the similarity of liquid properties, Table 6.1.

Table 6.1. Properties of probed liquids.

Property at (20°C-25°C)	Tributyl phosphate (TBP)	n-Hexadecane (HEX)
Color	Colorless	Colorless
Molecular formula	$C_{12}H_{27}O_4P$	$C_{16}H_{34}$
(Molecular Weight)	(Mw: 266.31)	(Mw: 226.24)
Viscosity (mPa·s)	3.80	3.03
Surface tension (mN/m)	27 ± 0.1	23.5 ± 0.2
Density (g/cm^3)	0.97	0.773
Vapor Pressure (mm Hg)	27 @ 178 °C	1 @ 105^{0}C

In a second series of experiments, with three porous and three non-porous yarns, the absorption properties of yarns made of solid non-porous fibers are much different from those of porous fibers were presented. As demonstrated in Figure 6.3c, the wicking constant of yarns made of solid nonporous fibers (0.0005 $m/s^{1/2}$) is at least 7 times smaller than that of porous fibers (0.0037 $m/s^{1/2}$), It is, therefore, important to understand the mechanism of significant enhancement of the wicking properties provided by the nanoporous fibers in the yarn.

6.4 Kinetics of Drop Absorption into Yarns with Double Porosity

When the dimensions of pores in a material are measured in nanometers, the rate of wicking becomes very slow [11, 32-35]. Therefore, it is a challenge to speed up fluid transport in these materials. Integration of nanoporous fibers into yarns provides a new degree of freedom in the probe design. Yarns may have two types of pores: nanometer pores in the fibers and micrometer pores between the fibers. Therewith, the absorption kinetics is expected to be distinguishable from that observed in materials having a unimodal pore size distribution [36].

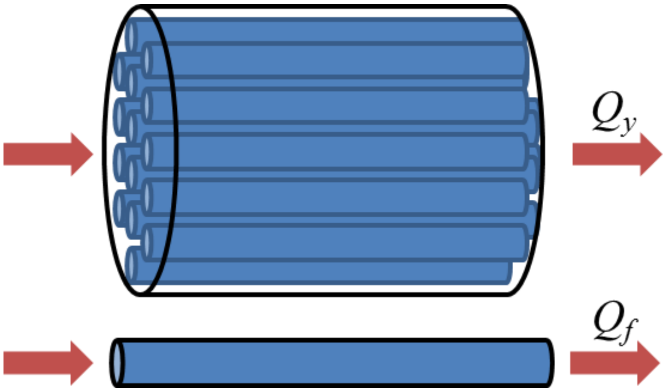

Figure 6.4. A schematic illustrates that the liquid flow through a yarn and a porous fiber. Subscripts *y* and *f* correspond to yarn and fiber, respectively.

Figure 6.4 illustrates the liquid flow through a yarn and a porous fiber respectively. If the yarn cross-sectional area is *A*, the velocity of the wetting front at time *t* is *v*(*t*), then the flow discharge through the interfiber pores is calculated as:

$$Q_y = \varepsilon_y A v(t), \tag{6.3}$$

where ε_y is the yarn porosity.

The total cross-sectional area of the fibers in the yarn is obtained as $A_f = (1-\varepsilon_y)A$. Accordingly, the flow discharge through the porous fibers reads:

$$Q_f = \varepsilon_f A_f v(t) = \varepsilon_f (1-\varepsilon_y) A v(t), \tag{6.4}$$

where ε_f is the fiber porosity.

Applying Darcy's law, the yarn permeability k_y corresponds to the permeability of yarn made of nonporous fibers:

$$Q_y = -\frac{k_y A}{\eta}\frac{\partial P}{\partial x}, \tag{6.5}$$

where η is the liquid viscosity and $\partial P/\partial x$ is the pressure gradient assuming the x-axis along the fiber.

The discharge only through the fibers is written as:

$$Q_f = -\frac{k_f A_f}{\eta}\left(\frac{\partial P}{\partial x}\right), \tag{6.6}$$

where k_f is the permeability of a single porous fiber.

Hence, the mass balance $Q_y + Q_f$ is expressed as:

$$[\varepsilon_y + \varepsilon_f(1-\varepsilon_y)]Av(t) = -[k_y + k_f(1-\varepsilon_y)]\frac{A}{\eta}\frac{\partial P}{\partial x}. \tag{6.7}$$

The liquid is assumed not volatile (eg. Hexadecane, vapor pressure: 1 mmHg @ 105°C), hence, the mass conservation equation reads $\partial(Q_y+Q_f)/\partial x = \partial^2 P/\partial x^2 = 0$. Integrating this equation, one obtains the linear distribution of the potential along the liquid column, $P(x) = ax + b$, where a and b are time-dependent functions that can be found from the boundary conditions. For further analysis it is sufficient to consider only one half of the drop and place the center of coordinate at the contact line. Hence, taking atmospheric pressure for the reference, the first boundary condition reads $P(0) = 0$. The second boundary condition is formulated at the wetting front $x = L(t)$. There, the capillary pressure is built by the pores between fibers, $P(L) = -P_c$. These two boundary conditions specify the pressure gradient $\partial P/\partial x = -P_c/L(t)$. Substituting this pressure gradient and noticing that at the wetting front $v(t) = dL/dt$ into Eq. (6.7), one can obtain an ordinary differential equation:

$$\frac{dL}{dt} = \frac{[k_y + k_f(1-\varepsilon_y)]}{[\varepsilon_y + \varepsilon_f(1-\varepsilon_y)]}\frac{P_c}{\eta L}. \tag{6.8}$$

Integrating Eq. (6.8) once to give:

$$L = \sqrt{\frac{2P_c}{\eta}\frac{[k_y + k_f(1-\varepsilon_y)]}{[\varepsilon_y + \varepsilon_f(1-\varepsilon_y)]}t}. \tag{6.9}$$

The front position $L(t)$ can be expressed through the incremental change of droplet volume as: $(V(t) - V_0)/A = 2[\varepsilon_y + \varepsilon_f(1 - \varepsilon_y)]L(t)$, where the factor two accounts for two wetting fronts. Solving this equation for L(t) and substituting it to Eq. (6.9), we obtain:

$$\frac{V_0 - V_t}{A} = C_w t^{1/2}, \tag{6.10}$$

where C_w is the slop or wicking constant which is expressed as $C_w = 2\sqrt{2k_{eff}P_c/\eta}$ and $k_{eff} = [k_y + k_f(1-\varepsilon_y)][\varepsilon_y + \varepsilon_f(1-\varepsilon_y)]$.

6.5 Mechanism of Strong Wicking

Nanoporous materials are superior absorbers due to their ability to generate extremely high capillary pressure [37]. The suction capillary pressure of a porous material is estimated by the Laplace formula as $P_c \sim 2\sigma\cos\theta/R_p$, where σ is the liquid surface tension, θ is the contact angle, and R_p is a characteristic radius of pores in the material [37, 38]. Hence, by decreasing the pore radius down to nanometers, one can significantly increase the driving force for the liquid wicking. On the other hand, doing so, one makes nanoporous materials even less permeable. Therefore, it is instructive to analyze a condition in which the interfiber spacing would provide sufficient permeability to the yarn, yet nanoporous fibers would increase the driving force for wicking.

Eq. (6.10) is a familiar definition of the Lucas–Washburn wicking constant C_w with the effective permeability k_{eff}. Capillary pressure P_c and effective permeability k_{eff} include all effects caused by nanopores in the fibers. As known from the physics of flow through porous media, the permeability is proportional to the square of the pore radius [38]. Therefore, the yarn permeability is typically much greater than the fiber permeability, $k_y >> k_f$. In this limit, the wicking constant is represented in a form convenient for comparison with the experiment:

$$C_w = 2\sqrt{\frac{2P_c k_y}{\eta}[\varepsilon_y + \varepsilon_f(1-\varepsilon_y)]}\,. \tag{6.11}$$

Porous fibers increase the capillary pressure, $P_c \propto 1/R_p$ but decrease the permeability, $k_f \propto R_p^2$. As follows from Eq. (6.11), when the porous fibers are twisted in a yarn, the permeability increases, yet the capillary pressure stays the same. As a result, the wicking constant increases; the smaller the pore size in each fiber, the greater is the wicking constant.

As seen from Figure 6.2C, where the porosity of a spot not affected by the yarn cutting was analyzed, the fibers in the yarn are closely packed. It is therefore plausible to assume that the fibers form a hexagonal elementary cell. Then the yarn porosity is estimated as $\varepsilon_y \approx (\sqrt{3}-\pi/2)/\sqrt{3} \approx 0.1$, and its permeability as $k_y \approx 0.008d^2$, where d is the fiber diameter [28, 29, 32]. Keeping the ratio d/R_p high, one can significantly increase the wicking constant $\propto d/\sqrt{R_p}$. These arguments explain the experimentally observed tendency.

To make a quantitative estimate of the characteristic pore diameter, $D_p = 2R_p$ that pulls the liquid in the yarn, Eq. (6.11) was solved for P_c using the measured wicking constants C_w and fiber porosities, $\varepsilon_f \approx 0.8$. Through these parameters, the capillary pressure is expressed as $P_c = C_w^2\eta/[8k_y(\varepsilon_y+\varepsilon_f(1-\varepsilon_y)]$. TBP and HEX wet the fibers, hence we can approximate the cosine of the contact angle by one, $cos\theta \approx 1$. Therefore, the effective diameter of the pores in the fiber is estimated as:

$$D_p \approx 4\sigma/P_c = 32\sigma k_y[\varepsilon_y+\varepsilon_f(1-\varepsilon_y)]/(C_w^2\eta). \tag{6.12}$$

In experiments, the fiber diameters in the yarn varied from 0.7 to 1.5 µm with the average d ~ 1 µm. For the yarns made of solid fibers, $\varepsilon_f = 0$, with the average fiber diameter $d = 1$ µm, Eq. (6.12) gives the diameter of effective pores as $D_p = 800$ nm. For yarns made of porous fibers, $\varepsilon_f \approx 0.8$, with the average fiber diameter $d = 1$ µm, Eq. (6.12) gives the diameter of effective pores as $D_p = 100$ nm. The smaller diameter fits the size of the pores in each fiber and the larger diameter appears to be on the same order of magnitude as that of an average interfiber gap.

To confirm these estimates, the ImageJ (NIH) was used to evaluate the pore size distribution from the SEM pictures of porous fibers (Figure 6.2B). Modeling the pore as a circular cylinder allowed calculating the pore diameter as $D_p = \sqrt{4A/\pi}$, where A is the visible cross-sectional area of the pore. Figure 6.5 shows that the average pore diameter is D_p ~ 97 nm, which is in agreement with the prediction of our theoretical model (~ 100 nm).

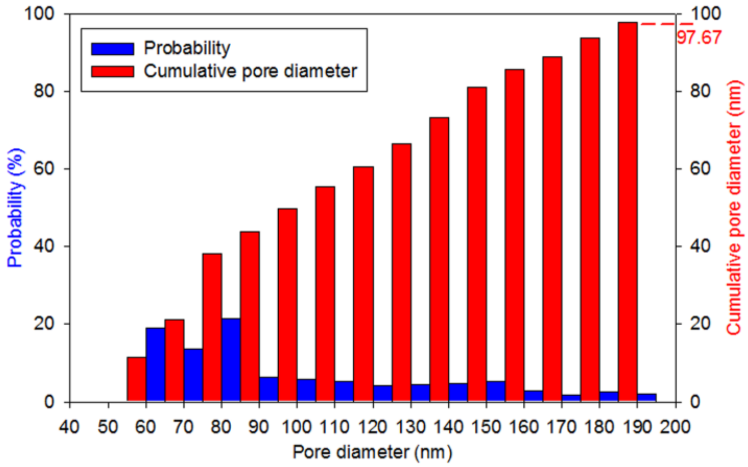

Figure 6.5. The pore size distribution of electrospun nanoporous PVDF/PEO fibers. The blue column shows the frequency of appearance of a fiber with a certain diameter. The numbers above the red columns show the cumulative pore diameter, which approaches the average pore diameter of 98 nm.

Thus, in our experiments, the hundred-nanometer pores provided the driving force for liquid wicking whereas micrometer-wide interfiber gaps facilitated the liquid movement through the yarns.

6.6 Deployment and Manipulation of the Artificial Proboscis with Electric and Magnetic Fields[6]

A butterfly uses a yet unknown mechanism to unroll and direct its proboscis toward a target [39]. For the deployment and positioning of the artificial proboscis the effect of the PVDF ferroelectricity was utilized. Hence the artificial proboscis can be flexed and controlled by applying an electric field. As shown in Figure 6.6, two copper

---

[6] I acknowledge Dr. T. Andruch for the experiments on manipulation of artificial proboscis.

plates were fixed vertically and parallel to each other, forming an 18 mm gap in between. One plate was connected to a power supply (Glassman FC series) and the other plate was grounded. The 320 μm diameter artificial proboscis was vertically suspended between the two electrodes. Its upper end was clamped to the holder and the lower end was free to move. A 0.34 μL TBP droplet was deposited onto the substrate at the bottom of the cell. This cell was enclosed with a transparent 60 mm × 30 mm × 18 mm box, thus preventing any perturbations of the artificial proboscis caused by air flow. After application of an 8 kV potential, proboscis bending and movement were observed. In this field, no appreciable change of the droplet shape was observed. This process was filmed with a video camera (Dalsa Falcon 1.4, Canada). When the artificial proboscis touched the droplet, the power was turned off. After that, the tip of the artificial proboscis was held attached to the droplet by only the surface tension of the liquid. Finally, when the droplet was completely wicked into the yarn, the yarn bent back to its initial straight shape. In contrast, the nylon yarn suspended in the cell as a reference stayed straight during the whole experiment (Figure 6.6). The nylon reference yarn had the same diameter and length as its experimental counterpart. This evidence favors the hypothesis that the PVDF/PEO fibers do contain a substantial amount of ferroelectric crystals. Thus, an artificial proboscis so constructed can be used for grabbing and probing hazardous liquids. Furthermore, it appears straightforward to embed superparamagnetic nanoparticles (FERRO 2Oz, CMS Magnetics) into porous fibers, thus making the proboscis reactive to a magnetic field [40-42]. An example of such a proboscis is shown in Figure 6.7.

Magnetically actuated artificial proboscises are attractive candidates for probing aqueous solutions, blood or any biofluids that do not interfere with the magnetic field.

Figure 6.6. (A) Butterfly with a proboscis searching for food. (B) A schematic of yarn manipulation with electric field generated by two vertical electrodes. (C) Artificial proboscis made of PVDF/PEO fibers absorbing a TBP droplet. Two electrodes are positioned from the sides and are not shown here. The solid black fiber on the left is the artificial proboscis; the gray fiber on the right is a nylon yarn. The scale bar is 2 mm.

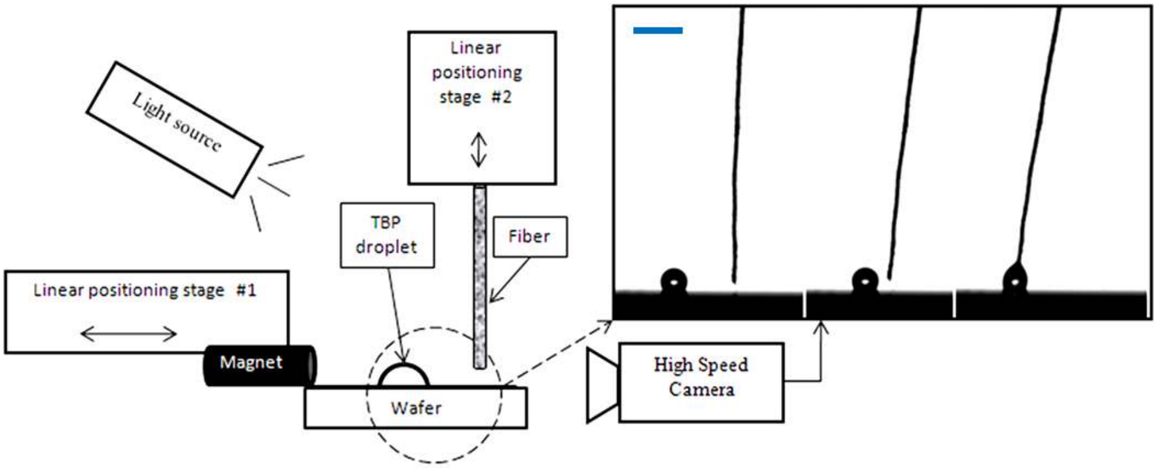

Figure 6.7. Absorption of a TBP droplet by the artificial proboscis made of PVDF/PEO fibers with embedded superparamagnetic nanoparticles. The proboscis was manipulated with a magnetic field. The scale bar is 2 mm

6.7 Methods and Materials

6.7.1 Probe Manufacturing

Two grams of PVDF (Goodfellow Corporation) and 0.2 g PEO (M_w=1,000 kDa, Sigma–Aldrich) were dissolved in 10 g dimethylacetamide (DMAc, Spectrum) at 55 °C.

All chemicals were used as received without further purification. The prepared polymer solution was placed in a 10 mL syringe. A flexible syringe heater (Watlow, EHG SL10) was attached to the syringe to maintain the temperature at 55 °C. The syringe with its heater was placed on the syringe pump (New Era Pump System, NE-300). A rotating mandrel with four aluminum bars separated from each other by 20 cm was used as a fiber collector. A high-voltage power supply (Glassman High Voltage, Inc.) was connected to the syringe through a stainless-steel needle (Gauge 20, EXEL) and a 35-cm wide gap separated the needle end from the nearest face of the mandrel. The flow rate was controlled at 0.2 mL/hr. A positive voltage varying between 8–10 kV was applied to the needle until a fiber jet and Taylor cone were produced. A second high-voltage power supply was attached to the collector and a negative charge of 1 kV was applied. The device for fiber collection consists of two ¾-inch diameter circular wire brushes, mounted co-axially and each attached to a miniature DC motor. The same device was used to form yarns by spinning the brushes in the opposite directions. The number of revolutions and the rate of twisting was controlled with totalizer counters (Crouzet 2108) and optical reflection sensors (OPTEC Technology OPB704WZ) operating in the infrared range of light, thus avoiding any interference with other devices. Solid non-porous fibers were obtained at 25-35% RH while porous fibers were obtained at 65% RH even without PEO removal Fibers were prepared at ambient temperature, 23-25 °C.

6.7.2 Fiber Porosity[7]

The quantitative estimate can be done using a simple spring model. If the AFM tip with attached fiber has mass M and the elastic constant of the cantilever spring is k, the tip oscillations in the vertical plane are described by the spring model as $M\, d^2y/dt^2 + ky = 0$, where y is the vertical coordinate of the tip center of mass, and t is the time, and oscillations are considered about the tip equilibrium position $y = 0$. Assuming sinusoidal oscillations of the form $y = a \sin (ft)$, where a is the tip amplitude, and f is its frequency, and substituting this form into the spring equation, we find the natural frequency as $f = \sqrt{k/M}$. When the cantilever is subjected to the forced oscillations, the oscillations become amplified as the frequency approaches the natural frequency f; hence this frequency is called the resonance frequency [43]. Therefore, one can measure the resonance frequency f of the cantilever with the dry fiber, and the resonance frequency $f_{\mathrm{m}} = \sqrt{k/(M + M_{\mathrm{liquid}})}$ of the cantilever with the fiber containing the liquid of mass M_{liquid}. The mass of liquid can be found as $M_{\mathrm{liquid}} = (k/f_{\mathrm{m}}^2)[1-(f_{\mathrm{m}}/f)^2]$. If the resonance frequency of the cantilever without fiber is f_{AFM}, the fiber mass M_{fiber} can be found as $M_{\mathrm{fiber}} = (k/f^2)[1-(f/f_{\mathrm{AFM}})^2]$. Therefore, from these experiments, the mass of fiber and absorbed liquid can be obtained.

---

[7] The fiber porosity was analyzed by Dr. Ruslan Burtovyy.

6.7.3 Analysis of Pore Size Distribution

The pore size distribution was analyzed by using ImageJ software (NIH). The images from Figure 6.2B were cropped into several 2 μm × 1 m pieces and the number of pores in each picture was calculated. ImageJ also provides the pore area. To estimate the pore diameter, we assumed that all pores were made of circular cylinders with diameter d. Figure 6.5 shows that most pores had the diameters in the range of 60 ~ 80 nm. The average diameter was calculated from $D_p = \Sigma f_i * d_i$, where f is the probability to find the diameter d_i, and subscript i corresponds to the site at which the pore diameter was measured within the prescribed range from 50 to 190 nm.

6.7.4 Probe Characterization by Fourier Transform Infrared Spectroscopy (FT-IR)

FT-IR spectra of the electrospun nanofiber yarns were measured on Nicolet 550 Magna-IR spectrometer in the 400-1000 cm^{-1} range. Figure 6.8A shows three different IR spectra of PVDF pellets, PVDF/PEO films obtained by dip coating of glass slides, and electrospun PVDF/PEO fibers. The $C_2H_2F_2$ molecular unit cells in the PVDF chain have net dipole moments, pointing the electronegative fluorine the hydrogen, and can crystallize forming different phases with different dipole orientations [44]. It is known that β-phase mostly consists of CF_2-CH_2 dipoles oriented in the same directions, i.e., this phase is ferroelectric. In another phase, called α-phase, the dipoles are counter directed or form clusters with zero net moment, i.e., this phase is not ferroelectric. β- and α-phases can be distinguished by their spectral characteristics: absorption bands of the β-phase are situated at 509 and 840 cm^{-1} and absorption bands of the α-phase appear at 530, 614, 762, and 795 cm^{-1} [45-47]. To estimate the fractional content of β- and α-phases in pellets, films and fibers, the fraction of β-phase in each sample was calculated using the Beer–Lambert law [45-47] in the form:

$$A_\alpha = \log\frac{I_\alpha^{\ 0}}{I_\alpha} = K_\alpha C X_\alpha L,\ A_\beta = \log\frac{I_\beta^{\ 0}}{I_\beta} = K_\beta C X_\beta L, \qquad (6.13)$$

where A_α and A_β are absorbencies of each phase, I^0 and I are the incident and transmitted radiation intensities, respectively, L is the sample thickness, C is the total monomer concentration, $K_{\alpha,\beta}$ are the absorption coefficients, and $X_{\alpha,\beta}$ are the mass fractions of the α- and β-crystals (sometimes called the degrees of crystallinity of each phase).

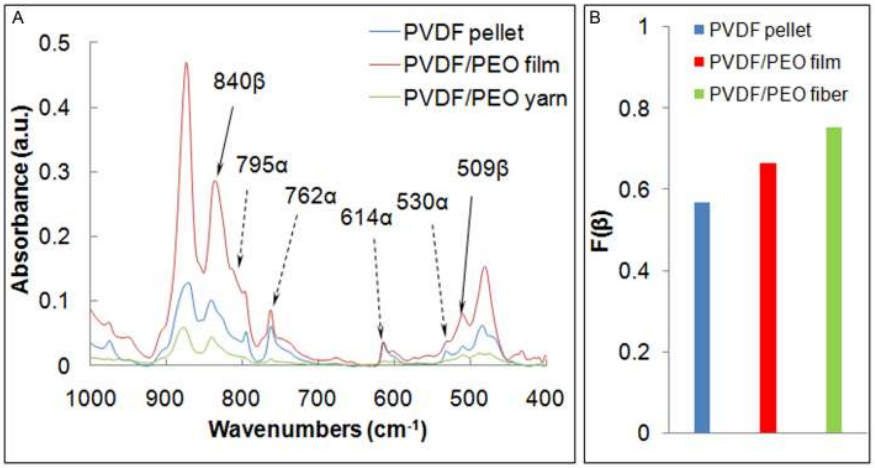

Figure 6.8. (A) FTIR spectra of PVDF pellet, dip-coated PVDF–PEO film, and electrospun PVDF–PEO fiber. (B) β/α ratios for PVDF pellets, PVDF–PEO film and electrospun PVDF–PEO fibers, suggesting that the electrospun fibers contain greater amount of ferroelectric crystals.

In the literature, the absorption coefficients of PVDF measured at 762 and 840 cm^{-1} wavenumbers: $K_\alpha = 6.1 \times 10^4$ cm^2 /mole and $K_\beta = 7.7 \times 10^4$ cm^2 /mole [45-47]. Using these parameters, the relative fraction of the 840 cm^{-1} β- phase with respect to 762 cm^{-1} α- phases is given as:

$$F(\beta) = \frac{X_\beta}{X_\alpha + X_\beta} = \frac{A_\beta}{(K_\beta / K_\alpha)A_\alpha + A_\beta} = \frac{A_\beta}{1.26A_\alpha + A_\beta}\,. \tag{6.14}$$

The results are presented in Figure 6.8B. In the electrospun PVDF/PEO fibers, the fraction of β-crystals appears greater than that found in the PVDF pellets. Quantitatively, about 30% increase of the β-crystals was observed in electrospun fibers. It has been shown that the α or γ phases can be converted in the ferroelectric β-phase by application of a strong electric field [45] or by fiber or film drawing [48]. In electrospinning, both these mechanisms may play important role in the enrichment of electrospun fibers with the β-phase.

This analysis, however, does not provide any information about the direction of the polarization vector in the fibers. One can assume that the polarization vectors in crystallites are randomly oriented, because the external field changed frequently owing to the mandrel rotation as well as because of flipping of the field directions between each pair of charged arms.

6.7.5 Swelling Properties: PVDF/PEO Films

To confirm that the liquid is wicked into the pores but not absorbed by the PVDF fiber itself, a series of experiments was conducted on films of the same composition. A dip coater (MTI Corporation, HWTL-01) with a temperature chamber for controlling the internal temperature was used to make uniform films. The temperature was set at 55 ^{0}C. Glass slides (Corning Inc., 2947-3x1) were used as the coating substrates. The pulling speed was maintained at 78 mm/min. The films were dried in the chamber for 10 minutes, then overnight at room temperature in a fume hood, and finally under vacuum at room temperature for 4 hours.

The thickness of prepared PVDF/PEO films was measured before soaking them in the liquids (HEX and TBP). A digital timer was used to record the soaking time. Every 5 minutes, the film was taken off from the liquids and an extra liquid was removed from the film surface. Then an image was taken by a camera. After that, the film was put back in the liquid and time was counted continuously. The film thickness at different time moments was measured by the ImageJ (NIH) software. The brightness and contrast were adjusted to make the film thickness measurable. The thickness δ of the PVDF/PEO film was defined as $\delta = (A_2 - A_1)/2$ (Figure 6.9), where A_1 is the thickness of a glass slide (1 mm) and A_2 is the total thickness of the PVDF/PEO film plus the glass slide. Ten points were measured along the film and the average and standard deviations of film thickness were presented in Figure 6.10. The swelling ratio is defined as $(\delta_t - \delta_0)/\delta_0$, where δ_t is the film thickness at time t and δ_0 is the initial film thickness. As shown in Figure 6.10, the swelling ratio is less than 5% after 20 minutes soaking. This time is on the same order as that of the time of wicking of HEX and TBP droplets. We confirmed that at time increments shorter than the time of droplet disappearance, which is typically approximate 20 min, swelling of PVDF/PEO films is not significant, less than 5%. Therefore, one can safely neglect the swelling effect and interpret the experiments based on physical flow phenomena.

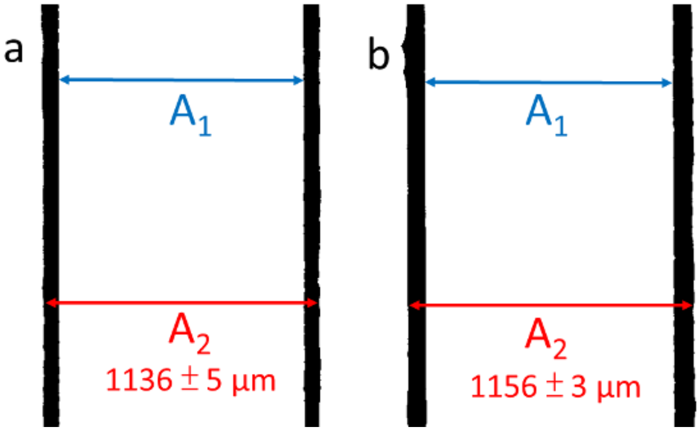

Figure 6.9. The blue line refers to the thickness of glass slide (1 mm) and the red line refers to the total thickness of PVDF/PEO film plus the glass slide. (a) without soaking in TBP and (B) after soaking 120 minutes in TBP.

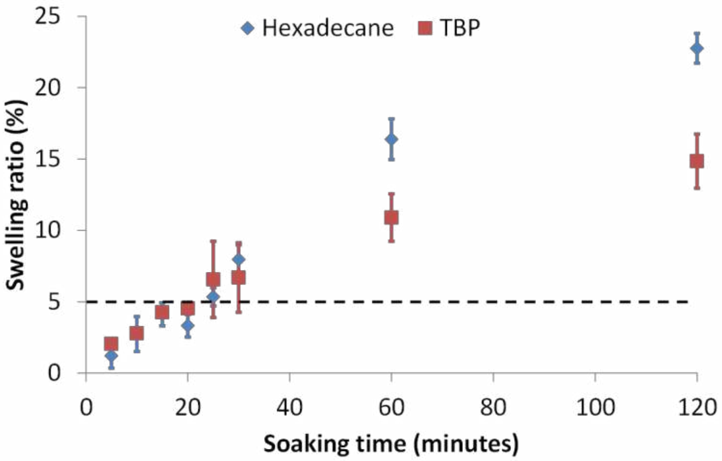

Figure 6.10. The swelling ratio versus different soaking time in HEX and TBP.

6.8 Conclusions

A technique to fabricate artificial proboscises was developed. PVDF/PEO fibers have been electrospun into ordered bands and subsequently twisted into yarns. By controlling the electrospinning time and revolution rate of the proposed twisting device, we formed biomimetic proboscis probes with repeatable transport properties. By varying the chemical composition of polymer blends and environmental conditions for electrospinning, we achieved porosities as high as 82% for single fibers. As predicted theoretically, and proven experimentally, the absorption rate of the probes can be significantly increased if one designs the probes to have double porosity composed of micro- and nanopores. Depending on the application, the probe can be made ferroelectric or magnetic. Further, owing to the ferroelectric and magnetic properties of the probes produced in this work, these probes can function as artificial proboscises and can be manipulated remotely. Commercially available microfluidic devices are typically monolithic stationary platforms with multiple channels to which the liquid is delivered either by a pipette or by a pump. One should mention that the produced materials swell in hours after a TBP or hexadecane droplet gets inside. Thus, these probes can be used as sensors as well. This work has the potential to embed multiple sensing devices in a single fiber and make the probing device in the form of an artificial octopus with many different microarms probing and analyzing the substrate in different places simultaneously. The fiber-based flexible platform here developed opens up many opportunities for probing and manipulating hazardous liquids, extracting biofluids from microorganisms or secretory glands, or operating on single cells.

6.9 References

1. Kornev, K.G., D. Monaenkova, C. Yore, C. Klipowics, E. Edmond, V. Sa, and T. Andrukh. *Buttefly proboscis as a biomicrofluidic system*. in *2008 AICHE Annular Meeting, November 16-21*. 2008. Philadelphia, PA AICHE.

2. Monaenkova, D., M.S. Lehnert, T. Andrukh, C.E. Beard, B. Rubin, A. Tokarev, W.K. Lee, P.H. Adler, and K.G. Kornev, *Butterfly proboscis: combining a drinking straw with a nanosponge facilitated diversification of feeding habits.* Journal of the Royal Society Interface, 2012. **9**(69): p. 720-726.

3. Reneker, D.H., A.L. Yarin, E. Zussman, and H. Xu, *Electrospinning of nanofibers from polymer solutions and melts*, in *Advances in Applied Mechanics, Vol 41*. 2007. p. 43-195.

4. Reneker, D.H. and A.L. Yarin, *Electrospinning jets and polymer nanofibers.* Polymer, 2008. **49**(10): p. 2387-2425.

5. Dzenis, Y., *Materials science - Structural nanocomposites.* Science, 2008. **319**(5862): p. 419-420.

6. Rutledge, G.C. and S.V. Fridrikh, *Formation of fibers by electrospinning.* Advanced Drug Delivery Reviews, 2007. **59**(14): p. 1384-1391.

7. Fang, J., H.T. Niu, T. Lin, and X.G. Wang, *Applications of electrospun nanofibers.* Chinese Science Bulletin, 2008. **53**(15): p. 2265-2286.

8. Janle, E.M. and J.E. Sojka, *Use of ultrafiltration probes in sheep to collect interstitial fluid for measurement of calcium and magnesium.* Contemporary Topics in Laboratory Animal Science, 2000. **39**(6): p. 47-50.

9. Huang, C.M., C.C. Wang, M. Kawai, S. Barnes, and C.A. Elmets, *In vivo protein sampling using capillary ultrafiltration semi-permeable hollow fiber and protein identification via mass spectrometry-based proteomics.* Journal of Chromatography A, 2006. **1109**(2): p. 144-151.

10. Reukov, V., A. Vertegel, O. Burtovyy, K.G. Kornev, and I. Luzinov, *Fabrication of nanocoated fibers for self-diagnosis of bacterial vaginosis* Materials Science and Engineeering C, 2008.

11. Monaenkova, D. and K.G. Kornev, *Elastocapillarity: Stress transfer through fibrous probes in wicking experiments.* Journal of Colloid and Interface Science, 2010. **348**(1): p. 240-249.

12. Dabirian, F. and S.A.H. Ravandi, *Novel Method for Nanofibre Yarn Production Using Two Differently Charged Nozzles.* Fibres & Textiles in Eastern Europe, 2009. **17**(3): p. 45-47.

13. Afifi, A.M., S. Nakano, H. Yamane, and Y. Kimura, *Electrospinning of Continuous Aligning Yarns with a 'Funnel' Target.* Macromolecular Materials and Engineering, 2010. **295**(7): p. 660-665.

14. Zhang, K., X.F. Wang, Y. Yang, L.L. Wang, M.F. Zhu, B.S. Hsiao, and B. Chu, *Aligned and Molecularly Oriented Semihollow Ultrafine Polymer Fiber Yarns by a Facile Method.* Journal of Polymer Science Part B-Polymer Physics, 2010. **48**(10): p. 1118-1125.

15. Bazbouz, M.B. and G.K. Stylios, *Novel mechanism for spinning continuous twisted composite nanofiber yarns.* European Polymer Journal, 2008. **44**(1): p. 1-12.

16. Mondal, A., R. Borah, A. Mukherjee, S. Basu, M. Jassal, and A.K. Agrawal, *Electrospun self-assembled nanofiber yarns.* Journal of Applied Polymer Science, 2008. **110**(1): p. 603-607.

17. Zhou, F.L. and R.H. Gong, *Manufacturing technologies of polymeric nanofibres and nanofibre yarns.* Polymer International, 2008. **57**(6): p. 837-845.

18. Moon, S. and R.J. Farris, *How is it possible to produce highly oriented yarns of electrospun fibers?* Polymer Engineering and Science, 2007. **47**(10): p. 1530-1535.

19. Smit, E., U. Buttner, and R.D. Sanderson, *Continuous yarns from electrospun fibers.* Polymer, 2005. **46**(8): p. 2419-2423.

20. Teo, W.E. and S. Ramakrishna, *A review on electrospinning design and nanofibre assemblies.* Nanotechnology, 2006. **17**(14): p. R89-R106.

21. Adu-Wusu, K. and N.M. Hassan, *Evaluating the effects of tributyl phosphate (TBP) and normal paraffin hydrocarbon (NPH) in simulated low-activity waste solution on ion exchange.* Separation Science and Technology, 2005. **40**(1-3): p. 463-482.

22. Carrera, J.A., E. Munoz, E. Bringas, M.F. San Roman, and I. Ortiz, *Influence of operation variables on the recovery of zinc from spent pickling effluents using the emulsion pertraction technology.* Desalination, 2009. **245**(1-3): p. 675-679.

23. Kumbasar, R.A., *Separation and concentration of cobalt from aqueous thiocyanate solutions containing cobalt-nickel by emulsion liquid membranes using TBP as extractant.* Journal of Membrane Science, 2009. **338**(1-2): p. 182-188.

24. Kumbasar, R.A., *Selective extraction of chromium (VI) from multicomponent acidic solutions by emulsion liquid membranes using tributhylphosphate as carrier.* Journal of Hazardous Materials, 2010. **178**(1-3): p. 875-882.

25. Messikh, N., M.H. Samar, and L. Messikh, *Neural network analysis of liquid-liquid extraction of phenol from wastewater using TBP solvent.* Desalination, 2007. **208**(1-3): p. 42-48.

26. Ortiz, I., E. Bringas, M.F. San Roman, and A.M. Urtiaga, *Selective separation of zinc and iron from spent pickling solutions by membrane-based solvent extraction: Process viability.* Separation Science and Technology, 2004. **39**(10): p. 2441-2455.

27. Zhao, L.F., D.J. Fei, Y.G. Dang, X.L. Zhou, and J.L. Xiao, *Studies on the extraction of chromium(III) by emulsion liquid membrane.* Journal of Hazardous Materials, 2010. **178**(1-3): p. 130-135.

28. Carroll, B.J., *The Accurate Measurement of Contact Angle, Phase Contact Areas, Drop Volume, and La Place Excess Pressure in Drop-Fiber Systems.* Journal of Colloid and Interface Science, 1976. **57**(3): p. 488-95.

29. Chen, X.M., K.G. Kornev, Y.K. Kamath, and A.V. Neimark, *The wicking kinetics of liquid droplets into yarns.* Textile Research Journal, 2001. **71**(10): p. 862-869.

30. Lucas, R., *Ueber das Zeitgesetz des kapillaren Aufstiegs von Flussigkeiten.* Kolloid Zeitschrift, 1918. **23**: p. 15-22.

31. Washburn, E.W., *The dynamics of capillary flow.* Physical Review, 1921. **17**: p. 273-283.

32. Neimark, A.V., S. Ruetsch, K.G. Kornev, P.I. Ravikovitch, P. Poulin, S. Badaire, and M. Maugey, *Hierarchical Pore Structure and Wetting Properties of Single Wall Carbon Nanotube Fibers.* Nano Letters, 2003. **3**(3): p. 419-423.

33. Raravikar, N.R., L.S. Schadler, A. Vijayaraghavan, Y.P. Zhao, B.Q. Wei, and P.M. Ajayan, *Synthesis and characterization of thickness-aligned carbon nanotube-polymer composite films.* Chemistry of Materials, 2005. **17**(5): p. 974-983.

34. Callegari, G., I. Tyomkin, K.G. Kornev, A.V. Neimark, and Y.L. Hsieh, *Absorption and transport properties of ultra-fine cellulose webs.* Journal of Colloid and Interface Science, 2011. **353**(1): p. 290-293.

35. Kornev, K.G., X. Ren, and Y. Dzenis, *Controlling Liquid Release by Compressing Electrospun Nanowebs.* Journal of Engineered Fibers and Fabrics, 2009. **4**(3): p. 14-23.

36. Alimov, M.M. and K.G. Kornev, *Impregnation of liquids into a laminated porous material with a high permeability contrast.* Physics of Fluids, 2007. **19**(10): p. 102108

37. Rouquerol, F., J. Rouquerol, and K. Sing, *Adsorption by powders and porous solids*. 1999, New York: Academic Press. 467.

38. Scheidegger, A.E., *The physics of flow through porous media*. 3rd ed. 1974, Toronto: University of Toronto.

39. Eastham, L.E.S. and Y.E.E. Eassa, *The feeding mechanism of the butterfly Pieris brassicae L.* Philosophical Transactions of the Royal Society of London. Series B, Biological Sciences, 1955. **239**(659): p. 1-43.

40. Korneva, G., H.H. Ye, Y. Gogotsi, D. Halverson, G. Friedman, J.C. Bradley, and K.G. Kornev, *Carbon nanotubes loaded with magnetic particles.* Nano Letters, 2005. **5**(5): p. 879-884.

41. Kornev, K.G., D. Halverson, G. Korneva, Y. Gogotsi, and G. Fridman, *Magnetostatic interactions between carbon nanotubes filled with magnetic nanoparticles.* Applied Physics Letters, 2008. **92**: p. 233117.

42. Freedman, J.R., D. Mattia, G. Korneva, Y. Gogotsi, G. Friedman, and A.K. Fontecchio, *Magnetically assembled carbon nanotube tipped pipettes.* Applied Physics Letters, 2007. **90**(10).

43. Landau, L.D. and E.M. Lifshitz, *Theory of elasticity*. 2nd ed. 1970, New York: Pergamon.

44. Poulsen, M. and S. Ducharme, *Why Ferroelectric Polyvinylidene Fluoride is Special.* Ieee Transactions on Dielectrics and Electrical Insulation, 2010. **17**(4): p. 1028-1035.

45. Andrew, J.S. and D.R. Clarke, *Effect of electrospinning on the ferroelectric phase content of polyvinylidene difluoride fibers.* Langmuir, 2008. **24**(3): p. 670-672.

46. Gregorio, R. and M. Cestari, *Effect of Crystallization Temperature on the Crystalline Phase Content and Morphology of Poly(Vinylidene Fluoride).* Journal of Polymer Science Part B-Polymer Physics, 1994. **32**(5): p. 859-870.

47. Bormashenko, Y., R. Pogreb, O. Stanevsky, and E. Bormashenko, *Vibrational spectrum of PVDF and its interpretation.* Polymer Testing, 2004. **23**(7): p. 791-796.

48. Hsu, T.C. and P.H. Geil, *Deformation and transformation mechanisms of poly(vinylidene fluoride) (PVF2).* Journal of Materials Science, 1989. **24**(4): p. 1219-1232.

CHAPTER SEVEN

APPLICATIONS OF WICK-IN-A-TUBE SYSTEM

In Chapter 4 we have demonstrated that the yarn formation protocol developed in Chapter 2 allows one to produce yarn with reproducible transport properties. A wick-in-a-tube system was developed for the characterization of yarn permeability by taking advantage of phenomenon of spontaneous wicking. In this chapter, an experimental protocol to deal with the analysis of permeability of butterfly proboscis was developed.

7.1 Introduction

Butterflies and moths (Lepidoptera) use their slender proboscises to sip nectar, plant sap, animal tears, blood, and other fluids, which are generally complex in composition [1-3]. The proboscis simultaneously is a multifunctional material and a fluidic device composed of two flexible strands, the maxillary galeae, with C-shaped medial faces joined by cuticular projections, the legulae [4]. The materials organization of the proboscis is unique, enabling it to perform multiple tasks, such as fluid acquisition, environmental sensing, coiling and uncoiling, and self-cleaning [1-3, 5, 6].

The size of the dorsal legulae and the interlegular spacing significantly increase in the distal 5-20% of the proboscis [3, 4]. The distal region, which is called the drinking region, is hydrophilic, while the remaining ~ 80% of the proboscis has hydrophobic properties [7]. The drinking region plays a critical role in fluid acquisition, especially for feeding on porous materials such as rotten fruits and tree sap. It has been shown [4, 8] that submicron pores (interlegular spaces) in the proboscis provide strong capillary action favoring the uptake of fluid droplets and films [9] and facilitating fluid withdrawal from pores [4]. Lepidoptera feed on porous materials, such as rotten fruits, and it proboscis typically has a brushlike extension of chemosensilla, which aids fluid uptake [4, 10]. Extant members of ancient lepidopteran lineages also have brushy proboscises [11], suggesting that capillarity had an early selective advantage, perhaps in exploiting limited moisture and sugary exudates [12, 13]. Evolutionary diversification of siphonate Lepidoptera, including those with comparatively smooth proboscises capable of reaching pools of nectar in floral tubes, was associated with the radiation of flowering plants [9, 13].

The mechanism by which Lepidoptera acquire fluid from a pool has been debated [6, 14-16]. The drinking-straw model, based on the Hagen-Poiseuille equation [17], was proposed to explain a relation between the observed flow rate and the pressure drop required from the suction pump, with flow rate decreasing as proboscis length increases [6, 18, 19]. This model is useful for crude estimates of the effects of food-canal diameter and fluid viscosity on the feeding efficiency and energetic requirements [6, 18], but faces problems when attempting to interpret experimental observations on the uptake of thick fluids [16]. The Hagen-Poiseuille model [6] of the fluid flow through a cylindrical tube cannot be directly applied to the butterfly proboscis because it is not a circular cylinder.

The proboscis tip historically has been viewed as sealed [15, 20], notwithstanding the analogy to a drinking straw. As revealed by X-ray tomography [4], however, the food canal converges apically to a microscopic slit-like opening. A second structural problem for the drinking-straw model is the distal taper of the food canal [4, 21]. A tapered food canal increases viscous friction [22] significantly restricting fluid uptake. Optimizing uptake from liquid films and droplets versus pools is, therefore, contradictory; a small lumen enhances capillarity [4], whereas a large lumen enhances flow [6, 17].

To test the hypothesis that the proboscis can function as a Hagen-Poiseuille straw, the permeability and flow in the drinking region were tested. The experimental data did not fit the drinking-straw model, and a new model was proposed. The pressure differential that would be required, based on our data, is greater than one atmosphere; thus, a vacuum pump could not function. To account for this paradox, we suggest that the butterfly can adjust the apical opening and the taper of the food canal by slightly splaying open the galeae at the distal tip to reduce the pressure differential when feeding on thick fluids. A second behavioral feature also could adjust the fluid-pressure differential by changing the size of the interlegular pores and apical opening. The ability to slide the galeae past one another in antiparallel movements [23] is well-documented for moths that pierce animal and plant tissues [24]; it is also common in nectar and other pool-feeding Lepidoptera and can serve to adjust the pressure differential.

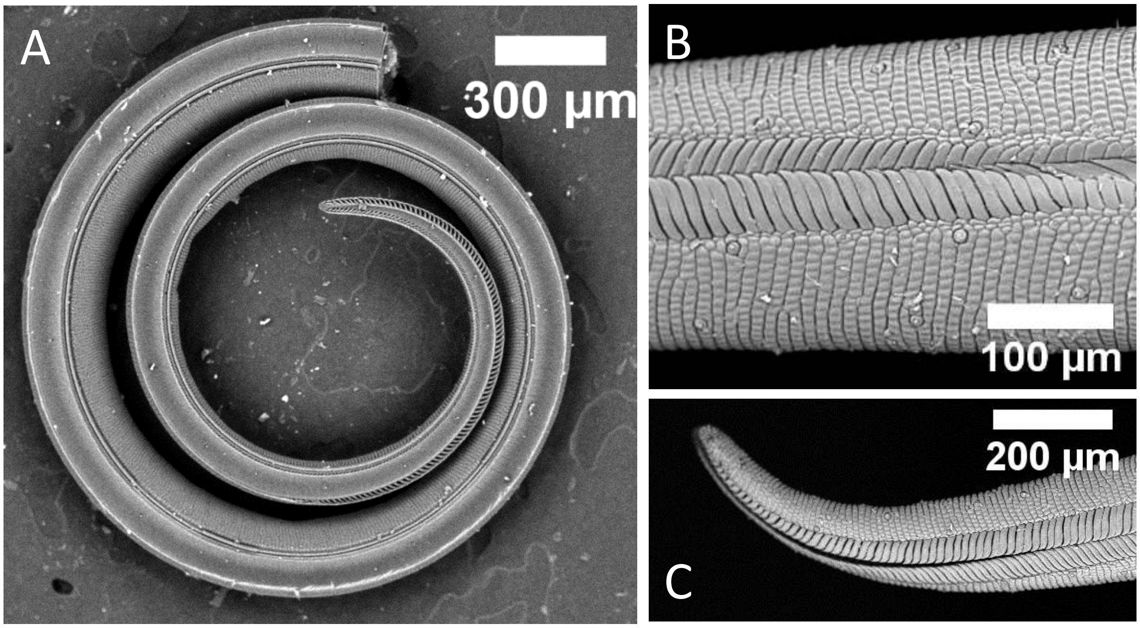

Figure 7.1. Scanning electron micrographs. (A) Single galea of the monarch proboscis. (B) Dorsal legulae. (C) Proboscis tip showing slit between opposing galeae.

7.2 Materials and Methods

7.2.1 Proboscis Permeability

The ability of a conduit or porous material to transport fluid at the fixed pressure gradient $\Delta P/l$ is characterized by the materials parameter called "permeability" [25, 26], denoted here as k. Permeability enters the problem via Darcy's law [25, 26], which states that the flow discharge Q through each proboscis cross-sectional area A and thickness l is written as $Q = (kA/\eta)(\Delta P/l)$, where η is the liquid viscosity and ΔP is the pressure differential. In particular, if the proboscis is modeled as a cylindrical tube of radius R, the permeability k is derived from the Hagen–Poiseuille law as $k = R^2/8$ [17]. For a more complex geometry, the material parameter k can be obtained by directly measuring the total flow rate Q and pressure gradient and by knowing the proboscis cross-sectional area and viscosity of the liquid.

Permeability is a convenient metric for characterizing the transport properties of the butterfly proboscis and interlegular pore structure [4]. Permeability of the interlegular pores in the nondrinking region can be determined by placing a droplet of water on the dorsal legulae and evaluating its uptake kinetics [4]. The slits between adjacent legulae 5 mm and 10 mm distal to the head of a monarch butterfly were estimated as 96 ± 27 nm and 162 ± 18 nm, respectively[4]. This droplet method, however, is not reliable for determining permeability of the drinking region; the spreading and intake rates of a droplet in the drinking region are comparable.

A new method was developed to evaluate proboscis permeability in the drinking region. A proboscis was inserted into a glass capillary tube and immersed in water (Figure 7.2). Due to capillary forces, water spontaneously invades the proboscis pores and food canal, moving further into the capillary tube. The flow rate was measured directly with a Cahn DCA-322 Dynamic Contact Angle Analyzer by monitoring an incremental change of the weight of hanging capillary at each moment of time. The pressure differential at the point where the proboscis meets the bore was not possible to measure. However, one can determine the contact angle θ, and the meniscus radius (Figure 7.2). This way, the driving capillary pressure, $P_c = 2\cos\theta/r$ can be obtained independently. Once the driving capillary pressure is known, the problem of determination of the proboscis permeability is reduced to the problem of liquid flow through a composite conduit consisting of two tubes connected in a sequence.

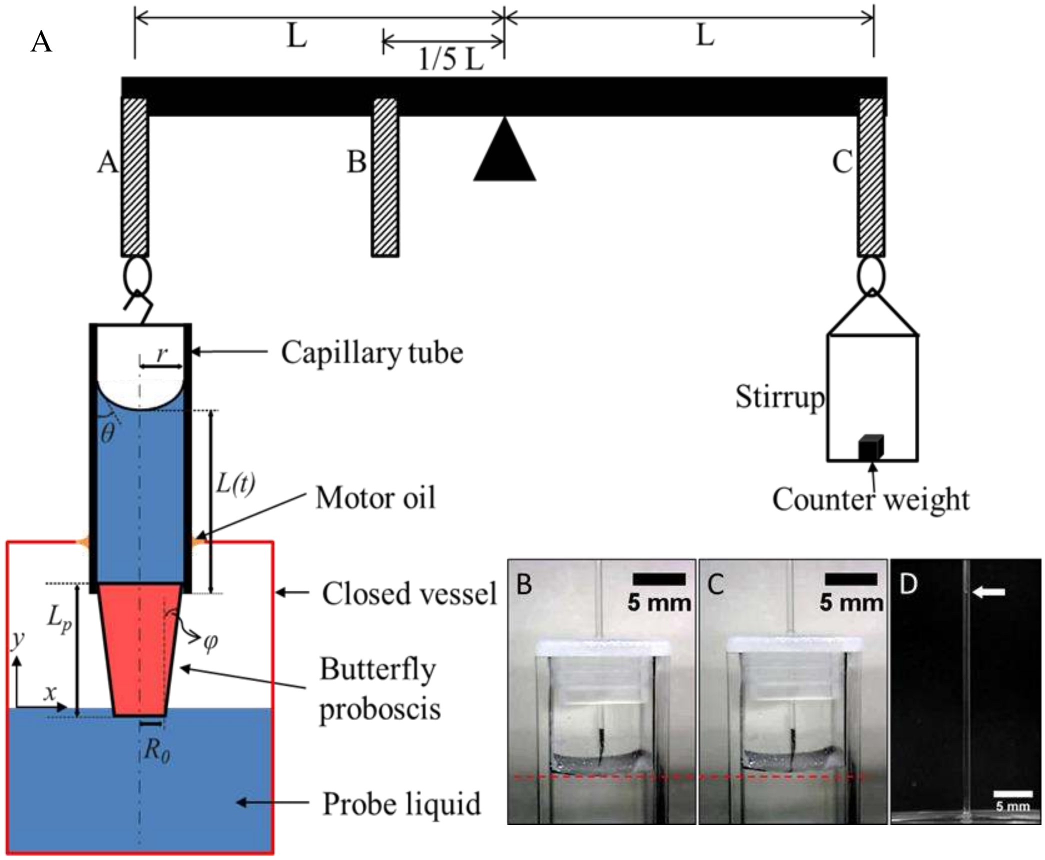

Figure 7.2. (A) Schematic of experiment showing the operation principle of the Cahn DSA-322. A capillary tube with the proboscis is connected to the balance arm through a hook. An oil droplet closes the rectangular vessel, preventing water evaporation and allowing the tube to move freely through the hole. Water moves from the reservoir to the tube by capillary action. The weight of the wicking water column is measured by the balance arm as the meniscus moves up the bore of the capillary tube. (B) Closed vessel after 1 hour of saturation with water vapor. The proboscis is suspended above the water. (C) The same vessel at the moment when the proboscis tip touches the water. (D) Example of measurement of Jurin length (Z_c), shown by the white arrow.

When such a conduit has a fixed length and the pressure differential is applied to the ends of this conduit, the problem appears similar to the Cohn-Rashevsky problem of design of some parts of the cardiovascular system [27-29]. In the case of moving meniscus, the length of the liquid column changes with time and one needs to change the Cohn-Rashevsky model. The corresponding mathematical analysis is presented in the

Appendix. A more realistic model of tapered food canal was used and analyzed the straight cylinder model as the limiting case. In each tube of the complex conduit the flow was assumed to follow the Hagen–Poiseuille law and the conservation of mass and the pressure continuity were used as the boundary conditions at the point where the proboscis meets the capillary. As follows from this model, the permeability of the capillary tube could be separated from the permeability of the proboscis.

7.2.2 Preparation of Proboscises[8]

Proboscises of monarch butterflies (*Danaus plexippus* L.) for scanning electron microscopy were straightened with crisscrossed pins on foam, dehydrated through an ethanol series (80-100%), dried in hexamethyldisilazane, mounted with double-sided conductive adhesive tape on aluminum stubs, and sputter coated with platinum for 3 minutes. Imaging was done with a Hitachi TM3000 (Hitachi High Technologies America Inc., Alpharetta, GA, USA) at 15KV, composite image mode, and full vacuum.

Coiled proboscises of 6 monarch butterflies were soaked in deionized water for 12 hours to soften and uncoil. They were straightened several millimeters at a time and fixed in position with pins every 2 hours. Straightened proboscises were examined with an optical microscope to confirm that the galeae did not separate apically and to measure the diameter.

---

[8] The SEM micrographs were taken by Dr. Charles Beard.

7.3 Experiment Design

To analyze the permeability of the proboscis, the Cahn DCA-322 was used. This instrument allows one to detect incremental changes in the sample weight with 1 μg accuracy (Figure 7.2A). A 5 mm long piece of each straightened proboscis was cut proximal to its tip, and the cut end was inserted into a capillary tube. The inserted portion was approximate 3 mm long; the remaining (distal) 2 mm, which included the drinking region, protruded from the capillary tube. The tube with the proboscis was placed in a rectangular vessel (Polystyrene, 12.5 mm × 12.5 mm × 45 mm, BRAND), and capped (Cuvette cap square, Fisher Scientific). A 3 mm diameter hole in the cap was punched, allowing the capillary tube to hang freely in the container, but permitting the Cahn balance arm to connect to it (Figure 7.2A). The tip of the proboscis was suspended above the water, without touching it (Figure 7.2B). A drop of motor oil (Castrol, SAE 5W-30) was used to seal the space between the hole edges and external wall of the tube, preventing evaporation and serving as a lubricant to enable the tube to move during wicking experiments. The tip of the proboscis was brought in contact with the water by raising the stage with the water vessel at 20 μm per second (Figure 7.2C). From the control experiments, we found that the trapped air bubble separating the top of the sealed vessel from the water surface required about 1 hour to reach full saturation with the water vapor (99 %RH) when the water filled the vessel up to $Z = 30$ mm height.

A schematic of the mechanical principle of force measurement by the Cahn DCA-322 is shown in Figure 7.2A. Two loops were used for force measurements (loop A and loop B). Loop A was more sensitive and could measure a force up to 1.5 mN; loop B was less sensitive and could measure a force up to 7.5 mN. A reference weight on loop C was used to counterbalance the sample weight, allowing maximum sensitivity. The ratio of the applied masses on the three loops (A: B: C) was 1: 5: 1, meaning that 100 mg sample on loop A or loop C created the same torque as 500 mg sample on loop B.

7.3.1 Data Acquisition

A special function of the Cahn DCA-322—the Zero Depth of Immersion (ZDOI)—can set the starting moment for weight measurements. The moment when the proboscis tip first touched the water is chosen as the ZDOI point; this was experimentally found that this point can be distinguished by setting a minimum force threshold of F_{min} = 5 μN. With this choice of the ZDOI point, if the measured force was less than 5 μN, the stage kept moving up. The balance was first zeroed; when the stage moved up, the force became negative due to friction and wiggling of the capillary tube [30]. However, this background noise was less than 5 μN, and was not recorded (Figure 7.3). When the proboscis touched the water, the force rapidly increased, reflecting the action of the wetting force, which was significantly larger than the ZDOI threshold (red arrow) [30]. The friction on the capillary tube exerted by the lubricating layer of oil was always much smaller than the threshold value F_{min}.

When the tip of the proboscis touched the water and the measured force became greater than F_{min}, the stage continued to rise up to 0.1 mm at 20 μm/s, confirming that the proboscis tip was immersed in water. A negative slope in Figure 7.3 was associated with the immersion process and was caused by buoyancy and increased viscous friction forces at the meniscus when the proboscis became immersed [30]. The stage then was stopped. One minute was waited to stabilize the entire setup, and began acquiring the force change for the next 60 minutes (red line, Figure 7.3). After the stage was stopped, a meniscus inside the capillary tube was observed, and all incremental changes of force detected by the analyzer were attributed to the incremental change of weight of the water column invading the tube due to capillary action.

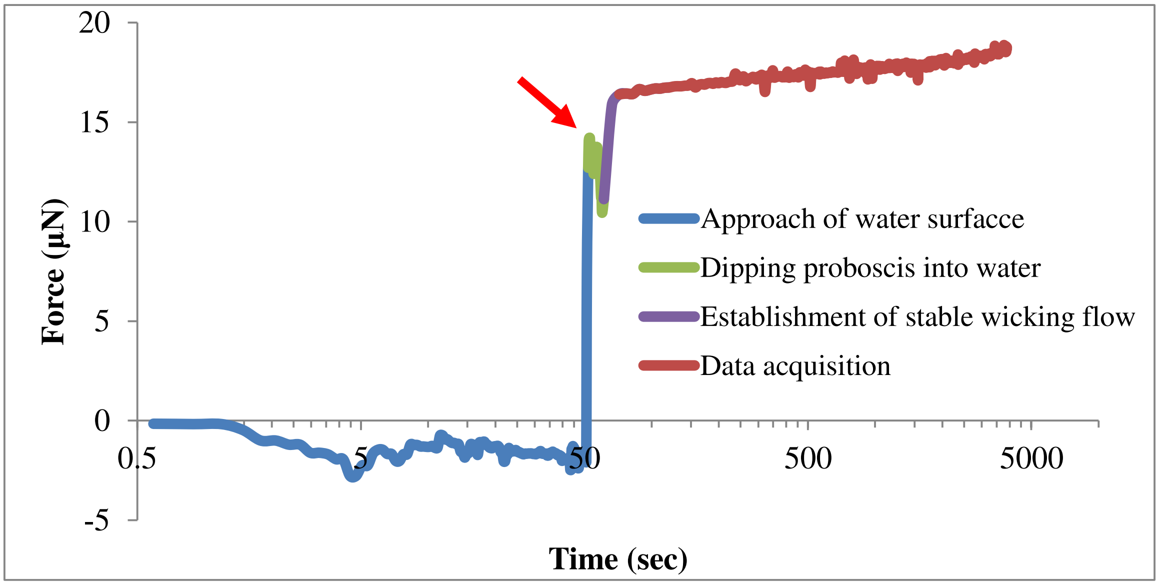

Figure 7.3. Typical experimental curve showing force changes at different steps of proboscis movement. A steep jump of the blue line allowed the ZDOI point to be defined. The proboscis was immersed further into the water for 0.1 mm (green line). After 1 minute (purple line), the change of water weight for 60 minutes was collected (red line).

7.3.2 Interpretation of Wicking Experiments

The center of Cartesian coordinates was taken at the water surface, with the *y*-axis pointing upward. The flow potential, Φ, was introduced as the sum of the pressure in water $P(y)$ at position y and hydrostatic pressure due to weight of the liquid column:

$$\Phi = P(y) + \rho g y, \qquad (7.1)$$

where ρ is water density and g is acceleration due to gravity. In this definition, the pressure at the water surface is zero and the potential is zero. Thus, Darcy's law is written through the flow potential as $Q = - k_pA/\eta(\partial\Phi/\partial y)$, where k_p is the permeability of the proboscis, η is the liquid viscosity, and $\partial\Phi/\partial y$ is the potential gradient along the proboscis. With this definition of permeability, the material parameter k_p could be obtained by measuring the total flow rate (Q) and the potential gradient and by knowing the proboscis cross-sectional area and viscosity of liquid used in our experiments. In the experiment, the flow rate was measured directly using the Cahn DSA-322, but the potential gradient was not defined. Therefore, data interpretation required additional information regarding the fluid flow. Below, a model was set up allowing us to extract the permeability from the experiment data.

7.3.2.1 Liquid discharge through the drinking region of the food canal (Q_H)

The cross-sectional area in the drinking region of the food canal, A, changes from the tip to the proximal end of the drinking region. The shape of the food canal in the drinking region was assumed conical (Figure 7.4). The radius of the food canal at the submerged tip is denoted by R_0, and the radius of the food canal at the proximal end of the drinking region is denoted by R_p. Introducing the cone angle φ, the radius of food canal at position y from the tip is expressed as $R(y) = R_0 + y\ tan\varphi$. Using the Hagen–Poiseuille law and assuming that the taper angle is small, the permeability of the drinking region of the food canal is approximated as $k_H = (R_0 + ytan\varphi)^2/8$. Accordingly, the water discharge through a cross-sectional area $A(y)$ is expressed as:

$$Q_H = -\frac{k_H A(y)}{\eta}\frac{\partial \Phi_H}{\partial y} = -\frac{\pi(R_0 + y\tan\varphi)^4}{8\eta}\frac{\partial \Phi_H}{\partial y}, \tag{7.2}$$

where subscript "H" refers to the drinking region. The flow discharge through any proboscis cross-section y is the same at any time moment t, $Q_H = Q_H(t)$. Substituting this relation in Eq. (7.2) and integrating it:

$$\int_0^H \frac{8\eta Q_H(t)dy}{\pi\left(R_0 + y\tan\varphi\right)^4} = -\Phi_H(H) = -(P_H + \rho g H), \tag{7.3}$$

where H is the drinking region length and P_H is the pressure at the end of the food canal. Solving Eq. (7.3) for Q_H, the liquid discharge through the drinking region of the food canal is expressed as:

$$Q_H(t) = -(P_H + \rho g H)\Bigg/\int_0^H \frac{8\eta dy}{\pi\left(R_0 + y\tan\varphi\right)^4}. \tag{7.4}$$

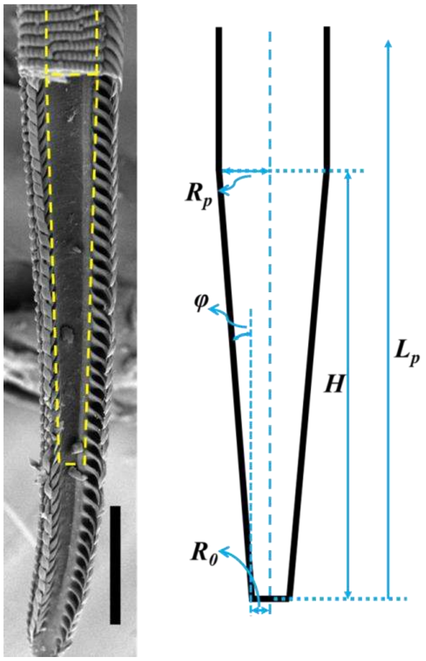

Figure 7.4 A schematic of a food canal model. Symbols: proboscis length L_p, drinking region length H, food canal radius R_p, drinking region radius at truncated tip R_0, and taper angle φ. The scale bar is 100 μm.

7.3.2.2 Liquid discharge through the nondrinking region of the food canal (Q_p)

Above the drinking region, y > H, the cone angle φ of the food canal becomes small, Figure 7.4, and the food canal in the non-drinking region is modeled by a straight cylindrical tube with radius, R_p. Therefore, the flow of the liquid column can be described by the Hagen–Poiseuille law [31] written in Darcy's form as $Q_p = -\left(k_p A / \eta\right)\left(\partial \Phi_p / \partial y\right)$ with $k_p = R_p^2/8$. Subscript "p" refers to the nondrinking region of the food canal. Using the mass conservation equation, we obtain $\partial Q_p/\partial y = \partial^2 \Phi_p/\partial y^2 = 0$. Integrating this equation, the linear distribution of the potential along the liquid column, $\Phi_p = cy + d$, can be inferred, where c and d are time-dependent functions that can be found from the boundary conditions. The boundary conditions state that the pressure at the end of the drinking region of the food canal y = H must be equal to the pressure in the water column at the same position y = H. Therefore, $P_H + \rho g H = cH + d$. At the inserted end of the food canal $y = L_p$, the pressure is written as $P_p + \rho g L_p = cL_p + d$. From these two boundary conditions, it follows that $c = (P_p - P_H + \rho g[L_p - H]) / [L_p - H]$ and $d = P_p + \rho g L_p - (P_p - P_H + \rho g(L_p - H))H / (L_p - L)$. With the obtained constants, the liquid discharge through the rest of the food canal is expressed as:

$$Q_p = -\left(k_p A / \eta\right) a = -\frac{\pi R_p^4}{8\eta} (P_p - P_H + \rho g[L_p - H]) / [L_p - H]. \qquad (7.5)$$

The pressure at the end of the drinking region of the food canal, P_H, can be related using the conservation of mass, $Q_H = Q_p$:

$$-(P_H+\rho gH)\Big/\int_0^H \frac{8\eta dy}{\pi\left(R_0+y\tan\varphi\right)^4}=-\frac{\pi R_p^4}{8\eta}(P_p-P_H+\rho g[L_p-H])/[L_p-H]. \tag{7.6}$$

Taking the integral and using the definition $R_p = R_0 + H \tan\varphi$, the pressure P_H is expressed as:

$$P_H=\frac{BP_p+\rho gB\left(L_p-H\right)-\rho gAH}{A+B}, \tag{7.7}$$

where we introduce the constants:

$A = 3\tan\varphi R_0^3 R_p^3/(R_p^3 - R_0^3)$ and $B = R_p^4/(L_p-H)$. (7.8)

These constants contain the structural parameters of the proboscis. Plugging Eq. (7.7) into Eq. (7.4), the liquid discharge through the nondrinking region of the food canal is expressed as:

$$Q_p=-\frac{\pi AB}{8\eta\left(A+B\right)}(P_p+\rho gL_p). \tag{7.9}$$

7.3.2.3 Meniscus motion through the capillary tube and related water discharge (*Q_c*)

Liquid discharge through the capillary tube is the same as that given by Eq. (7.4). Conservation of mass requires the following equality $Q_p = Q_c$, where the flow rate through the capillary is given by the Hagen–Poiseuille law with the pressure at one end $y = L_p$ being P_p and at the other end, i.e. at the meniscus position $y = L_p + L(t)$, being P_c:

$$-\frac{\pi AB}{8\eta\left(A+B\right)}(P_p+\rho gL_p)=-\frac{\pi r^4}{8\eta}(P_p+P_c+\rho g[L_p-L])\big/[L_p-L]. \tag{7.10}$$

Solving this equation for P_p one finds:

$$P_p = \frac{1}{(\frac{AB}{A+B} - \frac{r^4}{L_p - L})}\left[\frac{r^4 P_c}{L_p - L} + \frac{\rho g r^4}{L_p - L}(L_p - L) - \frac{\rho g A B L_p}{A+B}\right]. \tag{7.11}$$

Plugging Eq. (7.11) into Eq. (7.4) and expressing its left side through the meniscus velocity $Q_c = \pi r^2 dL/dt$, the basic equation describing the kinetics of meniscus propagation through the complex conduit consisting of the proboscis and capillary tube is expressed as:

$$\frac{dL}{dt} = \frac{r^2}{8\eta}\frac{\left(P_c - \rho g L\right)}{L - L_p + \frac{r^4\left(A+B\right)}{AB}}. \tag{7.12}$$

7.3.2.4 Engineering Parameters of the Butterfly Proboscis

The kinetics of meniscus propagation depends on the structural parameters of the butterfly proboscis indirectly, but through certain dimensionless complexes. To visualize this, the meniscus position is normalized by the Jurin length, Z_c, and the time in Eq. (7.12) by the following characteristic time:

$$t_0 = \frac{8\eta Z_c}{\rho g r^2} = \frac{8\eta P_c}{\rho^2 g^2 r^2}. \tag{7.13}$$

This time is approximately equal to the time required for a liquid meniscus to reach the Jurin length.

With this normalization, $L^* = L/Z_c$, $t^* = t/t_0$, Eq. (7.12) is rewritten as:

$$\frac{dL^*}{dt^*} = \frac{1 - L^*}{L^* + \beta}, \tag{7.14}$$

where

$$\beta = \frac{r^4\left(A+B\right)}{ABZ_c} - \frac{L_p}{Z_c}\,. \tag{7.15}$$

If the proboscis length is much smaller than the Jurin length (L_p << Z_c), the effect of gravity, the second term on the right side of Eq. (7.15), can be neglected, and Eq. (7.15) is simplified as:

$$\beta = \frac{r^4\left(A+B\right)}{ABZ_c}\,. \tag{7.16}$$

Eq. (7.14) is the familiar Lucas-Washburn equation describing capillary rise in tubes [32, 33], which has the solution:

$$-L^* - (1+\beta)\ln(1-L^*) = t^*\,. \tag{7.17}$$

Thus, using the introduced normalization, we can interpret the experiment data in an easier way by measuring the Jurin length Z_c, calculating the characteristic time t_0, and then fitting the experimental curve $L^*(t^*)$, by adjusting parameter β. After determination of this parameter, the length of the drinking region is calculated as:

$AB\beta Z_c - r^4\left(A+B\right) = 0$ or

$$H = \frac{3R_0^3R_p^4Z_c\beta - 3R_0^3R_p^4L_p}{R_pr^4\left(R_p^2 + R_pR_0 + R_o^2\right) - 3R_0^3r^4}\,. \tag{7.18}$$

7.3.3 Measurements of Surface Tension (σ)

The surface tension of deionized water was measured using the Wilhelmy method with a Cahn DCA-322 [31]. A platinum wire with a 250 μm diameter was used as the standard probe [30]. The wire was cleaned with ethanol and heated to red-hot with an oxidizing flame. The Wilhelmy equation $F = \sigma P cos\theta$ was used, where F is the wetting force, σ is the surface tension of the probe liquid, P is the perimeter of the probe, and θ is the contact angle. The contact angle is assumed $\theta = 0°$ or $cos\theta = 1$ because of the high surface energy of the platinum. Deionized water was measured three times, yielding an average surface tension of $\sigma = 71.4 \pm 0.5$ mN/m.

7.3.4 Determining Jurin length (Z_c) of a Capillary Tube

The contact angle of the internal meniscus was measured indirectly by analyzing the Jurin length (Z_c). The Jurin length is defined as the maximum possible height of the liquid column coexisting with the liquid reservoir [34] and it is equal to $Z_c = P_c/\rho g$ $=2\cos\theta/(\rho g r)$. The Jurin length therefore depends on the liquid density ρ, surface tension σ, contact angle θ, and radius of the capillary tube r. Deionized water (η: 1 mPa·s, ρ: 1000 kg/m^3), as the probe liquid, and a glass capillary tube with a 250-μm radius (r) were used to determine the Jurin length. Three experiments were performed, and the average Jurin length was calculated as $Z_c = 0.029 \pm 0.001$ m.

7.4 Results

Figure 7.5 shows the normalized experimental L^*-t^* curve for a butterfly proboscis. The blue hollow dots are the experimental data, and the solid black line is the fitting curve. Six different proboscises of monarch butterflies were used, and examined each proboscis at least three times (Figure 7.6). The results of the measurements of Jurin height and other physical parameters of the model are given in Table 7.1. Using these data, we analyzed the results of the wicking experiments and obtained the proboscis characteristics shown in Table 7.1. It should be noted that the dimensionless parameter β can be considered as one of the resistance of the complex conduit which significantly depends on the geometrical structure of butterfly proboscis. As a result, the parameters β are in wide range in Table 7.1 because of the different sizes between butterfly proboscis samples.

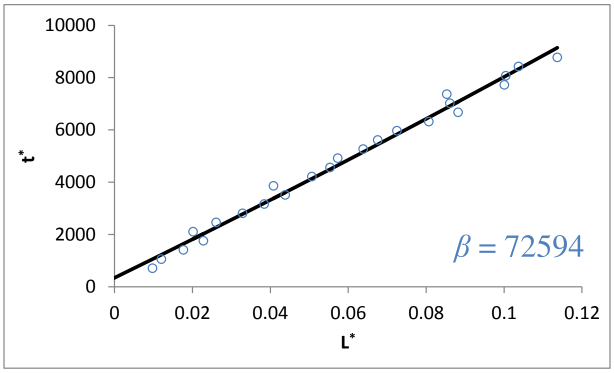

Figure 7.5. The experimental curve of dimensionless meniscus position (L^*) versus dimensionless time (t^*) for a butterfly proboscis acquired by the DCA-322 analyzer. The blue hollow dots are the experimental data, and the solid black line is the fitting curve.

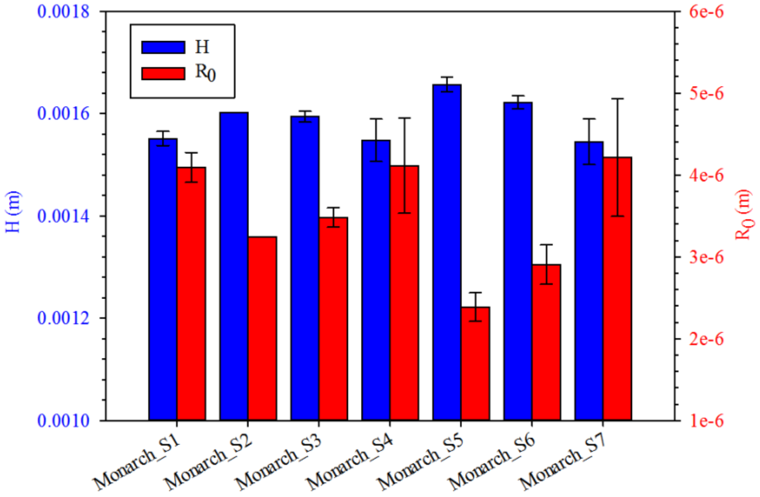

Figure 7.6. Average radii (± standard deviation) of the food canal at the tip of the drinking region R_0 and average length of the drinking region H of proboscises from 6 monarch butterflies.

Table 7.1. Radius of the proboscis opening at the tip and the length of the tapered part of the food canal of monarch butterfly proboscises.

Butterfly	**β ($\times 10^4$)**	**R_0 (μm)**	**H (mm)**	**Note**
Monarch_s1	1.5 ± 0.2	4.1 ± 0.2	1.55 ± 0.01	1. Zc = 29 mm.
* **Monarch_s2**	8.0	3.2	1.60	2. φ ~ 0.95°.
Monarch_s3	6.5 ± 0.7	3.5 ± 0.1	1.59 ± 0.01	3. t_0 ~ 0.38 s.
Monarch_s4	4.2 ± 1.8	4.1 ± 0.6	1.55 ± 0.04	4. L_p = 4.9 mm.
Monarch_s5	20.4 ± 4.7	2.4 ± 0.2	1.66 ± 0.01	5. R_p = 30 μm.
Monarch_s6	9.9 ± 6.4	2.9 ± 0.2	1.62 ± 0.01	*Only one measurement
Monarch_s7	4.2 ± 2.4	4.2 ± 0.7	1.54 ± 0.04	

7.4.1 Suction Pump Pressure

From the results, the pressure in the butterfly's suction pump was calculated, using the parameters in Table 7.2 and viscosity of sucrose solutions measured by magnetic rotational spectroscopy from Tokarev et al. [35]. Density was taken from Asadi [36]. The results of calculations based on Eq. (7.7) and (7.11) are shown in Figure 7.7, where the following notations were used: P_H = pressure at the end of the drinking region, P_p = pressure in the cibarial pump, P_t = pressure in the cibarial pump in the tube model of the proboscis when the tube radius R_p did not change along the proboscis.

Table 7.2. Parameters of the monarch proboscis and properties of model nectars [35, 36].

Sucruose Conc.	**η (mPa·s)**	**ρ (kg/m^3)**	**H (mm)**	**L_p (mm)**	**R_0 (μm)**	**R_p (μm)**	**tanφ**
10%	1.3 ± 0.2	1040	1.5	14	5	30	0.0167
20%	1.7 ± 0.2	1083	1.5	14	5	30	0.0167
30%	3.8 ± 0.4	1129	1.5	14	5	30	0.0167
40%	6.9 ± 0.7	1179	1.5	14	5	30	0.0167

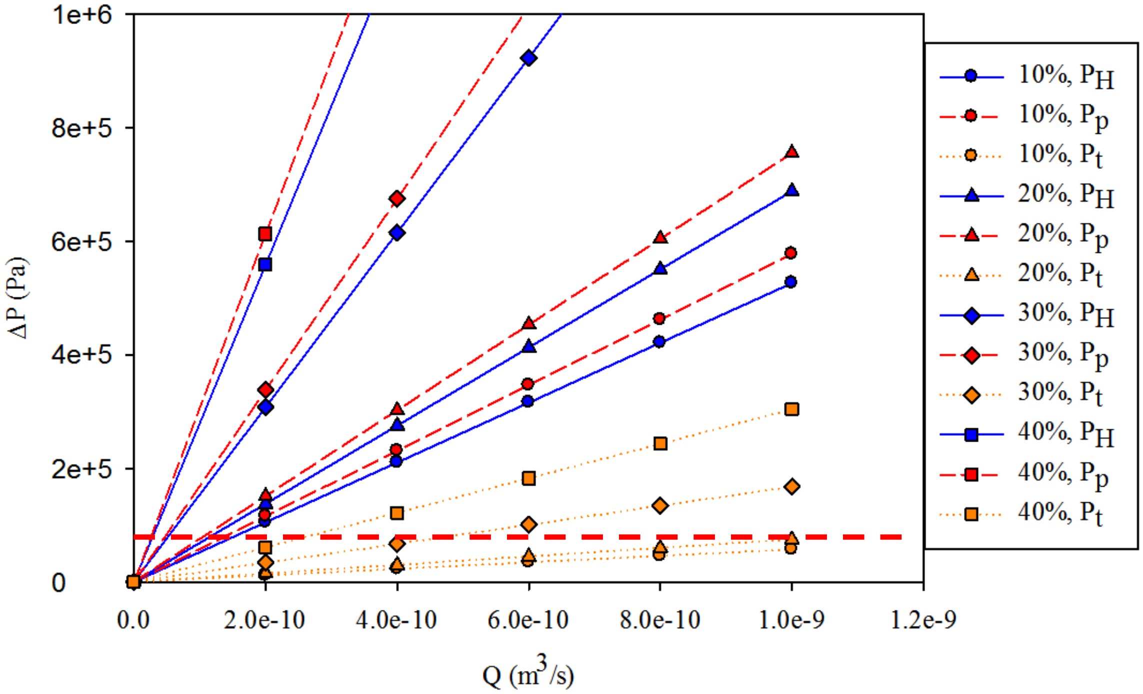

Figure 7.7. The pressure produced by the butterfly's cibarial pump, using parameters from Table 7.2. P_H = pressure at the end of the drinking region, P_p = pressure in the cibarial pump, P_t = pressure in the cibarial pump in the tube model of the proboscis when the tube radius R_p did not change along the proboscis.

7.5 Discussions

7.5.1 Drinking Straw Catastrophe

In experiments of monarchs feeding from a pool of liquid, the flow rate varies from 2×10^{-10} to 5×10^{-10} m^3/s. This flow rate assumes that development of the pressure differential in the suction pump is greater than 1 atmosphere, which is not possible. This pressure is required primarily to support flow through the drinking region where the radius of the food canal changes significantly. This structural feature of the proboscis is inherent in many Lepidoptera, suggesting that the taper is an important attribute of the proboscis. On the other hand, neglecting the taper, the required pressure can be reduced significantly below atmospheric pressure in most cases. The situation, therefore, is paradoxical: If structural features of the proboscis is taken into account, the required pressure skyrockets, while a simplistic drinking-straw model that ignores the structural features allows the pressure catastrophe to be avoided. Accordingly, the strategy of fluid acquisition by butterflies is more complex, and that the butterfly strategy allows high pressure differentials to be avoided.

7.6 References

1. Wigglesworth, V.B., *The life of insects*. 3rd edition ed. 1972, New York: Weidenfeld and Nicolson. 359.
2. Snodgrass, R.E., *The caterpillar and the butterfly.* Smithson Misc. Coll., 1961. **143**(6): p. 1-51.
3. Krenn, H.W., *Feeding Mechanisms of Adult Lepidoptera: Structure, Function, and Evolution of the Mouthparts.* Annual Review of Entomology, 2010. **55**: p. 307-327.
4. Monaenkova, D., M.S. Lehnert, T. Andrukh, C.E. Beard, B. Rubin, A. Tokarev, W.K. Lee, P.H. Adler, and K.G. Kornev, *Butterfly proboscis: combining a drinking straw with a nanosponge facilitated diversification of feeding habits.* Journal of the Royal Society Interface, 2012. **9**(69): p. 720-726.
5. Eastham, L.E.S. and Y.E.E. Eassa, *The feeding mechanism of the butterfly Pieris brassicae L.* Philosophical Transactions of the Royal Society of London. Series B, Biological Sciences, 1955. **239**(659): p. 1-43.
6. Kingsolver, J.G. and T.L. Daniel, *Mechanics of food handling by fluid-feeding insects*, in *Regulatory mechanisms in insect feeding*, R.F. Chapman and G. de Boer, Editors. 1995, Springer: New York. p. 32-74.
7. Lehnert, M.S., D. Monaenkova, T. Andrukh, C.E. Beard, P.H. Adler, and K.G. Kornev, *Hydrophobic–hydrophilic dichotomy of the butterfly proboscis.* Journal of the Royal Society Interface, 2013. **10**(85).
8. Tsai, C.C., P. Mikes, T. Andrukh, E. White, D. Monaenkova, O. Burtovyy, R. Burtovyy, B. Rubin, D. Lukas, I. Luzinov, J.R. Owens, and K.G. Kornev, *Nanoporous artificial proboscis for probing minute amount of liquids.* Nanoscale, 2011. **3**(11): p. 4685-4695.

9. Barth, F.G., *Insects and Flowers: The Biology of a Partnership*. 2nd ed. 1991, Princeton, NJ: Princeton University Press

10. Knopp, M.C.N. and H.W. Krenn, *Efficiency of fruit juice feeding in Morpho peleides (Nymphalidae, Lepidoptera).* Journal of Insect Behavior, 2003. **16**(1): p. 67-77.

11. Krenn, H.W. and N.P. Kristensen, *Early evolution of the proboscis of Lepidoptera: external morphology of the galea in basal glossatan moths, with remarks on the origin of the pilifers.* Zoologischer Anzeiger, 2000. **239**: p. 179-196.

12. Kristensen, N.P., *Studies on the morphology and systematics of primitive lepidoptera insecta.* Steenstrupia, 1984. **10**(5): p. 141-191.

13. Grimaldi, D.a.M.S.E., *Evolution of the Insects*. 2005: Cambridge University Press.

14. Borrell, B.J., *Mechanics of nectar feeding in the orchid bee Euglossa imperialis: pressure, viscosity and flow.* Journal of Experimental Biology, 2006. **209**(24): p. 4901-4907.

15. Borrell, B.J. and H.W. Krenn, *Nectar Feeding in Long-Proboscid Insects*, in *Ecology and Biomechanics: A Mechanical Approach to the Ecology of Animals and Plants* A. Herrel, T. Speck, and N.P. Rowe, Editors. 2006, CRC: Boca Roton. p. 185-205.

16. Lehane, M.J., *The Biology of Blood-Sucking in Insects*. 2nd ed. 2005, New York: Cambridge University Press.

17. Vogel, S., *Comparative Biomechanics: Life's Physical World* 2003, Princeton, NJ: Princeton University Press 582.

18. Kingsolver, J.G., *Butterfly engineering.* Scientific American, 1985. **253** (2): p. 106-114.

19. Kingsolver, J.G. and T.L. Daniel, *Mechanics and energetics of nectar feeding in butterflies.* Journal of Theoretical Biology, 1979. **76**(2): p. 167-&.

20. Krenn, H.W., J.D. Plant, and N.U. Szucsich, *Mouthparts of flower-visiting insects.* Arthropod Structure & Development, 2005. **34**(1): p. 1-40.

21. Krenn, H.W. and N. Muhlberger, *Groundplan anatomy of the proboscis of butterflies (Papilionoidea, lepidoptera).* Zoologischer Anzeiger, 2002. **241**(4): p. 369-380.

22. Batchelor, G.K., *An introduction to fluid dynamics*. 2000, New York: Cambridge University Press.

23. Krenn, H.W., *Proboscis assembly in butterflies (Lepidoptera) - a once in a lifetime sequence of events.* European Journal of Entomology, 1997. **94**(4): p. 495-501.

24. Buttiker, W., H.W. Krenn, and J.F. Putterill, *The proboscis of eye-frequenting and piercing Lepidoptera (Insecta).* Zoomorphology, 1996. **116**(2): p. 77-83.

25. Dullien, F.A.L., *Porous Media. Fluid Transport and Pore Structure* 1991, New York: Academic Press.

26. Scheidegger, A.E., *The physics of flow through porous media*. 3rd ed. 1974, Toronto: University of Toronto.

27. Cohn, D.L., *Optimal systems: I. The vascular system. Cohn.* The Bulletin of Mathematical Biophysics, 1954. **16**(1): p. 59 - 74.

28. Cohn, D.L., *Optimal systems: II. The vascular system.* . The Bulletin of Mathematical Biophysics, 1955. **17**(3): p. 219 - 227.

29. Rashevsky, N., *Mathematical Biophysics*. 3rd Ed ed. Vol. Vol. II. 1960, New York: Dover Publications, Inc. 462.

30. Miller, B., L.S. Penn, and S. Hedvat, *Wetting force measurements on single fibers.* Colloids and Surfaces, 1983. **6**(1): p. 49-61.

31. Adamson, A.W. and A.P. Gast, *Physical chemistry of surfaces*. 1997, New York: Wiley.

32. Lucas, R., *Ueber das Zeitgesetz des kapillaren Aufstiegs von Flussigkeiten.* Kolloid Zeitschrift, 1918. **23**: p. 15-22.

33. Washburn, E., *The Dynamics of Capillary Flow.* Phys. Rev. Physical Review, 1921. **17**(3): p. 273-283.

34. Jurin, J., *An account of some experiments shown before the Royal Society; with an enquiry into the cause of the ascent and suspension of water in capillary tubes.* Philosophical Transactions of the Royal Society, 1917-1919. **30**(351-363): p. 739-747.

35. Tokarev, A., B. Kaufman, Y. Gu, T. Andrukh, P.H. Adler, and K.G. Kornev, *Probing viscosity of nanoliter droplets of butterfly saliva by magnetic rotational spectroscopy.* Applied Physics Letters, 2013. **102**(3).

36. Asadi, M., *Tables A.1* in *Beet-Sugar Handbook*. 2005, John Wiley & Sons, Inc. p. 779-801.

CHAPTER EIGHT

CONCLUSION

1. A technique was developed to fabricate electrospun fiber yarn using a modified collector and twisting device. Different polymers and polymer blends were electrospun and collected. Fibers were twisted using a twisting device consisting of two co-axially mounted brushes. This design allowed control of the yarn diameter and compactness. The yarns produced were very uniform. These yarns had reproducible breaking stress, elongation at break, and Young's modulus. The modified electrospinning setup is a promising tool to fabricate yarns with reproducible properties.

2. The wick-in-a-tube technique was developed to enable determination of the permeability of electrospun yarns by taking advantage of wicking phenomenon. Yarns from different polymers were electrospun and characterized. The wicking kinetics in the wick-in-a-tube composite conduit was studied and the permeability was extracted from the modified Lucas-Washburn equation. The permeability of electrospun yarns demonstrated a two orders of magnitude range, from 10^{-14} m^2 to 10^{-12} m^2, by alternation of the fiber diameter and packing density.

3. Wetting properties of CA/PMMA yarns and their constituent films were studied. The contact angles on flat films were measured by the sessile drop technique while the contact angles on electrospun yarns were characterized by the capillary rise method.

The contact angles extracted from wicking experiments were close to the contact angles on the flat CA and PMMA films. The surface of microfibers made from polymer blends was smooth in while the surface of films made of the same blends was rough. This led to distinct wetting properties of yarns and films.

4. The challenge of making probes with fast absorption rates was addressed theoretically showing that the probe should possess two levels of pore hierarchy: nanopores are needed to enhance the capillary action and micrometer pores are required to speed up fluid transport. This model was verified in experiments. The yarns made of nanoporous fibers had faster wicking rates than those made of solid fibers. The nanopores caused strong suction and the micropores provided fast flow. It was shown that the artificial proboscises can be remotely controlled with electric or magnetic fields. Using an artificial proboscis, one can approach a drop of hazardous liquid, absorb it and safely deliver it to an analytical device.

5. The permeability of Monarch butterfly proboscises was characterized using the developed wick-in-a-tube technique. The experimental results did not fit the drinking-straw model, and a new model was proposed. Based on the experimental data, it was demonstrated that to drink fluids butterflies have to apply a pressure differential greater than one atmosphere.

APPENDICES

A Preliminary Results of Applications of Electrospun Yarns for Diagnosis of Sickle Cell Disease

Sickle cell disease was discovered over one hundred years ago and it is associated with drastic changes in the stiffness of the red blood cells [1]. Red blood cells (RBCs) contain a special protein called hemoglobin (Hb) to carry oxygen. Patients with sickle cell disease have a gene mutate affecting the hemoglobin protein [2]. As a result, hemoglobin molecules do not form properly, causing RBCs to change their conformation into a characteristic shape similar to a sickle used to cut wheat. These cells become stiff [3]. Normal red blood cells with adequate oxygen are flexible so they can travel freely through the narrow blood vessels. The abnormal sickle shaped cells get stuck in the blood vessels and are unable to transport oxygen effectively causing patients to experience frequent pain and damage to the lungs, kidneys, and other organs [1, 3]. The patients with sickle cell disease often have low red blood cell counts (anemia), which is why this disease is commonly called sickle cell anemia. People with this disorder have their life span reduced by approximate 30 years.

Screening blood and hemoglobin requires a clinical laboratory equipped with specialized instruments, consumable materials, and highly-trained technicians, which is expensive and rarely affordable for patients in developing countries such as South Africa and Southeast Asia where the sickle cell disease is wide spread [1, 4]. The urgent need to develop a low-cost diagnostic test for sickle cell disease has become a priority for these countries. In this work, electrospun fiber yarns with controlled pore sizes were suggested to use for diagnostic of the sickle cell disease. The hypothesis is that the normal RBCs can pass through the interfiber pores readily without obstruction while the abnormal RBCs would block the interfiber space resulting in the significant decrease of the yarn permeability. The yarn-in-a-tube technique developed in Chapter 4 was used to examine two types of the RBCs suspended in buffer solutions: one sample was prepared in the presence of oxygen; this sample models healthy RBCs sample; the other one was prepared in the presence of nitrogen modeling sickle RBCs. The preliminary results showed that the yarn permeability decreased after filtration of the sickle RBCs. These results suggested that the electrospun fiber yarns with controlled permeability may be used in the applications to biomedical diagnostics and screening of the blood samples.

A.1 Experimental[9]

A.1.1 Characterization of Red Blood Cells Suspended Buffer Solution

Before running the permeability experiments, the density (ρ) and viscosity (η) of RBCs suspended buffer solutions were first characterized. Two types of RBCs were prepared: (1) the oxygen enriched cells, which model the healthy RBCs and is symbolized by Oxy; and (2) the oxygen limited cells, which were prepared in the presence of nitrogen. These cells model the sickle RBCs and are symbolized by Deoxy. Density was calculated by precisely measuring the weight of 500 μL of each RBCs suspended in the buffer solution. The results ranged from 1.037 to 1.042 g/cm^3, and ρ =

---

[9] The RBCs suspended buffer solutions were prepared by Dr. Alexey Aprelev in Drexel University. I am grateful for his help in the solution preparation, characterization of solution densities, and wicking experiments.

1.04 g/cm^3 was used for further calculations. Viscosity was determined by analyzing the kinetics of meniscus movement inside the vertically placed 500 μm diameter capillary (Figure A.1). This kinetics is described by Eq. (2.11) of Chapter 2:

$$\frac{dL}{dt} = -\frac{r^2}{8\eta}\frac{\Delta P}{L} = -\frac{r^2}{8\eta}\frac{P_c - P_g}{L}, \tag{A.1}$$

where L is the meniscus position, r is the capillary radius, η is the liquid viscosity, P_c is the capillary pressure (= $\rho g Z_c$), Z_c is the Jurin length, P_g is the hydrostatic pressure (= $\rho g L$), and t is time.

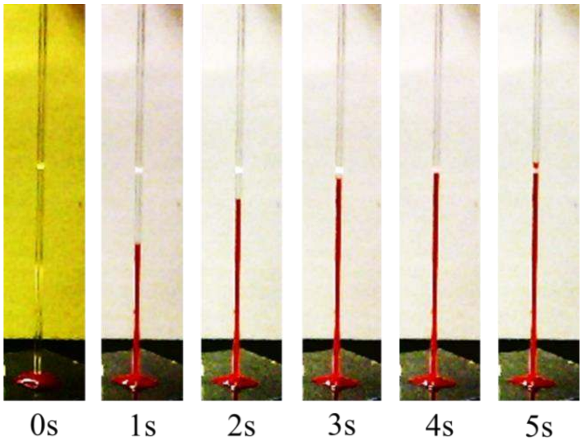

Figure A.1. An example of experimental frames showing the meniscus of Deoxy RBCs moving inside a 500 μm capillary.

Eq. (A.1) is the well-known Lucas-Washburn equation describing capillary rise in a tube [5, 6], which has the solution:

$$-L - Z_c \ln(1 - \frac{L}{Z_c}) = \frac{\rho g r^2}{8\eta} t. \tag{A.2}$$

The Jurin length (Z_c) was determined by measuring the equilibrium height of the liquid column in the same 500 μm diameter capillary. The Jurin length Z_c = 0.031 m appeared the same for both Oxy and Deoxy solutions. A USB portable microscope

(B003+ Multi-function, Shenzhen D&F Co.) with recording frequency of one frame per second (fps) was used to determine the position of liquid meniscus $L(t)$. Figure A.2 shows the curves of meniscus position (L) versus time (t) for Oxy and Deoxy solutions. The viscosities of Oxy and Deoxy solutions were obtained by using a Matlab code to fit the experimental data and the blue dashed lines corresponded to the theoretical model. As one obtains the fitting parameter $\rho g r^2/(8\eta)$, one can calculate the viscosity. The viscosity of Oxy solution was calculated as $\eta_o = 10.9$ cp and the viscosity of Deoxy was calculated as $\eta_d = 6.8$ cp.

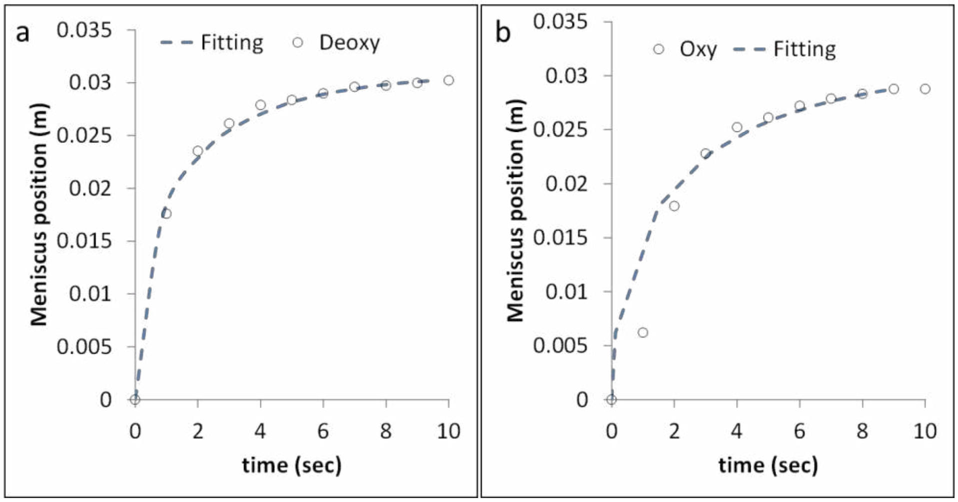

Figure A.2. Meniscus dynamics in 500 μm diameter capillary tube of (a) Oxy and (b) Deoxy solutions. The blue dashed lines represent the theoretical results.

A.1.2 Preparation of Yarns with Different Interfiber Space

Cellulose acetate (CA) and poly(methyl methacrylate) (PMMA) were dissolved in Dimethylacetamide (DMAc) with the CA/PMMA ratio = 1:1 (by weight) to prepare solutions of different polymer concentrations: 15wt%, 20wt%, and 25wt%. These solutions were individually electrospun to produce fibers. Fibers were collected and twisted into yarns by applying different turns per centimeter (tpcm). The permeability was determined using the techniques described in Chapter 4 and the pore sizes (interfiber distance, r_p) were summarized in Table A.1.

Table A.1. The characteristics of yarns used in experiments with blood cells.

Polymer Concentration (wt%)	**Yarn density (tpcm)**	**Pore size (μm)**	**Symbol**
15	13	~1	1u
20	15	~2	2u
20	12	~3	3u
25	15	~4	4u

A.2 Results: Permeability of Oxy and Deoxy Solutions

The experimental protocol used is similar to that described in Chapter 4. The CA/PMMA yarns were cut in L_y = 5 mm long and the yarn radius was measured as R_y = 250 μm. A USB portable microscope (B003+ Multi-function, Shenzhen D&F Co.) with recording frequency of one fps was used to determine the meniscus position $L(t)$. The camera was employed here because the experiments were run in oxygen and nitrogen flow which caused strong vibrations/noise and influenced the accuracy of data acquisition of the Cahn DCA-322 analyzer. The characteristic time t_0 for each solution was calculated using Eq. (4.11). The characteristic time of Oxy solution was t_0 = 4.24 seconds, and the characteristic time of Deoxy solution was t_0 = 2.65 seconds. The dimensionless variables, L^* and t^*, were calculated: L was divided by Z_c, and t was divided by t_0. Figure A.3a shows the typical curves of dimensionless meniscus position (L^*) versus dimensionless time (t^*) for both the Oxy and Deoxy solutions. Again, α parameters were obtained by using a Matlab code to fit the experimental data and the black dashed lines corresponded to the theoretical model (Figure A.3a). The corresponding permeabilities were calculated by Eq. (4.16) and summarized in Figure A.3b.

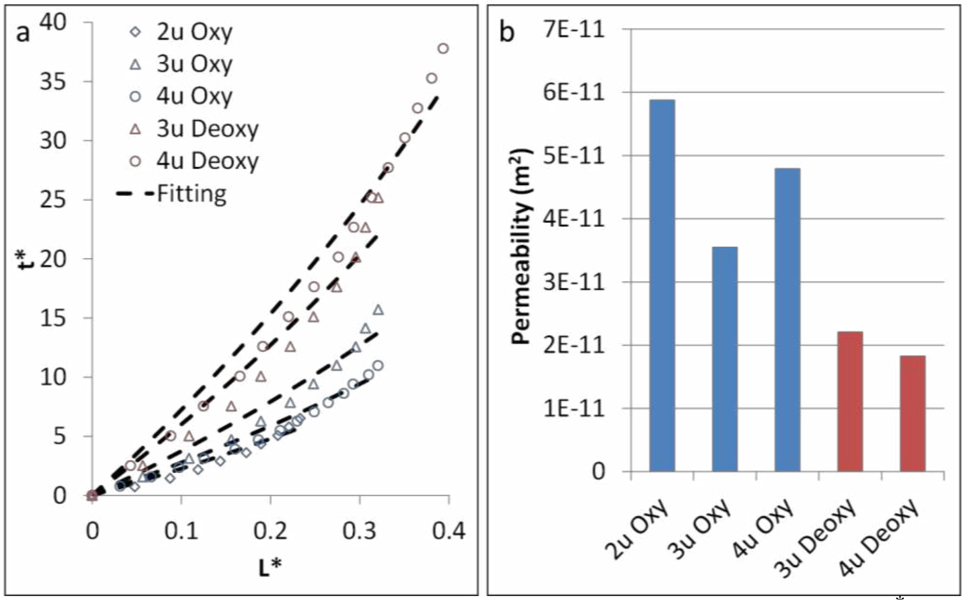

Figure A.3. (a) The typical curves of dimensionless meniscus position (L^*) versus dimensionless time (t^*) for Oxy and Deoxy solutions. The black solid lines represent the fitting curves. (b) A summary of permeability of Oxy and Deoxy solutions.

It is seen in Figure A.3b that the permeability of Oxy solutions is larger than that of Deoxy solutions. The permeability can be considered as an ability of a porous material to transport fluids through it, and it significantly depends on the geometrical structure of the medium. Since the pore sizes were controlled during the yarn formation, the decrease of permeability is caused by the cells blocking the pores. As we mentioned in the beginning, the normal RBCs are flexible and can pass through small pores. On the contrary, the sickle RBCs deform to sickle shape and become rigid. Therefore, the sick RBCs cannot pass through small pores and block the pores with clots resulting in the reduction of permeability.

A.3 Experimental Observation

A simple experiment was used to confirm the observations on the changes of permeability during filtration of RBCs. The concept is to verify that the clogging of pores will result in the decrease of permeability. A 10 wt% polyvinyl alcohol (PVA, MW: 146-180 kDa, Sigma Aldrich) solution was prepared. The PVA polymer was selected because it does not dissolve in hexadecane. One end of the CA/PMMA/PEO yarn (produced in Chapter 4) was immersed in the PVA solution to wick PVA inside the yarn, and the prepared samples were dried in the hood overnight. Then the permeabilities of CA/PMMA/PEO yarns and CA/PMMA/PEO with PVA yarns were determined using the wick-in-a-tube composite conduit.

Figure A.4a shows the typical curve of dimensionless meniscus position (L^*) versus dimensionless time (t^*) for CA/PMMA/PEO and CA/PMMA/PEO with PVA. As shown in Figure A.4a, the dimensionless meniscus position of CA/PMMA/PEO yarn with PVA inside is much smaller than that of CA/PMMA/PEO yarn at the same dimensionless time which suggests permeability was decreased dramatically. The permeability and porosity were examined on four prepared samples and summarized in Figure A.4b. Indeed, the results demonstrated that the permeability and porosity reduced significantly when the CA/PMMA/PEO yarns were clogged with PVA polymer. After examining the SEM micrographs of each material (Figure A.5), one confirms that the permeability of CA/PMMA/PEO with PVA yarns should be absolutely decreased since the PVA formed PVA bridges between fibers.

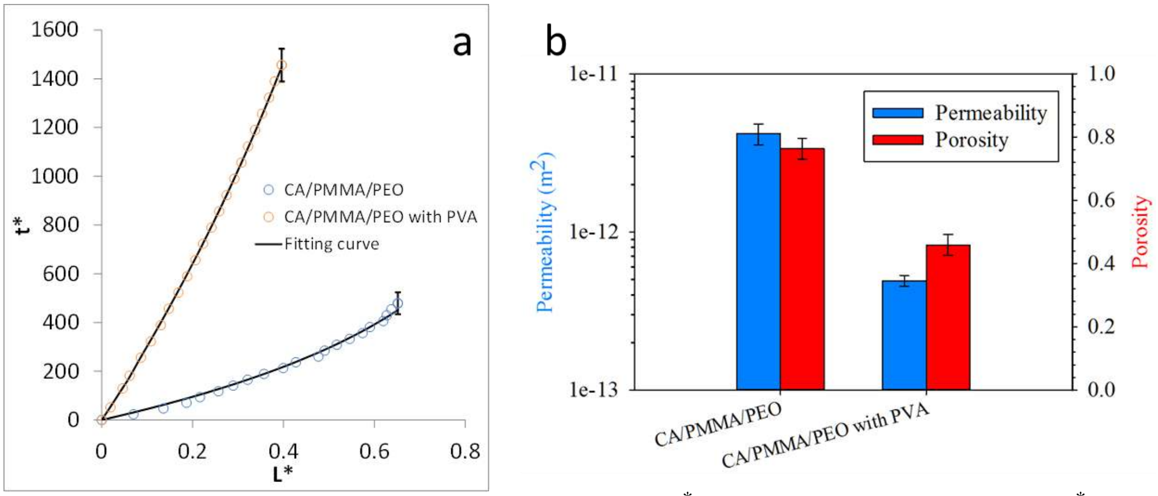

Figure A.4. (a) Dimensionless meniscus position (L^*) versus dimensionless time (t^*) for CA/PMMA/PEO and CA/PMMA/PEO with PVA. The black solid lines represent the fitting curves. (b) The permeability of CA/PMMA/PEO and CA/PMMA/PEO with PVA yarns. The *y* axis of permeability is presented in logarithmic scale. The error bars are the standard deviations.

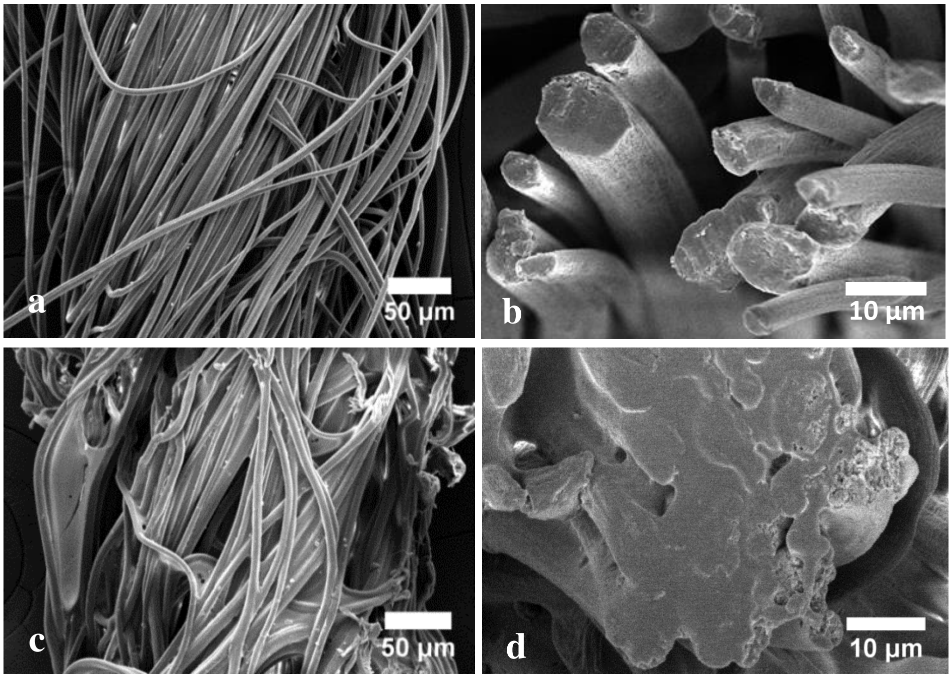

Figure A.5. The SEM micrographs of (a-b) CA/PMMA/PEO, (c-d) CA/PMMA/PEO with PVA. (a) and (c) represent the side view of yarn, and (b) and (d) represent the cross-sectional view of the yarn. The images confirm that the interfiber space was filled with PVA polymer, and the interfiber distance and porosity decrease.

A.4 Conclusions

The yarn-in-a-tube technique was proposed to diagnose the sickle cell disease. The yarn permeability was decreased after filtering of the sick RBCs solutions; the cells blocked some pores in the yarns. These results suggested that the electrospun fiber yarns with controlled permeability may be used for micro- or nanofluidic applications requiring separation and filtration of particles and emulsions.

A.5 Reference

1. Jones, P., *Sickle Cell Disease*. 2008: Chelsea House Publishers.
2. Orkin, S.H. and D.R. Higgs, *MEDICINE Sickle Cell Disease at 100 Years.* Science, 2010. **329**(5989): p. 291-292.
3. Schechter, A.N., *Hemoglobin research and the origins of molecular medicine.* Blood, 2008. **112**(10): p. 3927-3938.
4. Weatherall, D.J. and J.B. Clegg, *Inherited haemoglobin disorders: an increasing global health problem.* Bulletin of the World Health Organization, 2001. **79**(8): p. 704-712.
5. Lucas, R., *Ueber das Zeitgesetz des kapillaren Aufstiegs von Flussigkeiten.* Kolloid Zeitschrift, 1918. **23**: p. 15-22.
6. Washburn, E., *The Dynamics of Capillary Flow.* Phys. Rev. Physical Review, 1921. **17**(3): p. 273-283.